Title
Spectral Modeling of Solar and Atmospheric Radiation for Solar Power Integration

Author
Li, Mengying

Publication Date
2018

Peer reviewed|Thesis/dissertation

UNIVERSITY OF CALIFORNIA SAN DIEGO

Spectral Modeling of Solar and Atmospheric Radiation for Solar Power Integration

A Dissertation submitted in partial satisfaction of the
requirements for the degree
Doctor of Philosophy

in

Engineering Sciences (Mechanical Engineering)

by

Mengying Li

Committee in charge:

Professor Carlos F. M. Coimbra, Chair
Professor Renkun Chen
Professor Jan P. Kleissl
Professor Lynn M. Russell
Professor David G. Victor

2018

The Dissertation of Mengying Li is approved, and it is acceptable in quality and form for publication on microfilm and electronically:

Chair

University of California San Diego

2018

DEDICATION

This work is dedicated to my beloved family, for their loving support, encouragement and sacrifices.

EPIGRAPH

One, remember to look up at the stars and not down at your feet.

Two, never give up work. Work gives you meaning and purpose and life is empty without it.

Three, if you are lucky enough to find love, remember it is there and don't throw it away.

—Stephen Hawking

TABLE OF CONTENTS

LIST OF FIGURES

LIST OF TABLES

ACKNOWLEDGEMENTS

Foremost, I would like to express my sincerest gratitude to my mentor Dr. Carlos F. M. Coimbra for the continuous support during my time here at UC San Diego. He tops the list of people who have the most positive influence on me, because of his wisdom, passion about research, immense knowledge, enthusiasm, patience and caring heart. His guidance not only helped me thrive research-wise, but also life-wise for being such a wonderful role model. I respect him as a scientist, explorer and admirable person. Thank you so much for giving me the opportunity to join your group to conduct the research that I am passionate about, and offering me the teaching opportunities to find my passion. His countless invaluable guidance and support throughout the years gradually mold me into an independent researcher. I could not have imagined having a better mentor.

Besides Dr. Coimbra, my gratefulness also goes to the rest of my committee: Profs. Renkun Chen, Jan Kleissl, Lynn Russel and David Victor, for their constructive suggestions and valuable inspiration for my dissertation.

I would also like to acknowledge the help and support from previous and present research group members. First, I would like to thank Dr. Yinghao Chu, who provided valuable guidance during my first years here and being a good friend. I am also grateful for my coauthors Yuanjie Jiang and Zhouyi Liao for their help in conducting the research and writing papers. Dr. Hugo T. C. Pedro, who is always there to offer invaluable help. Thanks also to David P. Larson and Jeremy R. Orosco for being wonderful office mates to talk over research ideas, life events and encourage each other.

Last but not the least, I would like to thank my parents and parents-in-law for all the unconditional spiritual and financial support. From my father Baoping Li, I learn to be passionate about what I do and do the best I can. From my mother Jianjun Cui, I learn patience, unfailing love, gentleness and strength. My gratitude also belongs to my husband, Lequn Liu, for his loving support and for taking good care of the family. My last gratitude goes to my son Olymm (Muxin) Liu, for all the joy you bring to my life, and for motivating me to be a better self.

Chapter 2, in full, is a reprint of M. Li, Y. Jiang, and C. F. M. Coimbra (2017) “On the Determination of Atmospheric Longwave Irradiance under All-Sky Conditions.” *Solar Energy* (144), 40-48. The dissertation author is the first author of this publication.

Chapters 3 and 4, in full, are a combination of three publications: M. Li, Z. Liao, and C. F. M. Coimbra

(2018) “Spectral model for clear sky atmospheric longwave radiation” *Journal of Quantitative Spectroscopy and Radiative Transfer*, 209, 196-211; M. Li, Z. Liao and C. F. M. Coimbra (2018) “An Efficient Spectral Model for Evaluating Spectral and Spatial Distributions of Clear Sky Atmospheric Longwave Radiation,” accepted for the *16th International Heat Transfer Conference (IHTC-16)*; M. Li, and C. F. M. Coimbra (2018) “On the Effective Spectral Emissivity of the Sky,” submitted to *Proceedings of the National Academy of Sciences of the United States of America*. The dissertation author is the first author of these manuscripts.

Chapters 5 and 6, in full, are in preparation as a manuscript for publication with my co-author and Ph.D. adviser C. F. M Coimbra at UC San Diego. The dissertation author is also the first author of these papers.

VITA

2018	Ph. D. in Engineering Sciences (Mechanical Engineering), University of California San Diego, U. S.
2013	M. S. in Mechanical Engineering, University of Pennsylvania, Philadelphia, U. S.
2011	B. Eng. in Building Science, Tsinghua University, Beijing, China

PUBLICATIONS

Li, M., and Coimbra, C. F. M. (2018) " Local Thermal Effects Caused by Surface Albedo Replacement of Large Scale Photovoltaic and Concentrated Solar Farms". In preparation.

Li, M., Chu, Y., and Coimbra, C. F. M. (2018) "Sky-Imaging Network for Short-Term Spatial Solar Forecasts in the Los Angeles Basin". In preparation.

Zhou, L., Li, M. and Coimbra, C. F. M. (2018) "Approximation of Anisotropic Aerosol Scattering Effects on Longwave Irradiance". In preparation.

Li, M., and Coimbra, C. F. M. (2018) "On the Effective Spectral Emissivity of the Sky". Submitted to *Proceedings of the National Academy of Sciences of the United States of America*.

Li, M., Zhou, L. and Coimbra, C. F. M. (2018) "An Efficient Spectral Model for Evaluating Spectral and Spatial Distributions of Clear Sky Atmospheric Longwave Radiation". Accepted by *16th International Heat Transfer Conference (IHTC-16)*.

Li, M., Liao, Z., and Coimbra, C. F. M. (2018). "Spectral model for clear sky atmospheric longwave radiation". *Journal of Quantitative Spectroscopy and Radiative Transfer*, 209, 196-211.

Gross, K. C. and Li, M., "Method for Improved IoT Prognostics and Improved Prognostic Cyber Security for Enterprise Computing Systems". *Proceedings of the 2017 International Conference on Artificial Intelligence*.

Li, M., Jiang, Y., and Coimbra, C. F. M. (2017) "On the Determination of Atmospheric Longwave Irradiance under All-Sky Conditions." *Solar Energy* (144), 40-48.

Chu, Y., Li, M., and Coimbra, C. F. M. (2016) "Sun-tracking imaging system for intra-hour DNI forecasts." *Renewable Energy* (96), 792-799.

Li, M., Chu, Y., Pedro, H. T. C., and Coimbra, C. F. M. (2016) "Quantitative Evaluation of the Impact of Cloud Transmittance and Velocity Derivation on Short-term DNI Forecast." *Renewable Energy* (86), pp.1362-1371.

Li, M. and Lior, N. (2015). "Energy analysis for guiding the design of well systems of deep Enhanced Geothermal Systems". *Energy* (93), pp.1173-1188.

Chu, Y., Li, M., Pedro, H. T. C., and Coimbra, C. F. M. (2015) "Real-time Prediction Intervals for Intra-hour DNI Forecasts." *Renewable Energy* (83) pp.234-244.

Li, M. and Lior, N. (2015) "Analysis of Hydraulic Fracturing and Reservoir Performance in Enhanced Geothermal Systems." J*ournal of Energy Resources Technology*, 137(4), 041203.

Li, M., Hu, H. H. and Bau, H. H. (2015) "Range of Validity of a Simplified Model for Diffuse Charge Dynamics. " *Electroanalysis*, 27(2), 473-484.

Li, M., Hu, H. H., and Bau, H. H. (2015) "Capacitive charging and desalination dynamics of a packed-bed reactor." *Physical Chemistry Chemical Physics*, 17(11), 7181-7195.

Chu, Y., Pedro, H. T. C., Li, M., and Coimbra, C. F. M. (2015) "Real-Time Forecasting of GHI and DNI Solar Ramps with Smart Image Processing." *Solar Energy* (114) pp.91-104.

Li, M. and Lior, N. (2014) "Comparative Analysis of Power Plant Options for Enhanced Geothermal Systems (EGS)". *Energies*, 7(12), 8427-8445.

PATENTS

Li, M. and Gross, K. C. "Dequantizing Low Resolution IoT Signals to Produce High-Accuracy Prognostic Indicators." ORA180292 (Disclosure Pending, April 6, 2018).

Gross, K. C., Li, M., Wood, A. P., Jeffreys, S., Misra, A. and Fumagalli, L. "High-Fidelity Synthesis of Telemetry Time Series Signals for Expanded ML Research Opportunities." ORA 180260 (Disclosure Pending, March 19, 2018).

Gross, K. C., Li, M., and Gawlick, D., "Multivariate Memory Vectorization Technique to Facilitate Intelligent Caching in Time-Series Databases." ORA 180215 (Disclosure Pending, January 31, 2018).

Gross, K. C., Liu, Z. H., Gawlick, D., and Li, M., "MSET-based Process for Certifying Provenance of Time-Series Data in a Time-Series Database." ORA 180189 (Disclosure Pending, December 20, 2017).

Gross, K. C., Li, M. and Masoumi, T. "Bivariate Optimization Technique for Tuning SPRT Parameters to Facilitate Prognostic Surveillance of Sensor Data from Power Plants." ORA180251 (Disclosure Pending, November 28, 2017).

Gross, K. C., Li, M. and Urmanov, A. M. "Detecting Degradation in Rotating Machinery by Using the FWHM Metric to Analyze a Vibrational Spectral Density Distribution." ORA180243 (Disclosure Pending, November 22, 2017).

Gross, K. C., Li, M. and Wood, A. P. "Hybrid Clustering-partitioning Technique that Optimizes Accuracy and Compute Cost for Prognostic Surveillance of Sensor Data." ORA180084 (Disclosure Pending, November 6, 2017).

Gross, K. C., Li, M. and Franklin, B. P. "Optimal Short-term Loadshape Forecasting for Smart Meter Electricity Signals." ORA180084 (Disclosure Pending, September 26, 2017).

ABSTRACT OF THE DISSERTATION

Spectral Modeling of Solar and Atmospheric Radiation for Solar Power Integration

by

Mengying Li

Doctor of Philosophy in Engineering Sciences (Mechanical Engineering)

University of California San Diego, 2018

Professor Carlos F. M. Coimbra, Chair

Atmospheric longwave irradiance (LW, with wavenumbers ranging from 0 ~ 2,500 cm^{-1}) and solar shortwave irradiance (SW, wavenumbers ranging from 2,500 ~ 40,000 cm^{-1}) determine the radiative balance in the atmosphere. The balance between these radiative flux contributions is also essential in the design and operation of cooling systems, including evaporative cooling towers, passive dry fans, and optically selective materials, among many other natural and engineered surfaces exposed to solar and atmospheric radiation. Large scale solar farms interact with the local atmosphere through greenhouse gases emission offset and by replacing surface albedo with materials that respond to radiation very differently than soil or vegetation. Solar photovoltaic (PV) farms are highly absorbing (lower albedo) while concentrated solar power (CSP) farms are highly reflective (higher albedo) when compared to the ground where they are usually deployed. This work employs detailed and comprehensive spectral radiative models to calculate LW and SW through the atmosphere for different ground surfaces in order to quantify local interactions caused by the different

boundary conditions for a model of the atmosphere.

First, existing data-driven empirical models for determination of the surface downwelling longwave irradiance (DLW) are reviewed and recalibrated, and a more accurate comprehensive empirical model is proposed. The broadband empirical model then serves as a benchmark to validate a Line-by-Line (LBL) spectral radiative model that is able to capture details of the highly wavenumber-dependent nature of the irradiance fluxes. For the atmospheric longwave spectrum that is emitted and absorbed by gases, aerosols, clouds and the ground, a high-resolution two-flux model with a recursive scattering method is developed. For the shortwave (solar) part of the spectrum, which includes scattering from atmospheric constituents and the ground, comprehensive Monte-Carlo LBL simulations are used.

The LW spectral model is then used to quantify the contribution of each atmospheric constituent to DLW as well as the spectral and vertical distribution of LW irradiance. The SW spectral model is used to quantify the albedo replacement effects of PV and CSP farms on local SW irradiance field. A thermal balance accounting for both longwave and shortwave irradiance is then performed for both PV and CSP surfaces. In general, CSP farms reduce while PV farms increase ground temperatures with respective changes in relative humidity. The change in temperature is a function of solar zenith angle, column water vapor content, aerosol optical depth, cloud optical depth and cloud fraction. This work then quantifies the temperature anomaly due to albedo replacement as function of these parameters. A hybrid solar farm design to minimize both local thermal effects and operational variability is proposed.

Chapter 1

Introduction

1.1 Motivation and objectives

Absorption and scattering of shortwave solar irradiance (SW, wavenumber between 2,500 and 40,000 cm^{-1}) in the Earth's atmosphere is balanced by absorption, emission, and scattering of longwave radiation (LW, wavenumber between 0 and 2,500 cm^{-1}) [12]. This balance between the shortwave radiation and the longwave radiation determines the temperature structure of the atmosphere and local temperature values on Earth's surface [13]. The SW and LW balance is essential for understanding climate change, but also for the thermal design of radiant cooling systems, cooling towers, solar power plants, and of the built environment in general [14–16].

Current interest in the optical designs of passive cooling devices [17–20] that take advantage of atmospheric windows to reject heat to outer space requires detailed balance between the incoming thermal radiation from the atmosphere and the outer space and the outgoing emissive power from the coolers in order to calculate the equilibrium temperatures and cooling efficiencies. These figures of merit (equilibrium temperatures and cooling efficiencies) depend on the local atmospheric conditions, which include the convective environment around the device and the downwelling radiative flux from the atmosphere. The convective contribution can be minimized by design, but the thermal radiation from the atmosphere (so called sky radiation) is geometrically constrained by the ability of passive cooling devices to radiate directly to outer space. Absorption bands of water vapor dominate the absorption and emission of infrared radiation in the atmosphere when conditions are wet (high relative humidity). When the relative humidity is low, other contributors such as CO_2 and aerosols contribute in a non-negligible way through specific bands of the spectrum to the overall thermal balance of the passive cooling devices. Therefore, a detailed spectral model for the longwave radiative transfer in the atmosphere is in need to calculate the thermal balances of such optically selective devices.

Two distinct solar power technologies have emerged as most competitive in the renewable energy market of utility scale solar plants: direct photovoltaic (PV) conversion and concentrated solar power (CSP) using heliostat fields to direct solar radiation to a central boiler. In addition to greenhouse gas emission offset, large scale solar farms also interact with the atmosphere through surface albedo replacement. While both PV and CSP technologies affect the local environment, the extent in which they do so has not been studied in detail. Thus a spectrally resolved shortwave radiative model is needed to quantitatively evaluate the effects of albedo replacement on the local shortwave radiative exchange between the ground and the atmosphere.

Therefore, to better understand the thermal balances of the Earth-atmosphere system, passive cooling devices and solar power farms, the objective of this research is to develop detailed radiative model to simulate the shortwave solar and longwave atmospheric radiative transfer in the atmosphere, with and without the presence of clouds. The model is validated against ground measurements and other radiative models for varies meteorological conditions. By comparing the modeling results with ground telemetry, representative cloud characteristics (cloud optical depth, base height and thickness) for given surface conditions are proposed. Thus a complete spectral model is presented that allows for determination of longwave and shortwave irradiance and can be used for a wide range of meteorological conditions.

With the developed radiative model, the albedo replacement effects of large scale PV and CSP farms can be qualified for varies conditions. In addition, the model also serves as a valuable tool to analysis the contribution of each atmospheric constituent to the thermal balance of the Earth-atmosphere system, for seven critical bands of the infrared spectrum. Furthermore, the determination of thermal equilibrium temperatures for radiative cooling devices, also requires knowledge of the spectral atmospheric solar and longwave radiation. The modeling results enable direct calculation of the equilibrium temperature and cooling efficiency of passive cooling devices in terms of meteorological conditions observed at the surface level.

1.2 Introductory methods

Some common methodologies and terms used in future chapters are presented in this section.

1.2.1 Characteristics of longwave and shortwave radiation

Electromagnetic radiation is characterized by its wavelength/wavenumber/frequency [21]. By definition, wavelength λ, wavenumber ν and frequency ν_f are related as,

$$\lambda = \frac{1}{\nu} = \frac{c}{\nu_f} \tag{1.1}$$

where c is the speed of light. The wavenumber is used in future chapters unless stated otherwise.

The monochromatic emissive intensity of a black surface, $I_{b\nu}$, as the radiant power emitted per unit area of surface per unit solid angle per unit wavenumber, is expressed by Planck's law,

$$I_b(\nu, T) = \frac{2hc^2\nu^3}{\exp\left(\frac{hc\nu}{k_B T}\right) - 1}, \tag{1.2}$$

where ν ($\mathrm{m^{-1}}$) is wavenumber, $h = 6.626 \times 10^{-34}$ J s is Planck's constant, $c = 3 \times 10^8$ $\mathrm{m\,s^{-1}}$ is the speed of light and $k_B = 1.38 \times 10^{-23}$ $\mathrm{J\,K^{-1}}$ is the Boltzmann constant.

The solar irradiance is emitted by the Sun while atmospheric longwave irradiance is emitted by gases and surfaces at a temperature of 200 to 320 K [21]. Figure 1.1 plots the monochromatic emissive power of a black surface at various temperatures according to Planck's law. For the solar irradiance, 2000 ASTM Standard Extraterrestrial Spectrum is used [22]. As shown in Fig. 1.1, atmospheric longwave irradiance is mostly in the spectral range from 0 to 2,500 $\mathrm{cm^{-1}}$ while solar shortwave irradiance is from 2,500 to 40,000 $\mathrm{cm^{-1}}$.

Therefore, the longwave irradiance (LW) referred in this work is the emitted radiation from atmosphere constituents and the Earth's surface, in the spectral range of 0 to 2,500 $\mathrm{cm^{-1}}$. The solar shortwave irradiance (SW) is the emitted radiation from the Sun that in the spectral range of 2,500 to 40,000 $\mathrm{cm^{-1}}$. The emission by the atmosphere and Earth is assumed to be diffuse (no preferable direction) while the solar irradiance is highly directional. The LW transfer in the atmosphere includes processes of emission, absorption, scattering/reflection. While for SW, the processes involves only absorption and scattering/reflection.

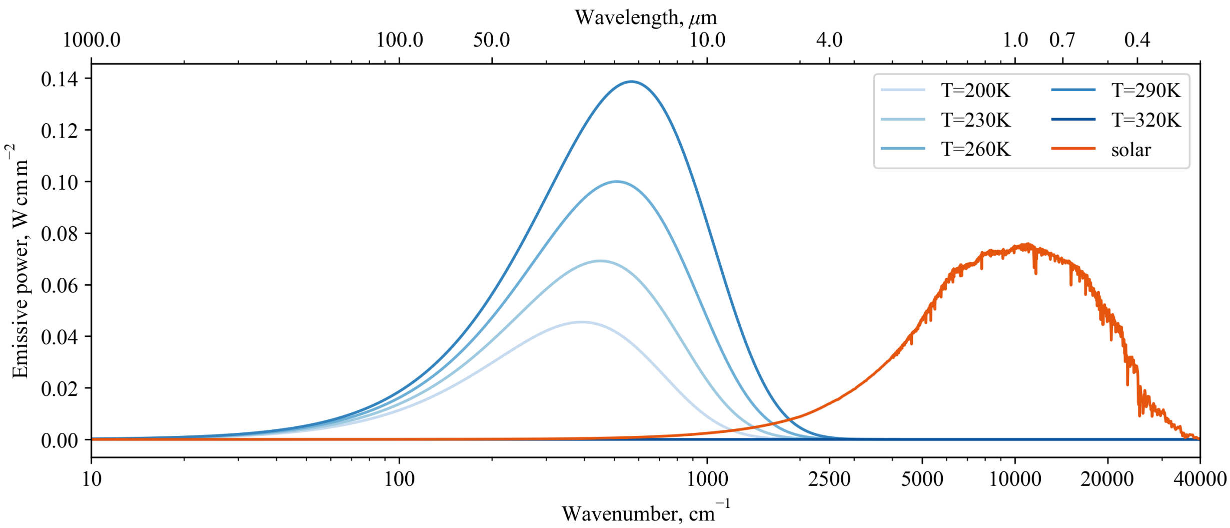

Figure 1.1: Monochromatic emissive power of a black surface at various temperatures according to Planck's law. The 2000 ASTM Standard Extraterrestrial Spectrum is also plotted [22].

1.3 Components of solar radiation

The solar radiation incident on the top of atmosphere (TOA) is parallel with the direction being defined by a solar zenith angle θ_z and an azimuth angle θ_{az}. Once enters the atmosphere, some photons are scattered and some are absorbed by gas molecules, aerosols and clouds. The solar radiation incident on the Earth's surface thus consists of both a direct (in the direction of solar rays) and a diffuse component (scattered out of the direction of solar rays), as shown in Fig. 1.2. When measured on the ground, the Direct Normal Irradiance (DNI) is the direct component, defined as the solar radiation received by a surface placed perpendicular (or normal) to the extraterrestrial solar rays. The Diffuse Horizontal Irradiance (DHI) quantifies the diffuse component, which is defined as the solar radiation received by a surface that does not in the direction of extraterrestrial solar rays. The global horizontal irradiance (GHI) is the combination of both direct and diffuse components, which is defined as the total solar radiation received by a surface placed horizontal on the ground,

$$\mathrm{GHI} = \mathrm{DNI} \cos\theta_z + \mathrm{DHI}. \tag{1.3}$$

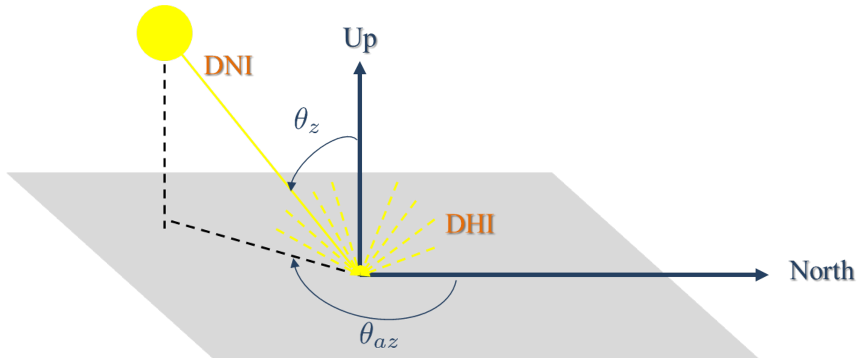

Figure 1.2: Illustration of solar zenith angle, azimuth angle, and radiation components.

1.3.1 Clear-sky models

Clear-sky irradiance is the solar irradiance value that would be measured if no clouds were present in the atmosphere. The clear-sky models are used to calculate the clear-sky irradiance for any specific locations during any period of the year. The clear-sky model is used in this work to detect clear-sky periods from irradiance measurements for model validation purpose.

Adapted from Refs. [11, 23–26], the clear sky GHI is expressed as,

$$\mathrm{GHI}_c = c_1 E_0 \sin(\theta_e) \cdot e^{0.01A_m^{1.8} - c_2 m(f_1 + f_2(T_L - 1))} \tag{1.4}$$

where c_1, c_2, f_1 and f_2 are altitude correction coefficients; E_0 ($\mathrm{W\,m^{-2}}$) is the extraterrestrial irradiance; θ_e (rad) is the solar elevation angle, $\theta_e = \pi/2 - \theta_z$; A_m is the air mass and T_L is the Linke turbidity factor. The clear sky Direct Normal Irradiance (DNI) is expressed as,

$$\mathrm{DNI}_c = \left(0.664 + \frac{0.163}{f_1}\right) I_0 \cdot e^{-0.09A_m(T_L - 1)} \tag{1.5}$$

The altitude correction coefficients are:

$$\begin{aligned} c_1 &= 5.09 \times 10^{-5} z + 0.868 \\ c_2 &= 3.92 \times 10^{-5} z + 0.0387 \\ f_1 &= e^{-z/8000} \\ f_2 &= e^{-z/1250} \end{aligned} \tag{1.6}$$

with z (m) is the altitude. The extraterrestrial irradiance E_0 is expressed as,

$$E_0 = 1361.1\left(1 + 0.033\cos\left(\frac{2\pi}{365.25}\mathrm{DOY}\right)\right) \tag{1.7}$$

with DOY is the day of year. The air mass A_m is expressed as a function of solar elevation angle,

$$\frac{1}{A_m} = \sin\theta_e + 0.15\left(\theta_e\frac{180}{\pi} + 3.885\right)^{-1.253} \tag{1.8}$$

The Linke turbidity factor T_L is extracted from monthly Link turbidity images.

1.3.2 Assessment metrics

Four statistical metrics are implemented to assess the accuracy of the proposed models: mean biased error (MBE), root mean square error (RMSE), relative mean biased error (rMBE) and relative root mean square error (rRMSE).

$$\mathrm{MBE} = \frac{1}{K}\sum_{k=1}^{K}\left(\hat{I}_k - I_k\right) \tag{1.9}$$

$$\mathrm{RMSE} = \sqrt{\frac{1}{K}\sum_{k=1}^{K}\left(\hat{I}_k - I_k\right)^2}, \tag{1.10}$$

$$\mathrm{rMBE} = \frac{\mathrm{MBE}}{1/K\sum_{k=1}^{K} I_k} \tag{1.11}$$

$$\mathrm{rRMSE} = \frac{\mathrm{RMSE}}{1/K\sum_{k=1}^{K} I_k} \tag{1.12}$$

where K is the number of data points, $\hat{I}$ is the modeled value and I is comparison ‘ground truth’.

1.4 Nomenclature and abbreviations

The list of symbols, abbreviations and subscripts used in this work is presented in Tables 1.1 to 1.3 for easier reference.

Table 1.1: List of symbols used in this work.

Symbol	Description and unit
ΔH_c	cloud thickness, m
ΔI / ΔI_c / ΔI_{oc}	irradiance change by PV or CSP under partly cloudy / clear / overcast skies, W m^{-2}
ε_{sky}	effective sky emissivity
$\bar{\varepsilon}_{lw}$ / $\bar{\varepsilon}_{sw}$	spectral averaged longwave / shortwave emittance / absoptance of passive coolers
Θ	scattering zenith angle, rad
θ_e	solar elevation angle, rad
κ^*	mass absorption coefficient, cm^2 g^{-1}
κ_e / κ_a / κ_s	volumetric extinction/absorption/scattering coefficients, cm^{-1}
μ	cosine of scattering zenith angle
ν	wavenumber, cm^{-1}
ξ	random number sampled uniformly from 0 to 1
ρ_i	partial density of constituent i, g cm^{-3}
ρ_n	depolarization factor that accounts for the anisotropy of gas molecules
σ	Stefan Boltzmann constant, 5.67×10^{-8} W m^{-2} K^{-4}
σ_n	defines constant pressure coordinate
ϕ	relative humidity, %
Φ	scattering azimuth angle, rad
$\tilde{\rho}$	single scattering albedo
A_m	air mass
A_n^*	equivalent surface area for radiative transfer
c	speed of light, m s^{-1}
d	moisture content, g (kg dry air)$^{-1}$
d_b	distance to nearest boundary in the direction of photon propagation
d_c	distance to next collision, m

Table 1.1: List of symbols used in this work, continued.

Symbol	Description and unit
e_ν	energy carried by each photoh, $\mathrm{W\,cm\,m^{-2}}$
E_0	extraterrestrial irradiance, $\mathrm{W\,m^{-2}}$
F_k	King corrector factor
$\mathcal{F}_{n,j}$	transfer factor between layer n and layer j
$\mathcal{F}^{*}_{n,j}$	correct transfer factor between layer n and layer j for flux calculation
$\mathcal{F}^{**}_{n,j}$	modified transfer factor between layer n and layer j by the plating algorithm
g	scattering asymmetry factor
g_f	growth factor
G_n	irradiance of layer n, $\mathrm{W\,m^{-2}\,cm}$
h	Planck's constant, $\mathrm{J\,s}$
h_c	convective heat transfer coefficient, $\mathrm{W\,m^{-2}\,K^{-1}}$
I_b	blackbody emissive intensity, $\mathrm{W\,m^{-2}\,sr^{-1}\,cm}$
J_{sky}	the radiosity of the sky, equivalent to DLW, $\mathrm{W\,m^{-2}}$
J_n	radiosity of layer n, $\mathrm{W\,m^{-2}\,cm}$
k_B	Boltzmann constant, $\mathrm{J\,K^{-1}}$
m	refractive index
N	number of atmospheric layers
$n(r)$	size distribution of particles, $\mathrm{mole\,cm^{-4}}$
N_{nu}	number of wavenumbers
N_A	Avogadro constant, $\mathrm{mol^{-1}}$
N_b	number of photon bundles
n_s	refractive index of standard air
P_a	air pressure, Pa
P_n	pressure of layer n boundary, Pa
$P_s(T)$	saturated water vapor pressure at temperature T, Pa
P_w	partial pressure of water vapor, Pa
p_w	normalized partial pressure of water vapor at the screening level

Table 1.1: List of symbols used in this work, continued.

Symbol	Description and unit
$\bar{P}_n$	average pressure of layer n, Pa
q_n^-	downwelling flux on layer n boundary, W m^{-2}
q_n^+	upwelling flux on layer n boundary, W m^{-2}
q_{cool}	broadband passive cooling power, W m^{-2}
q_{sw}	solar irradiance, W m^{-2}
q_c	convective heat loss, W m^{-2}
q_d	conduction heat loss, W m^{-2}
q_e	electricity production, W m^{-2}
Q_e / Q_a / Q_s	extinction/absorption/scattering efficiencies
R_f	radiation field, cm^{-1}
R_u	universal gas constant, J mol^{-1} K^{-1}
r_x / r_y / r_z	photon travel direction
t	normal optical depth
T_{sky}	effective temperature of sky, K
T_{ss}	steady state temperature of passive cooler
T_a	air temperature, K
T_d	dew point, K
T_L	Linke turbidity factor
T_n	temperature of layer n boundary, K
$\bar{T}_n$	average temperature of layer n, K
w	integrated water content in a vertical air column, mm
$w_i(z)$	mixing ratio of constituent i at altitude z
x	size parameter
z	altitude, m

Table 1.2: Abbreviations used in this work.

Abbreviation	Description
AER	Atmospheric Environmental Research, Inc
AFGL	Air Force Geophysics Laboratory
AOD	Aerosol Optical Depth
ARM	August-Roche-Magnus
ASOS	Automated Surface Observing System
CALIPSO	Cloud Aerosol LIDAR and Infrared Pathfinder Satellite Observations
CBH	Cloud Base Height, m
CF	Cloud Fraction
CIRC	Continual Intercomparison of Radiation Codes
CMF	Cloud Modification Factor
COD	Cloud Optical Depth
CSP	Concentrated Solar Power
DHI	Diffuse Horizontal Irradiance, $W\,m^{-2}$
DLW	Downwelling Longwave irradiance at the surface, $W\,m^{-2}$
DNI	Direct Normal Irradiance, $W\,m^{-2}$
DOY	Day of Year
GHI	Global Horizontal Irradiance, $W\,m^{-2}$
HITRAN	HIgh Resoluton TRANsmission
ICRCCM	Intercomparison of Radiation Codes in Climate Models
IR	thermal infrared
LBL	line-by-line
LW	longwave irradiance, $W\,m^{-2}$
LWP	Liquid Water Path, $g\,cm^{-2}$
MBE	Mean Bias Error
MC	Monte Carlo

Table 1.2: Abbreviations used in this work, continued.

Abbreviation	Description
MT_CKD	Mlawer-Tobin-Clough-Kneizys-Davies
NIP	Normal Incidence Pryheliometer
NOAA	National Ocenic and Atmospheric Administration
PIR	Precision Infrared Radiometer
PV	Photovoltaic
rMBE	relative Mean Bias Error, %
RMSE	Root Mean Square Error
rRMSE	relative Root Mean Square Error, %
SURFRAD	Surface Radiation budget network
SW	shortwave irradiance, $\mathrm{W\,m^{-2}}$
TOA	top of atmosphere
UV	ultraviolet

Table 1.3: Subscripts used in this work.

Subscript	Description
aer	aerosols
c	clear sky
cld	clouds
cont	continuum absorption
frgn	foreign continuum
gas	gases
line	spectral line absorption
lw	longwave
oc	overcast sky
S	measured

Table 1.3: Subscripts used in this work, continued.

Subscript	Description
self	self continuum
ss	steady state
sw	shortwave

1.5 Dissertation structure

In Chapter 2, we review and recalibrate existing parametric models and present a novel comprehensive model for estimation of the broadband downward atmospheric longwave (DLW) radiation for clear and cloudy sky conditions.

Since the spectral characteristics of irradiance is essential to understand the contribution of atmospheric constituents as well as the interactions between optically selective materials with the atmosphere, a comprehensive spectral longwave radiative model is developed and validated in Chapter 3. The proposed parametric broadband model serves as a validation benchmark for the spectral model. The wavenumber spectral resolution of the model is 0.01 cm^{-1} and the atmosphere is represented by 18 non-uniform plane-parallel layers with pressure in each layer determined on a pressure-based coordinate system. The model utilizes the most up-to-date (2016) HITRAN molecular spectral data for 7 atmospheric gases: H_2O, CO_2, O_3, CH_4, N_2O, O_2 and N_2. The MT_CKD model is used to calculate water vapor and CO_2 continuum absorption coefficients. Longwave absorption and scattering coefficients for aerosols and clouds are modeled using Mie theory.

Chapter 4 presents analysis of atmospheric longwave radiative transfer using the spectral model proposed in Chapter 3. The analysis includes: (i) The computational performance of the spectral model; (ii) broadband, spectral and spatial contributions of atmospheric constituents to surface DLW under clear skies; (iii) vertical and spectral distribution of longwave irradiance under clear skies; (iv) the effective sky emissivity under cloudy skies; and (v) radiative cooling ability of passive cooling materials.

A comprehensive spectral radiative model for solar shortwave transfer is presented in Chapter 5, and its validation against measurements and other radiative models is also presented. In the shortwave spectrum, the continuum absorption of ozone and oxygen is added. Monte Carlo simulation is used to fully account for the anisotropic scattering of gas molecules, aerosols and cloud droplets. The thermal effects of albedo replacement of large scale PV and CSP plants are analyzed in Chapter 6 using the developed LW and SW spectral models.

Chapter 2

Data-driven modeling of longwave irradiance from the atmosphere under all sky conditions

2.1 Introduction

The downward atmospheric longwave irradiance flux (DLW, $\mathrm{W\,m^{-2}}$) is an essential component of radiative balance for solar power plants and is of great importance in meteorological and climatic studies, including the forecast of nocturnal temperature variation and cloudiness. It also plays a critical role in the design of radiant cooling systems, as well as in the modeling of weather and climate variability [27, 28], and on the determination of selective optical properties for photovoltaic panels, photovoltaic-thermal collectors, solar thermoelectricity parabolic disks, etc. [29, 30].

The downward longwave atmospheric irradiance can be measured directly by pyrgeometers. However, pyrgeometers are not standard irradiance equipment in most weather stations because pyrgeometers are relatively expensive and require extensive calibration and adjustments to exclude the LW radiation emitted by surrounding obstacles, buildings and vegetation. Spectral (line-by-line) calculations considering the interactions of LW irradiance with atmospheric molecules (such as H_2O, CO_2 and O_3), aerosols and clouds yield reasonable estimates of DLW for global calculations, but line-by-line calculations are generally too complex for meteorological or engineering use.

A simple approach to estimate DLW relies on parametric modeling of meteorological variables measured routinely at the surface level, such as screening level air temperature and relative humidity. The parametric models imply specific assumptions regarding the vertical structure of the atmosphere [31–34]. These assumptions are either explicit [32], or implicitly included in the parametric models by locally fitting coefficients [28, 33–37].

In this Chapter, we review a large number of previous models for determining the DLW radiation at the ground level, and propose a novel model for all sky conditions (diurnal and nocturnal, clear or cloudy skies).

2.2 Background

For longwave atmospheric irradiance (4 ~ 100 μm), the background atmosphere can be considered as a gray body, and the LW irradiance is approximated as a fraction of a fictional blackbody emissive power evaluated at the surface level air temperature [21]. This fraction is called the effective sky emissivity ε_{sky} and is expressed as,

$$\varepsilon_{sky} = \frac{\text{DLW}}{\sigma T_a^4} \tag{2.1}$$

where $\sigma = 5.67\times10^{-8}\,\text{W m}^{-2}\,\text{K}^{-4}$ is the Stefan-Boltzmann constant [21] and T_a (K) is the air temperature at the surface level. This balance can be used to define an effective sky temperature T_{sky} (K) by approximating the sky as a blackbody,

$$\text{DLW} = \sigma T_{\text{sky}}^4 \tag{2.2}$$

Compare Eqs. (2.1) and (2.2), the relationship between T_{sky} and ε_{sky} is,

$$T_{\text{sky}} = \varepsilon_{\text{sky}}^{1/4} T_a \tag{2.3}$$

Since ε_{sky} ranges from 0 to 1, the effective sky temperature is always lower than the surface level air temperature [21].

In the parametric modeling, the clear-sky effective emissivity of the atmosphere can be expressed as a function of screening level air temperature T_a (K), relative humidity ϕ (%) and/or other meteorological variables, including screening level partial pressure of water vapor P_w (Pa), dew point temperature T_d (K) and moisture content d (g (kg dry air)$^{-1}$),

$$\varepsilon_{\text{sky,c}} = f(T_a, \phi, P_w, T_d, d) \tag{2.4}$$

The partial pressure of water vapor P_w (Pa) and dew point temperature T_d (K) can be expressed as a function of T_a and ϕ by the Magus expressions [38],

$$P_w = 610.94\left(\frac{\phi}{100}\right)\exp\left(\frac{17.625(T_a - 273.15)}{T_a - 30.11}\right) \tag{2.5}$$

$$T_d = \frac{243.04\ \ln(P_w/610.94)}{17.625 - \ln(P_w/610.94)} + 273.15. \tag{2.6}$$

And the moisture content d (kg/(kg dry air)) can be expressed as,

$$d = \frac{P_w}{P_a - P_w}\frac{R_a}{R_w} = \frac{0.622P_w}{P_a - P_w}. \tag{2.7}$$

where P_a is the air pressure (Pa). In Section 2.4 of this work, fifteen different forms of Eq. (2.4) are compared and calibrated using measurements from seven stations across the contiguous United States, and the most accurate formula is proposed.

The presence of clouds substantially modifies the LW because the radiation emitted by water vapor and other gases in the lower atmosphere is supplemented by the emission from clouds. Therefore, under cloudy conditions, the effective sky emissivity is higher compared to clear-sky value. Parametric models can also be used to estimate all-sky condition LW with the consideration of cloud contribution,

$$\text{DLW} = f(\text{DLW}_c, \text{CF}, \text{CMF}) \tag{2.8}$$

where DLW_c (W m^{-2}) is the corresponding clear-sky DLW, CF (%) is the cloud cover fraction in the sky dome and CMF is a cloud modification factor,

$$\text{CMF} = 1 - \frac{\text{GHI}}{\text{GHI}_c}. \tag{2.9}$$

where GHI ($\mathrm{W\,m^{-2}}$) is the global horizontal solar radiation and GHI_c ($\mathrm{W\,m^{-2}}$) is the clear-sky GHI. Note that CMF only has values during the daytime. In Section 2.5, three different forms of Eq. (2.8) are compared and calibrated, and a new model is proposed to achieve higher accuracy.

Therefore, we propose and validate a new parametric modeling of DLW for clear and all-sky conditions applicable to both daytime and nighttime. We validate the model with data from seven stations over the contiguous United States, for which cloud cover fraction data is available in nearby weather stations. A detailed description of the dataset is presented in Section 2.3.

2.3 Preparation of dataset

2.3.1 Observational data

The comparison and calibration of parametric models in Section 2.4 and 2.5 are performed and validated using the radiation and meteorological measurements from the SURFRAD (Surface Radiation Budget Network) and ASOS (Automated Surface Observing System) operated by NOAA (National Oceanic and Atmospheric Administration). Currently seven SURFRAD stations are operating in climatologically diverse regions over the contiguous United States as shown in Fig. 2.1 [1]. Our fitting and validation datasets include measurements of year 2012 and year 2013 that are collected in all seven stations. Data from years 2014 and 2015 are not selected to avoid the influence of El Niño and La Niña years [39].

The seven stations, Bondville (in Illinois), Boulder (in Colorado), Desert Rock (in Nevada), Fort Peck (in Montana), Goodwin Creek (in Mississippi), Penn State University (in Pennsylvania) and Sioux Falls (in South Dakota) represent the climatological diversities, as shown in Table 2.1. Fort Peck and Sioux Falls have a cold and humid climate with annual averaged temperature and relative humidity around 7.0°C and 70%. Bondville and Penn State are cool and humid with annual averaged temperature around 11.0°C and relative humidity around 71%. Boulder has a mild climate with annual averaged temperature and relative humidity of 12.2°C and 44.7%. Goodwin Creek is warm and humid with annual averaged temperature of 16.8°C and relative humidity of 71.9%. Desert Rock has a hot and dry climate with annual averaged temperature and relative humidity of 18.8°C and 27.5%. The seven sites also covers a large altitude span that ranges from 98 m to 1689 m.

The utilized SURFRAD measurements include 1-minute averaged downwelling thermal infrared

Table 2.1: Annual average values, 25th and 75th percentile of air temperature (T_a), relative humidity (ϕ), downward atmospheric infrared irradiance (IR) of SURFRAD stations during year 2012~ 2013.

	SURFRAD Stations						
Parameters	Bondville	Boulder	Desert Rock	Fort Peck	Goodwin Creek	Penn State	Sioux Falls
Latitude (°)	40.05	40.13	36.62	48.31	34.25	40.72	43.73
Longtitude (°)	−88.37	−105.24	−116.02	−105.10	−89.87	−77.93	−96.62
Altitude (m)	213	1689	1007	634	98	376	437
Data Sampling Rate (minute)	1	1	1	1	1	1	1
Average T_a (°C)	11.8	12.2	18.8	5.9	16.8	10.7	8.3
25th Percentile of T_a (°C)	2.2	4.3	10.6	−3.8	10.0	2.1	−1.8
75th Percentile of T_a (°C)	20.9	20.6	27.1	16.5	23.9	18.9	19.1
Average ϕ (%)	70.7	44.7	27.5	68.2	71.9	71.0	72.1
25th Percentile of ϕ (%)	58.2	26.2	13.4	52.1	56.8	57.6	58.9
75th Percentile of ϕ (%)	85.6	61.2	35.5	86.4	89.9	87.4	87.9
Average IR (W/m^2)	320.7	290.4	308.0	288.9	349.7	318.0	302.4
25th Percentile of IR (W/m^2)	275.1	248.8	268.6	246.7	307.9	276.4	255.8
75th Percentile of IR (W/m^2)	370.6	331.0	342.7	331.9	396.2	366.6	354.0
	Closest ASOS stations						
	Champaign	Boulder	Desert Rock	Wolf Point INTL	Oxford	State College	Sioux Falls
Latitude (°)	40.04	40.04	36.62	48.09	34.38	40.85	43.58
Longtitude (°)	−88.28	−105.23	−116.03	−105.58	−89.54	−77.85	−96.75
Altitude (m)	163	1612	1009	605	138	378	436
Data Sampling Rate (minute)	60	20	60	60	20	20	60

Figure 2.1: Locations of the 7 SURFRAD stations used in this work [1].

(IR, W m^{-2}), direct normal solar radiation (DNI, W m^{-2}), global horizontal solar radiation (GHI, W m^{-2}), screen level air temperature (T_a, K) and relative humidity of the air (ϕ,%). The Eppley Precision Infrared Radiometer (PIR) measures the downwelling IR from the atmosphere. The spectral range of the PIR is 3 μm to 50 μm [1]. The Normal Incidence Pryheliometer (NIP) measures the DNI in the broundband spectural range from 0.28 μm to 3 μm [1]. The Spectrolab SR-75 pyranometer measures the GHI in the same spectral range as the NIP [1]. All irradiance instruments have uncertainties smaller than ± 5 W m^{-2}, and are calibrated annually. The data quality is controlled by NOAA using the methodology outlined for the Baseline Surface Radiation Network, where low quality data are deleted and questionable data are flagged (less than 1% of data). The instruments are calibrated against standards traceable to the World Radiation Center in Davos, Switzerland [1]. Questionable data falling outside of physically possible values were also flagged and deleted from our dataset. Since large amounts of measured data are used in this work, the uncertainty is statistically reduced. Less than 0.5% of the original data has been deleted for this study. The cloud fraction (CF) is obtained from closest ASOS stations (Table 2.1). ASOS network has over 3000 operational stations over the contiguous United States and its data are publicly available for download from the website of Iowa State University of Science and Technology [40]. The cloud fraction in ASOS is reported in three layers. The amount of cloud is determined by adding the total number of hits in each layer and computing the ratio of those hits to the total possible. If there is more than one layer, the ‘hits’ in the first layer are added to the second (and third) to obtain overall coverage [10]. ASOS stations measure 20-minute or 60-minute averaged text-annotated CF information while in this work, the CF is interpreted as numerical values based on Table 2.2. When CF data are in use, the 1-minute averaged SURFRAD data are interpolated to match the timestamp of the CF data by nearest neighbor interpolation.

Table 2.2: Numerical interpretation of ASOS text-annotated cloud fraction [10].

ASOS text-annotated cloud fraction (CF)	Clear	Few	Scattered	Broken	Overcast
Numerical cloud fraction (CF)	0	0.125	0.375	0.75	1

2.3.2 Selection of clear-sky periods

For the analysis of clear-sky parametric models, only clear-sky periods are selected. The clear-sky periods are defined as the periods where no cloud presents within the field of view of the radiometers. During the daytime, GHI and DNI time series are used instead of CF data because irradiance measurements are available on-site and are sampled at 1-minute intervals. The CF data have an uncertainty of ±0.125, sampled every 20 or 60 minutes and are retrieved from nearby ASOS stations. An endogenous statistical model which was originally developed by Reno et al for GHI observations [41] is used to select clear-sky periods. This method uses five criteria to compare a period of N GHI measurements to a corresponding clear-sky GHI for the same period. In this work, the clear-sky GHI and DNI values are calculated using clear-sky models adapted from Refs. [11, 23–26], which are presented in the Appendix.

The time period is deemed ‘clear’ if threshold values for all the following criteria are met when compared with clear-sky irradiance time series:

1. The difference of mean value of irradiance I and clear-sky irradiance I_c in the time series,

$$\left| \frac{1}{N}\sum_{n=1}^{N} I(t_n) - \frac{1}{N}\sum_{n=1}^{N} I_c(t_n) \right| < \theta_1 \tag{2.10}$$

2. The difference of max value of I and I_c in the time series,

$$|\max I(t_n) - \max I_c(t_n)| < \theta_2, \quad n \in [1, 2, \cdots, N] \tag{2.11}$$

3. The difference of length of the line connecting the points in the time series [11], without the consideration of the length of the time-step,

$$\left| \sum_{n=1}^{N} |s(t_n)| - \sum_{n=1}^{N} |s_c(t_n)| \right| < \theta_3 \tag{2.12}$$

where slopes $s(t_n) = I(t_n + \Delta t) - I(t_n)$ and $s_c(t_n) = I_c(t_n + \Delta t) - I_c(t_n)$.

4. The difference of maximum deviation from the clear-sky slope,

$$\max |s(t_n) - s_c(t_n)| < \theta_4, \quad n \in [1, 2, \cdots, N] \tag{2.13}$$

5. The difference of the normalized standard deviation of the slope between sequential points,

$$\left| \frac{\sqrt{\frac{1}{N-1} \sum_{n=1}^{N-1} (s(t_n) - \bar{s})^2}}{\frac{1}{N} \sum_{n=1}^{N} I(t_n)} - \frac{\sqrt{\frac{1}{N-1} \sum_{n=1}^{N-1} (s_c(t_n) - \bar{s}_c)^2}}{\frac{1}{N} \sum_{n=1}^{N} I_c(t_n)} \right| < \gamma_5 \tag{2.14}$$

Specific thresholds for both GHI and DNI are used in this work, resulting in a total of 10 criteria. A 10-minute sliding window is employed as suggested by Refs. [11, 41]. In this work, a period is classified as clear only if all 10 criteria are met for measured GHI and DNI time series in at least one sliding window around the referred period. The threshold values for GHI and DNI are obtained from Ref. [11] and tabulated in Table 2.3. The threshold values θ_1, θ_2, θ_3 and θ_4 have units of W/m^2 because they represent the differences of irradiance or slope as defined in Eqs.(10) - (13). The threshold value γ_5 is dimensionless because it represents the difference of normalized standard deviation of the slope as defined in Eq. (14).

Table 2.3: Clear-sky criteria threshold values for GHI and DNI [11]

	GHI thresholds	DNI thresholds
θ_1 (W m^{-2})	100	200
θ_2 (W m^{-2})	100	200
θ_3 (W m^{-2})	50	100
θ_4 (W m^{-2})	10	15
γ_5	0.01	0.015

During the nighttime, a period is denoted as clear if ASOS cloud fraction (CF) is zero during the whole night.

2.3.3 Measured atmospheric longwave irradiance

In Refs. [27, 37] and many others, the measurements from the PIR are used directly as the DLW irradiance. However, the Eppley PIR only measures infrared irradiance from 3 μm to 50 μm, which is a subset range of the total DLW irradiance. To account for this discrepancy, we calculate the effective sky temperature T_{sky} iteratively using the proper spectral range,

$$\text{IR} = \sigma T_{\text{sky}}^4 F_{\lambda_1-\lambda_2}(T_{\text{sky}}) \tag{2.15}$$

where IR is the measured infrared flux from PIR and $F_{\lambda_1-\lambda_2}$ is the external fraction of blackbody emission, which is calculated as,

$$F_{\lambda_1-\lambda_2}(T) = \frac{\int_{\lambda_1}^{\lambda_2} E_{b,\lambda}(T)d\lambda}{\int_0^{\infty} E_{b,\lambda}(T)d\lambda} = \frac{\int_{\lambda_1}^{\lambda_2} E_{b,\lambda}(T)d\lambda}{\sigma T^4} \tag{2.16}$$

where $\lambda_1 = 3$ μm and $\lambda_2 =$ 50 μm that match the measurement range of the Eppley PIR. The measured downward atmospheric longwave irradiance is then expressed as,

$$\text{DLW}_S = \sigma T_{\text{sky}}^4 \tag{2.17}$$

2.3.4 Assessment metrics

Four statistical metrics listed in section 1.3.2 are implemented to assess the accuracy of the parametric models.

The number of data points used in this work is tabulated in Table 2.4. The data are randomly selected from the fitting and validation datasets to include measurements from all seasons and all seven SURFRAD stations. The clear-sky data are randomly selected from the dataset when the sky is deemed clear while the all-sky data are randomly selected from the entire dataset.

All the results tabulated in the following Sections 2.4 and 2.5 are calculated based on the validation dataset (Table 2.4) while the plots illustrate only a random subset to improve the readability of the figures.

Table 2.4: The number of data points used in this work

	Fitting dataset (year 2012)	Validation dataset (year 2013)
Daytime clear-sky periods	8,287	6,912
Nigttime clear-sky periods	8,840	7,140
All day clear sky periods	17,127	14,052
Daytime all sky condition periods	4,719	5,403
Nighttime all sky condition periods	4,185	4,614
All day all sky condition periods	8,904	10,017

2.4 Parametric models for clear-sky conditions

2.4.1 Calibration of selected models

Since 1910s, researchers have developed several parametric models to quantify the relationship between the clear-sky effective sky emissivity and ground level meteorologic information. The meteorologic information includes the air temperature T_a (K), the relative humidity ϕ (%), water vapor pressure P_w (Pa), dew point temperature T_d (K), integrated water content in a vertical air column w (mm) and moisture content d (g (kg dry air)$^{-1}$).

Selected parametric clear-sky models are presented in chronological order in Table 2.5. The numerical coefficients in each model were originally fitted using local meteorologic measurements. A grid search method is used to calibrate the coefficients of the parametric models based on our dataset. The grid search method lays the coefficient values on a grid, and each parametric model is evaluated on the fitting dataset using a combination of coefficients at a time. Then the combination of coefficients that results in the smallest RMSE is selected as the calibrated set of coefficients. Clear-sky SURFRAD data collected in year 2012 is used as fitting dataset and data collected in year 2013 is used as a validation dataset to evaluate the performance of original and calibrated models.

2.4.2 Results and discussions

Calibration increases the accuracy of all models

Figure 2.2 presents a comparison between the original and calibrated Brunt model. Both the bias and absolute errors are reduced by the calibration and the reduction applies for all other models. The MBE, RMSE, rMBE and rRMSE of those models in calculating DLW before and after the calibrations are presented

Table 2.5: Parametric models for clear skies

Model	Year	Variables	Formulation	Original Parameters
Brunt [31]	1932	P_w (hPa)	$\varepsilon_{sky} = c_1 + c_2\sqrt{P_w}$	$c_1 = 0.52$, $c_2 = 0.065$
Swinbank [42]	1963	T_a (K)	$\varepsilon_{sky} = c_1 T_a^{c_2}$	$c_1 = 9.365 \times 10^{-6}$, $c_2 = 2$
Idso and Jackson [43]	1969	T_a (K)	$\varepsilon_{sky} = 1 - c_1 \exp[c_2(273 - T_a)^{c_3}]$	$c_1 = 0.261$, $c_2 = -7.77 \times 10^{-4}$, $c_3 = 2$
Brutsaert [32]	1975	P_w (hPa), T_a (K)	$\varepsilon_{sky} = c_1 (P_w/T_a)^{c_2}$	$c_1 = 1.24$, $c_2 = 1/7$
Satterlund [44]	1979	P_w (hPa),T_a (K)	$\varepsilon_{sky} = c_1[1 - \exp(-P_w^{T_a/c_2})]$	$c_1 = 1.08$, $c_2 = 2016$
Idso [45]	1981	P_w (hPa),T_a (K)	$\varepsilon_{sky} = c_1 + c_2 P_w \exp(c_3/T_a))$	$c_1 = 0.70$, $c_2 = 5.95 \times 10^{-5}$, $c_3 = 1500$
Berdahl and Fromberg [35]	1982	T_d (°C)	$\varepsilon_{sky} = c_1 + c_2 T_d$ (daytime)	$c_1 = 0.727$, $c_2 = 0.0060$
Berdahl and Martin [46]	1984	T_d (°C)	$\varepsilon_{sky} = c_1 + c_2(T_d/100) + c_3(T_d/100)^2$	$c_1 = 0.711$, $c_2 = 0.56$, $c_3 = 0.73$
Prata [47]	1996	w ($\mathrm{g\,cm^{-2}}$), P_w (hPa),T_a (K)	$\varepsilon_{sky} = 1 - (1+w)\exp(-\sqrt{(}c_1 + c_2 w))$, $w = c_3 \frac{P_w}{T_a}$	$c_1 = 1.2$, $c_2 = 3$, $c_3 = 46.5$
Dilley and O'Brien [48]	1998	T_a (K), w ($\mathrm{kg\,m^{-2}}$)	$\varepsilon_{sky} = \left(c_1 + c_2\left(\frac{T_a}{273.16}\right)^6 + c_3\sqrt{\frac{w}{25}}\right)/\sigma T_a^4$, $w = 4.65 \frac{P_w}{T_a}$	$c_1 = 59.38$, $c_2 = 113.7$, $c_3 = 96.96$
Niemelä [49]	2001	P_w (hPa)	$\varepsilon_{sky} = c_1 + c_2(P_w - c_3)$, if $P_w \geq c_3$ $\varepsilon_{sky} = c_1 - c_2(P_w - c_3)$, if $P_w < c_3$	$c_1 = 0.72$, $c_2 = 0.009$, $c_3 = 2$ $c_1 = 0.72$, $c_2 = 0.076$, $c_3 = 2$
Iziomon [50]	2003	P_w (hPa), T_a (K)	$\varepsilon_{sky} = 1 - c_1 \exp\left(\frac{-10P_w}{T_a}\right)$	$c_1 = 0.35$
Ruckstuhl et al [33]	2007	w (mm), d ($\mathrm{g\,kg^{-1}}$)	$\varepsilon_{sky} = c_1 w^{c_2}$, $w = c_3 d - c_4$	$c_1 = 147.8$, $c_2 = 0.26$, $c_3 = 2.40$, $c_4 = 1.60$
Dai and Fang [51]	2014	P_w (hPa), P_a (hPa)	$\varepsilon_{sky} = (c_1 + c_2 P_w^{c_3})(P_a/1013)^{c_4}$	$c_1 = 0.48$, $c_2 = 0.17$, $c_3 = 0.22$, $c_4 = 0.45$
Carmona [28]	2014	T_a (K), ϕ (%)	$\varepsilon_{sky} = -c_1 + c_2 T_a + c_3\phi$	$c_1 = 0.34$, $c_2 = 3.36 \times 10^{-3}$, $c_3 = 1.94 \times 10^{-3}$

in Table 2.6. As shown in Table 2.6, after the calibration of coefficients, the RMSE of all models improved by 2.8% ~ 58.9% and some formulas are substantially better than others. The Swinbank, Idso and Jackson and Ruchstuhl models have errors around twice of that of other models, indicating that these three formulas are not recommended for future use.

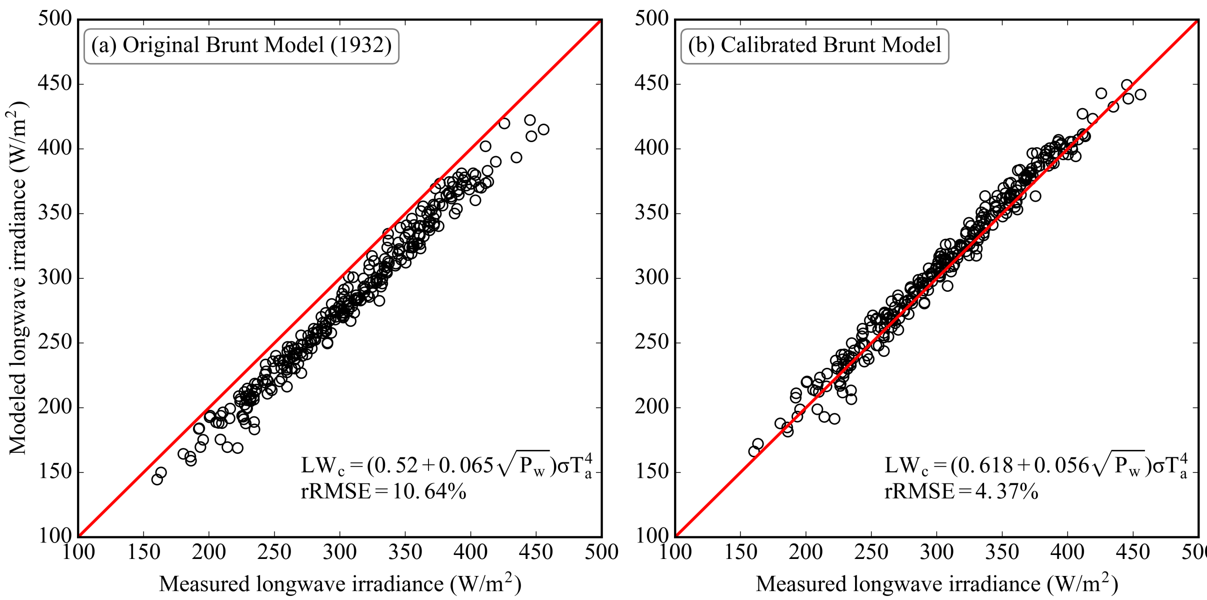

Figure 2.2: Modeled LW with respect to measured LW. (a) Original Brunt model; (b) Calibrated Brunt model.

Different functional forms corresponding to the same model

Even though the parametric models described above have different functional forms and different coefficients as shown in Table 2.5, most models have nearly identical accuracies after the calibration of their coefficients as shown in Table 2.6. Further examination of the modeling results show that most of the examined parametric models correspond to only a few independent model families. As shown in Fig.2.3, DLW_c calculated by calibrated Brunt, Brutsaert, Berdahl and Fromberg, Berdahl and Martin, Prata, Dilley and O'Brien, Niemelä, Iziomon, and Dai and Fang models correspond to the same model family. The models proposed by Idso, Satterlund and Carmona also yield identical values of DLW_c after the calibration and they collapse to another model family. The different functional forms relate only to the use of different variables that are not independent from each other. In other words, each model family represents the same model expressed in terms of either mutually dependent or redundant variables. In these cases, the increased

Table 2.6: LW_c modeling errors of original and calibrated clear-sky models

Model	Original Models MBE ($W\,m^{-2}$)	Original Models RMSE ($W\,m^{-2}$)	Original Models rMBE (%)	Original Models rRMSE (%)	Calibrated Parameters	Calibrated Models MBE ($W\,m^{-2}$)	Calibrated Models RMSE ($W\,m^{-2}$)	Calibrated Models rMBE (%)	Calibrated Models rRMSE (%)
Brunt [31]	29.54	32.24	9.75	10.64	$c_1 = 0.618$, $c_2 = 0.056$	−0.94	13.24	−0.31	4.37
Swinbank [42]	3.70	30.30	1.22	10	$c_1 = 9.169\times10^{-6}$, $c_2 = 2$	−2.70	29.45	−0.89	9.72
Idso and Jackson [43]	9.63	30.51	3.18	10.07	$c_1 = 0.242$, $c_2 = -1.8\times10^{-4}$	−0.52	25.81	−0.17	8.52
Brutsaert [32]	−18.91	23.69	−6.24	7.82	$c_1 = 1.168$, $c_2 = 1/9$	−1.94	13.54	−0.64	4.47
Satterlund [44]	5.42	16.36	1.79	5.4	$c_1 = 1.02$, $c_2 = 1564.94$	−1.12	14.63	−0.37	4.83
Idso [45]	5.21	14.03	1.72	4.63	$c_1 = 0.685$, $c_2 = 3.2\times10^{-5}$, $c_3 = 1699$	−0.39	13.18	−0.13	4.35
Berdahl and Fromberg [35]	−15.21	20.06	−5.02	6.62	$c_1 = 0.764$, $c_2 = 5.54\times10^{-3}$	−1.00	13.57	−0.33	4.48
Berdahl and Martin [46]	−18.36	22.42	−6.06	7.4	$c_1 = 0.758$, $c_2 = 0.521$, $c_3 = 0.625$	−0.70	13.24	−0.23	4.37
Prata [47]	−6.91	15.00	−2.28	4.95	$c_1 = 1.02$, $c_2 = 3.25$, $c_3 = 52.7$	−1.67	13.15	−0.55	4.34
Dilley and O'Brien [48] [48]	−19.81	24.03	−6.54	7.93	$c_1 = 55.08$, $c_2 = 125.03$, $c_3 = 108.83$	−0.33	12.48	−0.11	4.12
Niemelä [49]	2.85	14.88	0.94	4.91	$c_1 = 0.712$, $c_2 = 8.7\times10^{-3}$, $c_3 = 1.52$ $c_1 = 0.66$, $c_2 = -0.0107$, $c_3 = 1.52$	−1.85	13.82	−0.61	4.56
Iziomon [50]	−15.91	20.66	−5.25	6.82	$c_1 = 0.33$, $c_2 = 13.78$	−1.24	13.15	−0.41	4.34
Ruckstuhl et al [33]	−42.87	56.62	−14.15	18.69	$c_1 = 184$, $c_2 = 0.2$, $c_3 = 3.1$, $c_4 = 0.5$	4.97	34.87	1.64	11.51
Dai and Fang [51]	−24.93	28.78	−8.23	9.5	$c_1 = 0.32$, $c_2 = 0.34$, $c_3 = 0.16$, $c_4 = 0.2$	−2.36	13.24	−0.78	4.37
Carmona [28]	−21.06	25.33	−6.95	8.36	$c_1 = -0.503$, $c_2 = 4.04\times10^{-3}$, $c_3 = 2.4\times10^{-3}$	0.39	13.12	0.13	4.33

complexity of the functional relationships does not yield higher accuracy. Since the calibrated Brunt model has the simplest functional form (only one variable with two coefficients) and remains the most accurate, we recommend its use as the baseline model for further developments.

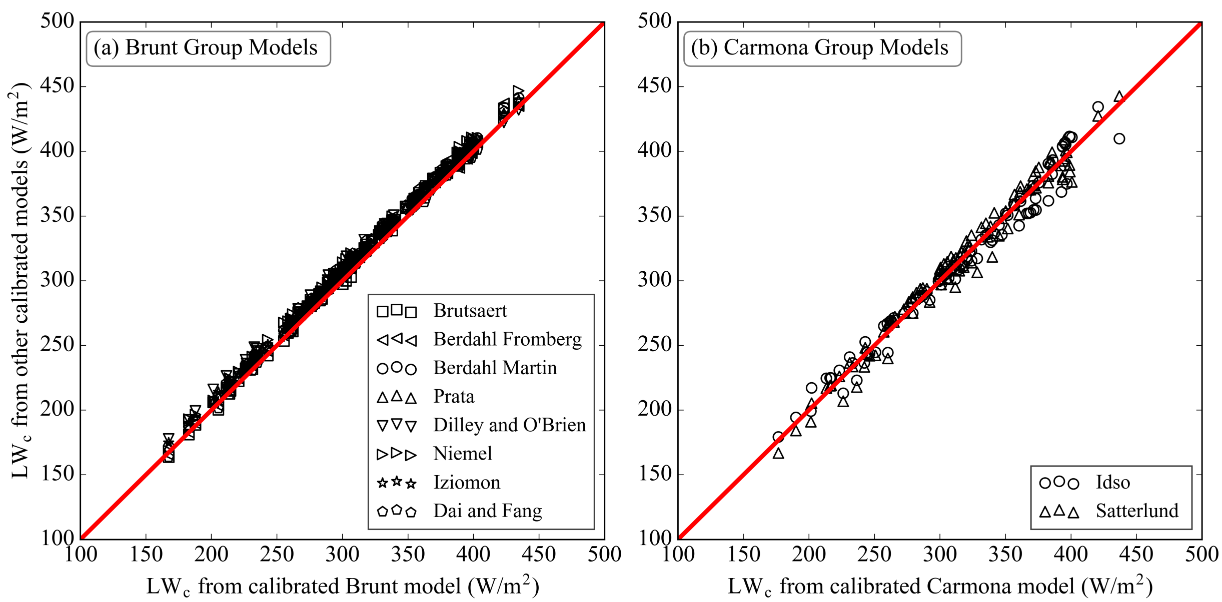

Figure 2.3: Comparison of different calibrated clear-sky models (a) The Brunt model group; (b)The Carmona model group.

The nighttime clear sky is more emissive than the daytime

By comparing the effective clear sky emissivity during the nighttime and the daytime, a positive difference is observed, indicating that the clear sky is more emissive during the night. Fig.2.4 shows that on average, the nighttime emissivity is around 0.035 higher than the daytime values under the same ground-level partial pressure of water vapor. This behavior is related to the formation of inversion layers during clear nights where the surface temperature is reduced compared with the temperature aloft [35]. The day and night difference is observed by other studies as well [27, 35, 52].

For energy balance applications in solar engineering, the effective emissivity during the daytime is more favorable while for nighttime passive cooling applications, the effective emissivity during the nighttime is more favorable. Therefore, the parametric clear-sky Brunt models for both daytime and nighttime are proposed as,

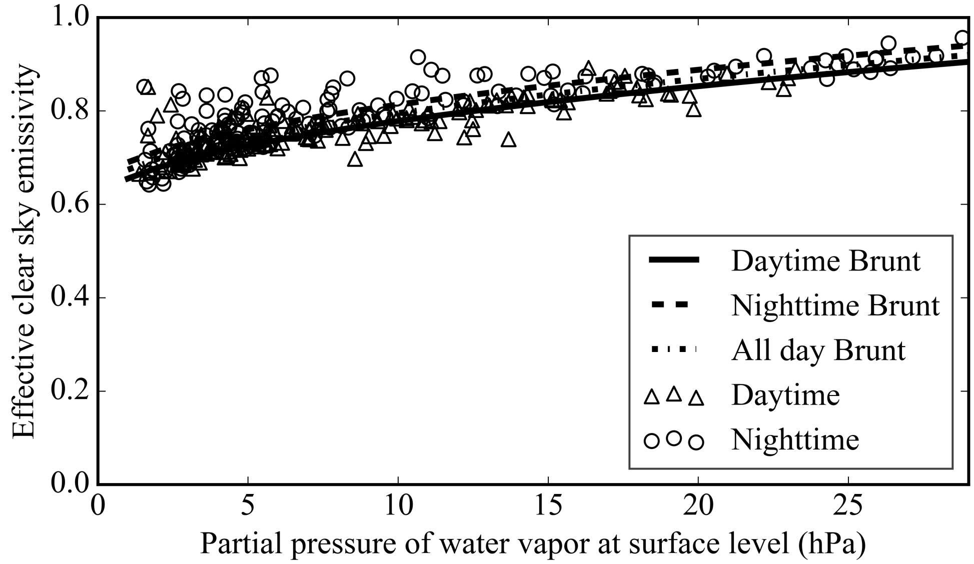

Figure 2.4: Comparison of clear sky emissivity during the nighttime and during the daytime.

$$\text{Daytime clear-sky model:} \qquad \varepsilon_{\text{sky},c} = 0.598 + 0.057\sqrt{P_w} \tag{2.18a}$$

$$\text{Nighttime clear-sky model:} \qquad \varepsilon_{\text{sky},c} = 0.633 + 0.057\sqrt{P_w} \tag{2.18b}$$

$$\text{All day clear-sky model:} \qquad \varepsilon_{\text{sky},c} = 0.618 + 0.056\sqrt{P_w} \tag{2.18c}$$

Table 2.7 presents the modeling errors of time specified Brunt models. Daytime Brunt model has the highest accuracy during the daytime and nighttime Brunt model has the highest accuracy during nighttime. For applications that require both daytime and nighttime DLW$_c$ information, the all-sky Brunt model is the most accurate model to use.

2.5 Parametric models for all-sky conditions

2.5.1 Calibration of selected and proposed models

Under all-sky conditions, the downward longwave irradiance is increased by the radiation emission from clouds (liquid water and/or ice). Therefore, the all-sky parametric models need to include cloud

Table 2.7: DLW_c modeling errors of time specified Brunt models. Bold values indicate best performance.

	Model	Daytime Brunt, Eq. (2.18a)	Nighttime Brunt, Eq. (2.18b)	All-day Brunt, Eq. (2.18c)
Daytime clear-sky periods	MBE ($\mathrm{W\,m^{-2}}$)	−1.99	12.18	4.98
	RMSE ($\mathrm{W\,m^{-2}}$)	8.54	15.16	9.86
	rMBE (%)	−0.65	3.95	1.61
	rRMSE (%)	2.77	4.91	3.2
Nighttime clear-sky periods	MBE ($\mathrm{W\,m^{-2}}$)	−13.19	0.01	−6.68
	RMSE ($\mathrm{W\,m^{-2}}$)	19.42	14.57	15.85
	rMBE (%)	−4.43	0.00	−2.24
	rRMSE (%)	6.53	4.89	5.33
All day clear-sky periods	MBE ($\mathrm{W\,m^{-2}}$)	−7.68	6.00	−0.94
	RMSE ($\mathrm{W\,m^{-2}}$)	15.08	14.86	13.25
	rMBE (%)	−2.54	1.98	−0.31
	rRMSE (%)	4.98	4.91	4.37

information such as cloud cover fraction (CF) or cloud modification factor (CMF). In 1999, Crawford and Duchon [53] developed a parametric model that accounts for the emission of clouds in the form of,

$$\mathrm{DLW} = \mathrm{DLW}_c(1 - c_1\mathrm{CF}^{c_2}) + c_3\mathrm{CF}^{c_4}\sigma T_a^4 \tag{2.19}$$

In the original Crawford and Duchon model, all the four coefficients $c_1 \sim c_4$ are equal to 1. Other parametric models proposed by Refs. [54, 55] would also collapse to this form with different $c_1 \sim c_4$.

A parametric model for daytime all-sky condition was proposed by Bilbao et al (2007) as [37],

$$\mathrm{DLW} = \mathrm{DLW}_c(1 + c_1\mathrm{CMF}^{c_2}) \tag{2.20}$$

where c_1 and c_2 are coefficients regressed from local measurements.

Another model proposed by Aldo et al (2012) has the functional relation [27]

$$\mathrm{DLW} = \mathrm{DLW}_c(c_1 - c_2(1 - \mathrm{CMF})) \tag{2.21}$$

where c_1 and c_2 are locally fitted coefficients as well.

To account for the modification of DLW due to clouds, we propose a comprehensive new model as shown in Eq.(2.22) where CMF or CF equals to zero corresponds to clear (cloud free) conditions. The first term on the right-hand side of Eq.(2.22) accounts for the absorption of DLW by clouds and the second term accounts for the emission of DLW by clouds. The alteration of vertical atmospheric temperature and relative humidity profile by clouds is represented by using screening level temperature T_a and relative humidity ϕ as parameters in the second right-hand side term of Eq.(2.22). Although many functional forms are possible for the weighing functions, we opted for a simple linear to power-law scale dependency, which fits well the data.

$$\text{Daytime model:} \qquad \mathrm{DLW} = \mathrm{DLW}_c(1 - c_1\mathrm{CMF}^{c_2}) + c_3\sigma T_a^4\mathrm{CMF}^{c_4}\phi^{c_5} \tag{2.22a}$$

$$\text{All day model:} \qquad \mathrm{DLW} = \mathrm{DLW}_c(1 - c_1\mathrm{CF}^{c_2}) + c_3\sigma T_a^4\mathrm{CF}^{c_4}\phi^{c_5} \tag{2.22b}$$

The three previously proposed models (Eq. (2.19)~ (2.21)) with their original coefficients are tested on the validation sets and their coefficients are recalibrated by a grid search method to improve their accuracy for comparison. The coefficients of the proposed new models (Eq. (2.22)) are fitted to the *fitting* dataset and validated against the *validation* dataset.

2.5.2 Results and discussions

Using the calibrated clear-sky Brunt model (Eq. (2.18)) to calculate the clear-sky DLW_c, the MBE, RMSE, rMBE and rRMSE of all-sky models in modeling LW are presented in Table 2.8. The accuracies of Carwford and Duchon, Bilbao and Aldos model increase after the calibration of coefficients. During the daytime periods, the proposed all-sky model outperforms the three other models and has 15.3% ~ 31.8% lower RMSE. If GHI irradiance measurements are available, using CMF has 7.5% lower RMSE than using CF. During the nighttime, the proposed model (Eq.(2.22b)) has 1.3% lower RMSE than the calibrated Crawford and Duchon model. During all day periods, the proposed model (Eq.(2.22b)) has 3.8% lower RMSE than the calibrated Carwford and Duchon model. For different applications that require daytime and/or nighttime DLW information, specific values of $c_1 \sim c_5$ of proposed model can be selected from Table 2.8.

Table 2.8: LW modeling errors of original and calibrated all-sky models. Bold values indicate best performance.

	Daytime					**Nighttime**		**All day**	
Model	Eq.(2.19)	Eq.(2.20)	Eq.(2.21)	Eq.(2.22a)	Eq.(2.22b)	Eq.(2.19)	Eq.(2.22b)	Eq.(2.19)	Eq.(2.22b)
Original Coefficients	$c_1 = 1$ $c_2 = 1$ $c_3 = 1$ $c_4 = 1$	$c_1 = 0.273$ $c_2 = 0.809$	$c_1 = 1.202$ $c_2 = 0.303$	–	–	$c_1 = 1$ $c_2 = 1$ $c_3 = 1$ $c_4 = 1$	–	$c_1 = 1$ $c_2 = 1$ $c_3 = 1$ $c_4 = 1$	–
MBE ($\mathrm{W\,m^{-2}}$)	−2.89	−0.75	−36.55	–	–	0.31	–	−1.46	–
RMSE ($\mathrm{W\,m^{-2}}$)	23.26	30.77	45.81	–	–	21.21	–	22.38	–
rMBE (%)	−0.86	−0.22	−10.93	–	–	0.1	–	−0.45	–
rRMSE (%)	6.96	9.2	13.71	–	–	6.78	–	6.93	–
Calibrated Coefficients	$c_1 = 0.48$ $c_2 = 0.89$ $c_3 = 0.57$ $c_4 = 0.92$	$c_1 = 0.23$ $c_2 = 1$	$c_1 = 1.2$ $c_2 = 0.17$	$c_1 = 1.29$ $c_2 = 0.8$ $c_3 = 0.7$ $c_4 = 0.78$ $c_5 = 0.13$	$c_1 = 0.96$ $c_2 = 1.2$ $c_3 = 0.49$ $c_4 = 1.09$ $c_5 = 0.15$	$c_1 = 0.82$ $c_2 = 1.13$ $c_3 = 0.83$ $c_4 = 1.11$	$c_1 = 0.77$ $c_2 = 0.8$ $c_3 = 0.39$ $c_4 = 0.8$ $c_5 = 0.16$	$c_1 = 0.82$ $c_2 = 1.24$ $c_3 = 0.83$ $c_4 = 1.21$	$c_1 = 0.78$ $c_2 = 1$ $c_3 = 0.38$ $c_4 = 0.95$ $c_5 = 0.17$
MBE ($\mathrm{W\,m^{-2}}$)	−5.46	−11.4	−6.9	−3.09	−5.88	−2.57	−2.43	−4.94	−4.38
RMSE ($\mathrm{W\,m^{-2}}$)	23.14	28.73	27.38	19.59	21.18	20.59	20.32	21.73	20.91
rMBE (%)	−1.63	−3.41	−2.06	−0.92	−1.76	−0.82	−0.78	−1.53	−1.35
rRMSE(%)	6.92	8.59	8.19	5.86	6.34	6.58	6.49	6.72	6.47

2.6 Conclusions

Under clear-sky conditions, fifteen parametric models proposed in the bibliography to estimate downward atmospheric longwave irradiance (DLW_c) are compared and recalibrated using data collected from 7 climatologically diverse SURFRAD stations over the contiguous United States. All fifteen models achieve 2.8% ~ 58.9% smaller errors when their coefficients are recalibrated. After the recalibration, we identify several models as yielding identical values of DLW_c, which indicate that they are different expression of the same model, and that the increased complexities of the proposed formulas does not result in higher accuracies. Models that correspond to the recalibrated Brunt model include the ones proposed by Refs. [32, 35, 46–51]. Another group of models correspond to recalibrated Carmona model, and includes the ones proposed by Refs. [44, 45]. Since the expression of effective sky emissivity in the Brunt model has only two coefficients and one variable and it achieves high accuracy (rRMSE = 4.37%), the use of recalibrated clear-sky Brunt models is recommended.

Clear night skies has higher effective emissivity than clear days at the same level of surface partial pressure of water vapor, which is observed in this work. The clear nighttime emissivity is larger than the daytime value by 0.035. Therefore, both daytime and nighttime calibrated Brunt-type models are proposed and validated in this study.

Under all sky conditions, the parametric models for calculating DLW should consider the radiation emitted from clouds. The information of clouds is represented by simple cloud cover fractions (CF) or cloud modification factors (CMF, only valid during daytime). Three parametric models proposed in the literature are compared and recalibrated, and a new model is proposed to account for the alternation of vertical atmosphere profiles by clouds. During the daytime, the proposed all-sky model has 15.3% ~ 31.8% lower RMSE than the other three calibrated models. If GHI irradiance measurements are available, using CMF has 7.5% lower RMSE than using CF. During the nighttime and all day periods, the proposed model yields 1.3% ~ 3.8% lower RMSE than the recalibrated Crawford and Duchon model. For different applications that require LW information during daytime and/or nighttime, coefficients of the proposed model can be selected for use.

The main contributions of this chapter are: (1) We propose novel accurate parametric models to calculate 1-minute averaged downward atmospheric longwave irradiance under both clear-sky and all-sky conditions. (2) The coefficients of the proposed models should be considered more universal, since data from seven climatologically diverse stations (rather than one or two particular locations) are used. (3) We also determined that several clear-sky parametric models proposed recently are equivalent.

2.7 Acknowledgment

This chapter, in full, is a reprint of M. Li, Y. Jiang, and C. F. M. Coimbra (2017) “On the Determination of Atmospheric Longwave Irradiance under All-Sky Conditions.” *Solar Energy* (144), 40-48. The dissertation author is the first author of this publication.

Chapter 3

Spectral modeling of longwave radiative transfer in the atmosphere

3.1 Introduction

Surface downwelling longwave irradiance (DLW) plays a critical role on weather and climate variability modeling, as well as on the heat balance design of solar power plants, of radiant cooling systems, and of the built environment [16]. Surface DLW can be measured directly by pyrgeometers, but pyrgeometers are not widely available in weather stations due to capital and calibration expenses. Furthermore, infrared radiation from the surroundings tend to complicate the installation of research-quality pyrgeometers. Because of the importance of surface DLW on the thermal balance of both agricultural and industrial environments, simplified models to estimate the so-called sky radiosity have been proposed (see [16] for an extensive review and up-to-date data-driven models). A simple-to-use parametric model with coefficients regressed from measurements can be used to calculate the ground level longwave irradiance with satisfactory accuracy. However, for locations without pyrgeometers, choosing a parametric model with regression coefficients estimated from the measurements of other locations may introduce bias errors because the surface level downwelling irradiance depends on local meteorological conditions. This work aims to develop a *minimal* model for calculating the atmospheric downwelling longwave radiation within the uncertainty of commonly used pyrgeometers.

A spectrally resolved radiative model is developed to calculate the interactions of longwave irradiance with atmospheric molecules, aerosols and clouds. When compared with other available radiative models [56–59], this model incorporates the most up-to-date HIgh Resoluton TRANsmission (HITRAN) molecule spectral line data combined with the Mlawer-Tobin-Clough-Kneizys-Davies (MT_CKD) water vapor and CO_2 continuum model [60, 61]. The proposed model incorporates Mie theory to calculate aerosol extinction coefficients and asymmetry factors, with modifications for aerosol size distribution and refraction index corrections for aerosol - water vapor interactions. The complete model is a robust and inexpensive tool to study longwave radiative heat transfer in the atmosphere. The robustness of the model is derived from the use of a standard atmosphere that can be readily adjusted for surface altitude. The model was designed to be applied to the Air Force Geophysics Laboratory (AFGL) midlatitude summer atmosphere by simple displacement of the local altitude above sea level (see Section 3.5.3 for details).

In building the complete model, a recognition that most of the complexity related to the mutual interactions between atmosphere layers, aerosols and participating gases cannot be resolved without a detailed spectral consideration of each component. Thus, the model adopts high-resolution line-by-line data for all main constituents.

The monochromatic thermal exchange between layers is calculated by an isotropic *two-stream* (or *two-flux*) model [62–65], where the piecewise monochromatic sections of the spectrum are first treated as perfect emitters before they are recursively corrected by the application of a reflective plating algorithm. This application of the plating algorithm originally proposed by Edwards [66] for radiative enclosures allows for expedited incorporation of piecewise non-black portions of the spectrum, including aerosol scattering. To the best of our knowledge, this type of recursive plating algorithm has not been applied to atmospheric radiation problems before. The combination of reusable transfer factors, high-resolution line-by-line spectral data, and the recursive plating algorithm results in a fast computational method that can be performed in real-time (within realistic time constants of change of temperature and relative humidity) by a mini computer (e.g., Raspberry Pi or BeagleBone), thus allowing for the development of smart instruments for DLW calculations as opposed to relying on sparse pyrgeometer data networks. Because the proposed model incorporates the main thermal radiation contributions in the atmosphere, it can also be used to study the sensitivity of DLW to greenhouse gases (H_2O, CO_2 and CH_4) and aerosols by adjusting the parameters in the model without the need for local telemetry.

The main components of the proposed spectral model are outlined in Table 3.1, and the detailed methodology used for evaluation is presented in Section 3.2 to 3.4, and the model is validated in Section 3.5.

Table 3.1: Main components of the proposed model

Model components	Descriptions	Presented in
Main radiative model	Divides the atmosphere into N parallel layers, constant σ coordinate system for pressures	Section 3.2
Temperature profile	AFGL profiles	Section 3.2
Concentration profiles of atmospheric gases	AFGL profiles corrected to current surface concentrations of gases	Section 3.2
Spectral resolution	Wavenumber range from 0 to 2500 cm^{-1} with resolution of 0.01 cm^{-1}	Section 3.2
Aerosol absorption and scattering coefficients	Evaluated using Mie theory	Section 3.3.1
Aerosol size distribution	Assumes equivalent spherical shape for the aerosols, size distribution follows a bimodal lognormal distribution	Section 3.3.1
Aerosol interaction with water vapor	Aerosol size and refraction index change with respect to water vapor concentration in the surrounding air	Section 3.3.1
Clouds absorption and scattering coefficients	Evaluated using Mie theory	Section 3.3.2
Clouds droplet size distribution	Assumes equivalent spherical shape for the droplets, size distribution follows a Gamma distribution	Section 3.3.2
Spectral line absorption coefficients	HITRAN 2016 absorption coefficients for 7 atmospheric gases: H_2O, CO_2, O_3, CH_4,N_2O, O_2 and N_2 evaluated at layer-averaged pressures and temperatures. Data retrived via HITRAN API	Section 3.3.3
Continuum absorption coefficients	MT_CKD continuum model for H_2O, CO_2, O_3 and O_2	Section 3.3.3
Monochromatic flux of scattering medium	Scale anisotropic scattering to isotropic by δ-M approximation, use exponential integral as transferfactors, blackbody emissive power of each layer is evaluated at layer average temperature	Section 3.4.1
Broadband flux	Integrated monochromatic flux density	Section 3.4.2

3.2 Model structure

This section presents the method used to divide the atmosphere into N parallel layers, with pressure, temperature and constituent profiles along the z direction. As depicted in Fig.3.1, the atmosphere is divided in N layers, extending from the surface to an altitude with approximately zero pressure. The layers are determined according to pressure, not physical height. The monochromatic downwelling and upwelling fluxes q_n^- and q_n^+ are evaluated at layer boundaries. The monochromatic extinction coefficient κ_e, single scattering albedo $\tilde{\rho}$ and asymmetry factor g for each layer are evaluated using layer-averaged pressure $\bar{P}_n$ and temperature $\bar{T}_n$ values.

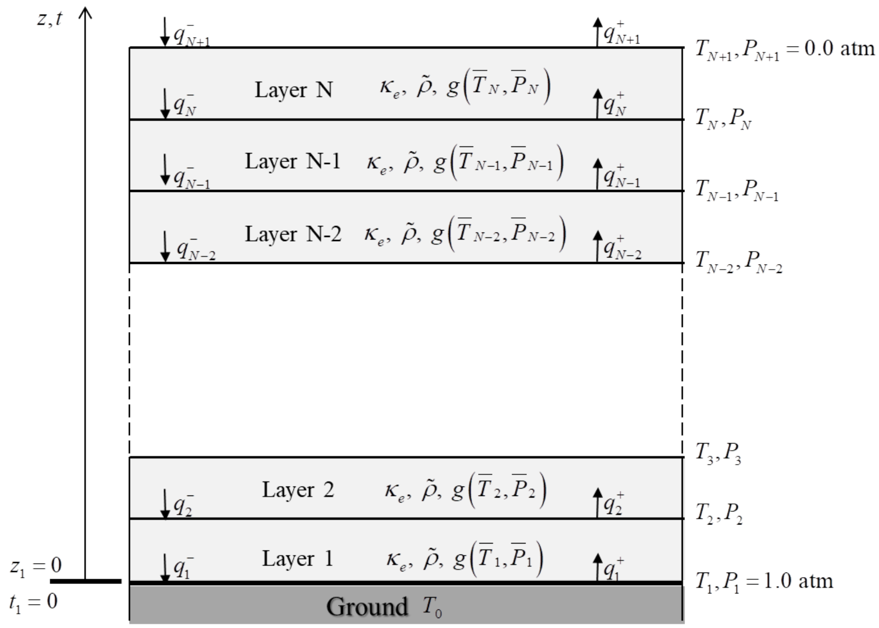

Figure 3.1: Schematic representation of the multilayer model of the Earth-atmosphere system. The vertical coordinates of altitude and normal optical path are labeled as z and t, respectively. The surface altitude z and normal optical depth t are equal to zero.

A constant σ_n coordinate system designates the average pressure $\bar{P}_n$ and the pressure of each layer boundary [67, 68]:

$$
\begin{aligned}
\sigma_n &= \frac{2N - 2n + 1}{2N}, \\
\bar{P}_n &= \sigma_n^2(3 - 2\sigma_n), \\
P_n &= \bar{P}_{n-0.5}
\end{aligned}
\tag{3.1}
$$

and the pressure-averaged temperature of layer n is:

$$
\bar{T}_n = \frac{T_n(P_n - \bar{P}_n) + T_{n+1}(\bar{P}_n - P_{n+1})}{P_n - P_{n+1}}. \tag{3.2}
$$

AFGL profiles [69] are used for the temperature profile T_n and pressure profile P_n (Fig. 3.2). Since the pressure is defined by Eq. (3.1), the z_n and T_n are inferred from P_n according to the AFGL profiles. The AFGL midlatitude summer profile is used throughout this work, unless noted otherwise.

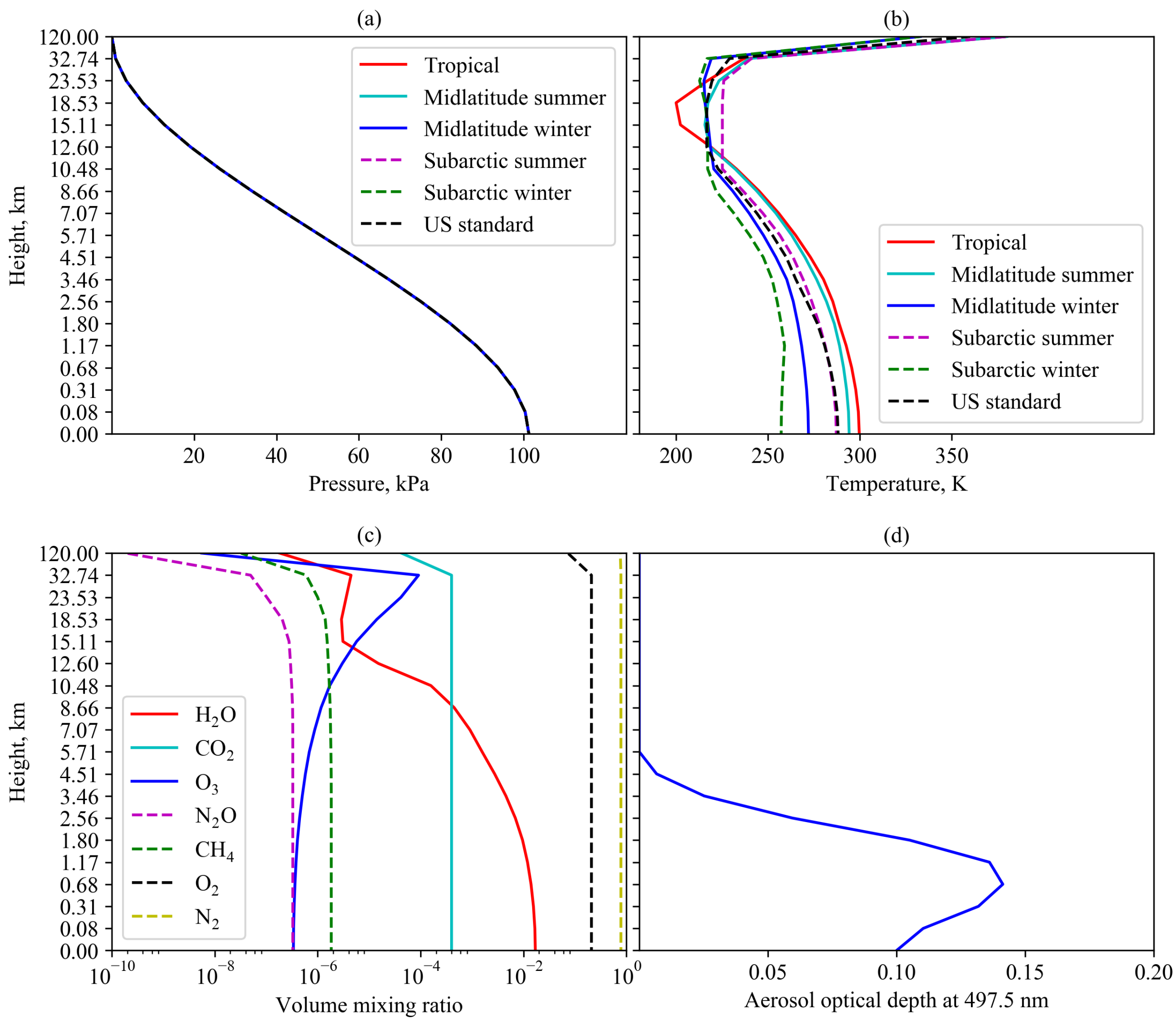

Figure 3.2: (a) AFGL pressure profiles; (b) AFGL temperature profiles; (c) AFGL midlatitude summer gas profiles corrected for current surface concentration of gases (shown for 70% surface relative humidity); (d) aerosol optical depth at 497.5 nm.

Seven participating atmospheric gases are considered: water vapor (H_2O), carbon dioxide (CO_2), ozone (O_3), methane (CH_4), nitrous oxide (N_2O), oxygen (O_2) and nitrogen (N_2). The vertical profiles of those gases are also based on AFGL profiles [69], with modifications to account for various surface conditions

(Fig. 3.2). For each gas, the vertical profile of the volumetric mixing ratio is given by

$$w(z) = w^*(0)\frac{w_{\mathrm{AFGL}}(z)}{w_{\mathrm{AFGL}}(0)}, \tag{3.3}$$

where $w^*(0)$ represents the current surface volumetric mixing ratio. For H_2O, $w^*(0)$ is a function of surface relative humidity ϕ_1, such that

$$w^*_{\mathrm{H_2O}}(0) = \frac{\phi_1 P_s(T_1)}{P_1}. \tag{3.4}$$

The saturated water vapor pressure P_s (Pa) for a given temperature T (K) is calculated using the August-Roche-Magnus (ARM) expression [38]

$$P_s(T) = P_{\mathrm{ARM}}\ \exp\left(\frac{c_{\mathrm{ARM}}(T-273.15)}{T-30.11}\right), \tag{3.5}$$

where $P_{\mathrm{ARM}} = 610.94$ Pa and $c_{\mathrm{ARM}} = 17.625$.

For the other gases we use current averaged values for the volumetric mixing ratios $w^*(0)$ in the troposphere [70]: $w^*_{\mathrm{CO_2}}(0) = 399.5$ ppm, $w^*_{\mathrm{O_3}}(0) = 337$ ppm, $w^*_{\mathrm{CH_4}}(0) = 1834$ ppb, $w^*_{\mathrm{N_2O}}(0) = 328$ ppb, $w^*_{\mathrm{O_2}}(0) = 0.209$ and $w^*_{\mathrm{N_2}}(0) = 0.781$.

The vertical aerosol concentration profile is adopted from [71] using the Cloud Aerosol LIDAR and Infrared Pathfinder Satellite Observations (CALIPSO) over North America. As mentioned before, we cover the wavenumber range from 0 to 2500 cm^{-1} in order to include all bands of practical interest, and adopt a spectral resolution of 0.01 cm^{-1}.

3.3 Monochromatic volumetric optical properties of atmosphere layers

The atmosphere is assumed to contain seven participating gases plus aerosols and clouds. For longwave radiation, scattering by gas molecules can be neglected [72], so only scattering by aerosols and clouds are considered here. The monochromatic volumetric extinction coefficient, the single scattering albedo and asymmetry factor for each layer are expressed as (the subscript for wavenumber ν is omitted in this section for expediency),

$$
\begin{aligned}
\kappa_e &= \kappa_a + \kappa_s = \kappa_{a,\text{gas}} + \kappa_{a,\text{aer}} + \kappa_{s,\text{aer}} + \kappa_{a,\text{cld}} + \kappa_{s,\text{cld}}, \\
\tilde{\rho} &= \frac{\kappa_{s,\text{aer}} + \kappa_{s,\text{cld}}}{\kappa_e}, \\
g &= \frac{\kappa_{s,\text{aer}} g_{\text{aer}} + \kappa_{s,\text{cld}} g_{\text{cld}}}{\kappa_{s,\text{aer}} + \kappa_{s,\text{cld}}}
\end{aligned}
\tag{3.6}
$$

where coefficients of gases, aerosols and clouds are evaluated at layer averaged temperature $\bar{T}_n$ and pressure $\bar{P}_n$. The absorption and scattering coefficients of aerosols and clouds follow Mie theory behavior, as detailed in the following sections 3.3.1 and 3.3.2. The method we use to calculate absorption coefficients for gas mixtures is detailed in 3.3.3.

3.3.1 Absorption and scattering coefficients of aerosols

The monochromatic absorption coefficient $\kappa_{a,\text{aer}}$, scattering coefficient $\kappa_{s,\text{aer}}$ and asymmetry factor g_{aer} of aerosols are functions of aerosol size distribution and aerosol refractive index.

The size distribution of aerosol particles in the model follows a standard lognormal distribution [2],

$$
\frac{dN}{d\ln r} = r\frac{dN}{dr} = rn(r) = \sum_{i=1}^{I} \frac{N_i}{\sqrt{2\pi}\ln\sigma_i} \exp\left[-\frac{1}{2}\left(\frac{\ln(r/r_{m,i})}{\ln\sigma_i}\right)^2\right]. \tag{3.7}
$$

For each mode i, $r_{m,i}$ (μm) is the mode radii, σ_i (μm) is the standard deviation and N_i is the mode amplitude. For internally mixed aerosols (aerosols mixed as a homogeneous material that reflects the chemical and physical average of all the contributing components [73]), the size distribution can be expressed bimodally with $I = 2$ and $r_{m,1} = 0.135$ μm, $r_{m,2} = 0.995$ μm, $\sigma_1 = 2.477$ μm, $\sigma_2 = 2.051$ μm [2]. The smaller particle mode is dominant given that $N_1 = 10^4 N_2$. Since the composition and size distribution of atmospheric aerosols vary greatly with time and locations [74], aerosols modeled in [2] are used to demonstrate the proposed model. Different aerosol compositions and size distributions can be easily implemented in the model.

To account for the changes of aerosol size distribution and refractive index due to the interaction with water vapor, a growth factor g_f is used. The value of g_f is a function of surrounding relative humidity as tabulated in Table 3.2 [2]. The value of g_f is multiplied by the mode radii $r_{m,i}$ in Eq. (3.7) to account for size changes, and is used in the following relation to account for the change of refractive index m [2]:

$$
m = m_0 g_f^{-3} + m_w(1 - g_f^{-3}), \tag{3.8}
$$

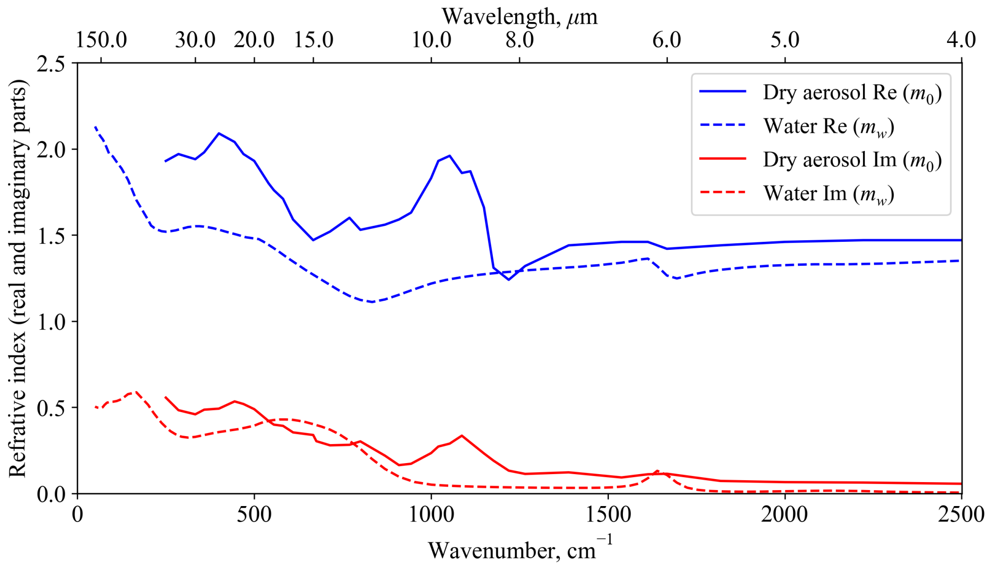

Figure 3.3: Refractive index of aerosols and liquid water [2, 3]. Re(·) and Im(·) stand for the real and imaginary parts of the index.

where the subscript 0 stands for dry aerosols, and the subscript w stands for liquid water. The spectral refractive index of dry aerosols m_0 and liquid water m_w are plotted in Fig. 3.3. Data for these plots were obtained from Ref. [2] and [3], respectively.

Table 3.2: Growth factor of aerosols [2]. Starred values are interpolated in the proposed model.

RH,%	0	10	20	30	40	50	60	70	80	90	100
g_f	1.000*	1.000*	1.000*	1.031	1.055	1.09	1.15	1.26	1.554	1.851	2.151*

The scattering of longwave radiation by aerosols is modeled by Mie theory, assuming equivalent spherical shapes for the aerosols [72]. The extinction, scattering, absorption efficiencies and asymmetry parameter of a single aerosol particle are calculated using standard Mie theory relations [72, 75],

$$
\begin{aligned}
Q_e &= \frac{2}{x^2}\sum_{n=1}^{\infty}(2n+1)\mathrm{Re}(a_n+b_n),\\
Q_s &= \frac{2}{x^2}\sum_{n=1}^{\infty}(2n+1)\left(|a_n|^2+|b_n|^2\right),\\
Q_a &= Q_e - Q_s,\\
g &= \frac{4}{x^2 Q_s}\left[\sum_{n=1}^{\infty}\frac{n(n+2)}{n+1}\mathrm{Re}(a_n a_{n+1}^* + b_n b_{n+1}^*) + \sum_{n=1}^{\infty}\frac{2n+1}{n(n+1)}\mathrm{Re}(a_n b_n^*)\right],
\end{aligned}
\tag{3.9}
$$

where the diacritic * stands for the complex conjugate; Re(·) stands for the real part of a complex number; x is the size parameter, $x = 2\pi\nu r$, where r (cm) is the radius of the aerosol and ν (cm^{-1}) is the wavenumber; a_n and b_n are the Mie coefficients, which are a function of the size parameter x and the aerosol refractive index m.

Note that the above parameters are summations of infinite series, which are truncated after n_{max} terms in the computations to satisfy accuracy requirements. The criteria for the number of terms used is given by [75],

$$n_{\max} = \mathrm{round}(x + 4x^{1/3} + 2). \tag{3.10}$$

When the magnetic permeability of the sphere is equal to the magnetic permeability of the ambient medium, the Mie coefficients a_n and b_n are given by [75],

$$\begin{aligned} a_n &= \frac{m^2 j_n(mx)[x j_n(x)]' - j_n(x)[mx j_n(mx)]'}{m^2 j_n(mx)[x h_n(x)]' - h_n(x)[mx j_n(mx)]'}, \\ b_n &= \frac{j_n(mx)[x j_n(x)]' - j_n(x)[mx j_n(mx)]'}{j_n(mx)[x h_n(x)]' - h_n(x)[mx j_n(mx)]'}, \end{aligned} \tag{3.11}$$

where m is the refractive index of the aerosol relative to the ambient air; $j_n(z)$ is the spherical Bessel function of the first kind; $h_n(z)$ is the spherical Bessel related function, $h_n(z) = j_n(z) + y_n(z)i$ and $y_n(z)$ is the spherical Bessel function of the second kind.

The primes indicate derivatives with respect to the arguments, $z = x$ or $z = mx$, with the derivatives of the spherical Bessel functions being [76],

$$\begin{aligned} [z j_n(z)]' &= z j_{n-1}(z) - n j_n(z), \\ [z h_n(z)]' &= z h_{n-1}(z) - n h_n(z). \end{aligned} \tag{3.12}$$

For atmospheric aerosols with varying sizes, the volumetric absorption and scattering coefficients and asymmetry parameters correspond to integrated values of scattering/absorption efficiencies over all possible aerosol radii r [72],

$$\begin{aligned} \kappa_{a,\mathrm{aer}} &= \int_0^\infty n(r) Q_a(r) \pi r^2 dr, \\ \kappa_{s,\mathrm{aer}} &= \int_0^\infty n(r) Q_s(r) \pi r^2 dr, \\ g_{\mathrm{aer}} &= \frac{1}{\kappa_{s,aer}} \int_0^\infty n(r) Q_s(r) \pi r^2 g(r) dr. \end{aligned} \tag{3.13}$$

The scattering and absorption coefficients of atmospheric aerosols are proportional to N_1, the first mode amplitude, as shown in Eqs. (3.7) and (3.13). Aerosol content in the atmosphere relates to aerosol optical depth (AOD) [1], which is defined as AOD = $\kappa_{e,\text{aer}}\bar{L}$ [77], where $\bar{L}$ is the scale height. Here we take the value of $\bar{L}$ to be 1,575 m, the annualized average value reported in [71] for the continental USA. If $\text{AOD}_{497.5}$ = 0.1, aerosol extinction coefficient at 497.5 nm is then $\kappa_{e,\text{aer@497.5}} = \text{AOD}_{497.5}/\bar{L} = 6.35 \times 10^{-7}$ cm^{-1}. The value of N_1 in Eq. (3.7) is thus determined from $\kappa_{e,\text{aer@497.5}} = 6.35 \times 10^{-7}$ cm^{-1}. Figure 3.4 is a plot of the monochromatic extinction coefficient and optical depth of aerosols when $\text{AOD}_{497.5}$ = 0.1 and relative humidity of 70%.

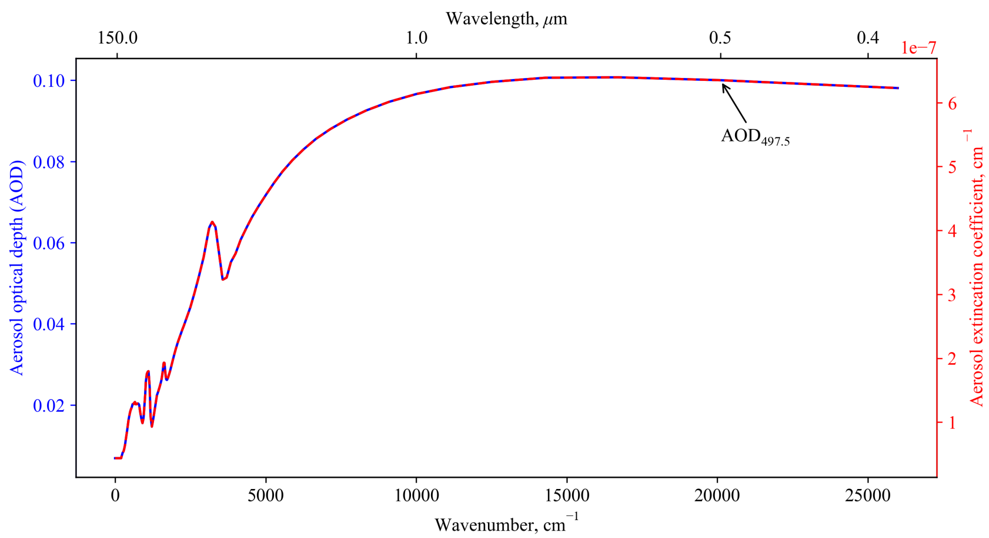

Figure 3.4: The monochromatic extinction coefficient and optical depth of aerosols when $\text{AOD}_{497.5}$ = 0.1 and 70% RH.

3.3.2 Absorption and scattering coefficients of clouds

Water clouds are modeled in the spectral radiative model using the similar methods as aerosols. Each water droplet is assumed to have a spherical shape, thus the absorption and scattering efficiencies of droplets are calculated using Mie theory [5] with the input of the refraction index of water retrieved from [3]. The absorption and scattering coefficients as well as the asymmetry factors of clouds are further calculated by integrating the efficiencies over a droplet size distribution [75]. The size distribution of droplets in clouds is

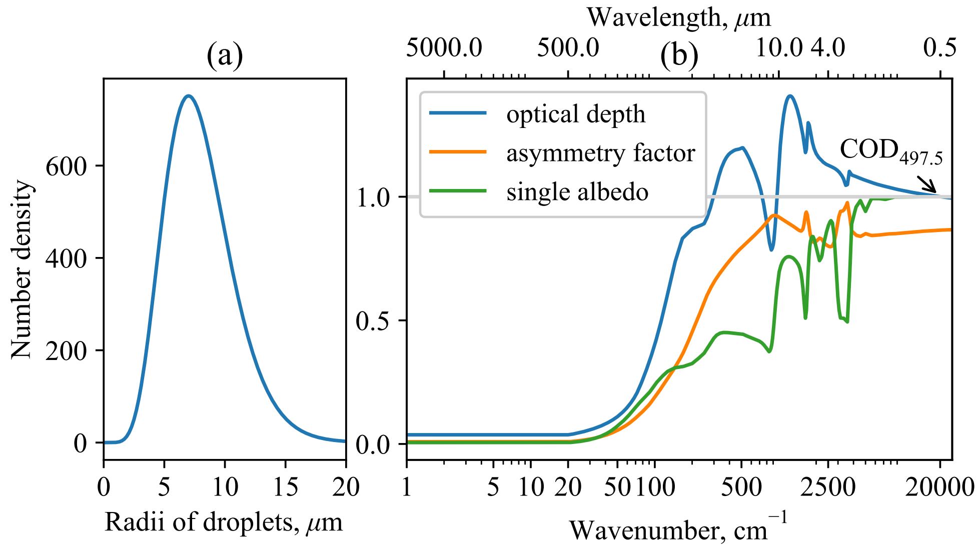

Figure 3.5: (a) Size distribution of droplets in the model clouds. (b) The spectral optical depth, single albedo and asymmetry factor of model clouds for unity value of COD. The subscript 497.5 is omitted in the text for simplicity.

assumed to follow the Gamma distribution [78–80],

$$n(r) = r^{1/\sigma_e - 3} \exp\left(-\frac{r}{r_e \sigma_e}\right), \tag{3.14}$$

where r_e and σ_e are the effective radius and variance, respectively. For modelling purpose, $r_e = 10$ μm and $\sigma_e = 0.1$, as suggested in [80]. The spectral dispersion k used by some modelers to represent the spread of droplet size (instead of σ_e) is defined as $k = (1/\sigma_e - 2)^{-1/2}$. When $\sigma_e = 0.1$, $k = 0.354$, which is a typical value for marine and continental clouds [79]. The size distribution of water droplets is shown in Fig. 3.5 (a).

In the model, clouds are treated as overcast and placed into layers with a predefined optical depth at 497.5 nm defined as COD $= \kappa_{e,\text{cld}} \Delta H_c$ where ΔH_c is the height of the clouds. The spectral optical depth, single albedo and asymmetry factor of clouds are shown in Fig. 3.5 (b) for COD $= 1.0$.

3.3.3 Absorption coefficients of a mixture of atmospheric gases

The volumetric absorption coefficient κ_a (cm^{-1}) of a gas mixture is [72, 81],

$$\kappa_{a,\text{gas}} = \sum_i \rho_i \kappa_i^* = \sum_i \rho_i \left[\kappa_{\text{cont,i}}^* + \kappa_{\text{line,i}}^*\right], \tag{3.15}$$

where ρ_i (g cm^{-3}) is the partial density of gas i which is integrated over a layer; κ_i^* (cm^2 g^{-1}) is the mass absorption coefficient of gas i, which is the summation of continuum absorption coefficient $\kappa^*_{\text{cont,i}}$ and spectral line absorption coefficient $\kappa^*_{\text{line,i}}$.

The spectral line absorption coefficients $\kappa^*_{\text{line,i}}$ are obtained from HITRAN database using the HITRAN API [60, 82]. We use a Lorentz profile with line wing cut-off set to 25 cm^{-1} as suggested by [13, 61, 83] to properly account for the continuum absorption for water vapor. Although the Lorentz line shape is not strictly valid for high altitudes, the contributions from higher altitudes to the surface DLW is small enough that the error in assuming Lorentz line shapes across the atmosphere is negligible (see next Chapter for more details).

The continuum absorption coefficient of water vapor is the summation of self continuum and foreign continuum coefficients,

$$\kappa^*_{\text{cont},H_2O} = \kappa^*_{\text{self},H_2O} + \kappa^*_{\text{frgn},H_2O}. \tag{3.16}$$

The continuum absorption spectral density functions C^0 at reference conditions are obtained from the MT_CKD model [61] and plotted in Fig.3.1 (a). For conditions with temperature T and pressure P, the spectral density function is,

$$C(T,P) = C_{\text{self}}(T,P) + C_{\text{frgn}}(T,P) = \frac{P}{P_0}\frac{T_0}{T}\left[w_{H_2O} C^0_{T_0,\text{self}} \left(\frac{C^0_{T_{\text{ref}},\text{self}}}{C^0_{T_0,\text{self}}}\right)^{\frac{T-T_0}{T_{\text{ref}}-T_0}} + (1-w_{H_2O}) C^0_{T_0,\text{frgn}}\right], \tag{3.17}$$

where T_0 = 296 K, P_0 = 1 atm, T_{ref} = 260 K; w_{H_2O} is the molar fraction of water vapor; $C^0_{T_0,\text{self}}$,$C^0_{T_{\text{ref}},\text{self}}$ and $C^0_{T_0,\text{frgn}}$ are the reference spectral density function in Fig.3.1 (a).

To get the mass absorption coefficients, a 'radiation field' R_f is applied [59, 61],

$$R_f = \begin{cases} 0.5\nu\eta, & \text{for } \eta \le 0.01 \\ \nu\frac{1-\exp(-\eta)}{1+\exp(-\eta)}, & \text{for } \eta \le 10 \\ \nu, & \text{all other conditions} \end{cases} \tag{3.18}$$

where η is a non-dimensional parameter defined as $\eta = \nu/(T/c_{r2})$ with c_{r2} = 1.439 cm K being the second radiation constant [61].

The continuum mass absorption coefficient for water vapor is then,

$$k^*_{\text{cont,H}_2\text{O}} = C(T,P)\, R_f. \tag{3.19}$$

Figure 3.1 (b) plots the spectral and continuum absorption coefficients of pure water vapor, showing that continuum absorption dominates in the atmosphere window from 8 μm to 14 μm.

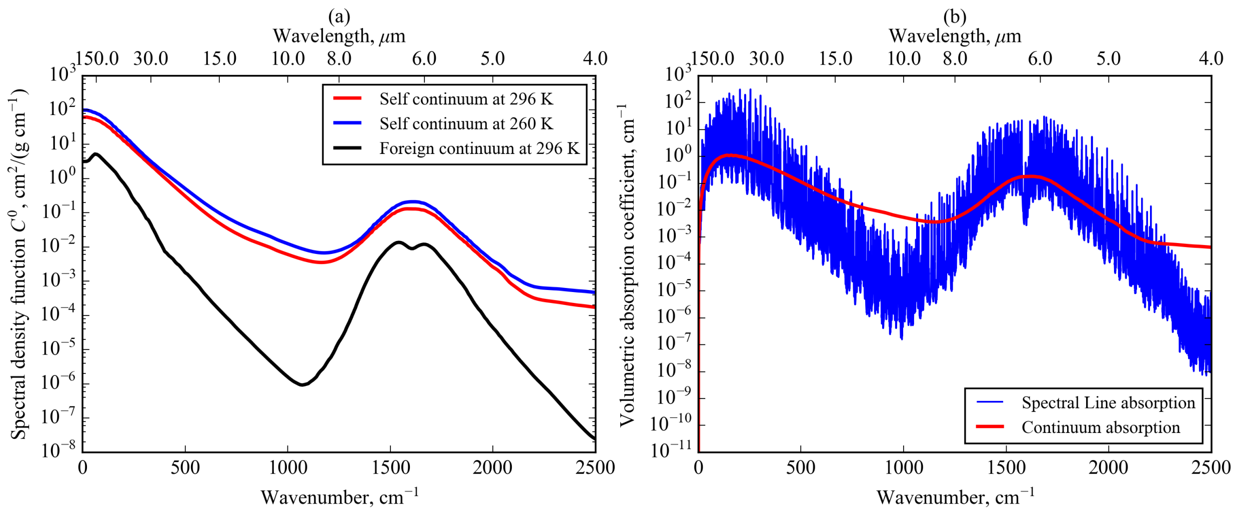

Figure 3.1: (a) The continuum absorption spectral density function C^0 for water vapor at selected conditions. (b) Spectral line and continuum absorption coefficients for water vapor at 1 atm and 288 K.

The continuum absorption spectral density functions C^0 at reference condition for CO_2 are obtained from the MT_CKD model [61] and plotted in Fig.3.2 (a). For conditions with temperature T and pressure P, the spectral density function is,

$$C(T,P) = w_{\text{CO}_2} C^0_{T_{\text{ref2}}} f_c \frac{P}{P_0} \frac{T_0}{T} \left(\frac{T}{T_{\text{ref2}}} \right)^{f_t}, \tag{3.20}$$

where $T_{\text{ref2}} = 246$ K; w_{CO_2} is the molar fraction of CO_2; $C^0_{T_{\text{ref2}}}$ is the reference spectral density function in Fig.3.2 (a); f_c and f_t are the spectral and temperature correction factor obtained from [61], respectively. The continuum mass absorption coefficient for CO_2 is then,

$$k^*_{\text{cont,CO}_2} = C(T,P)\, R_f. \tag{3.21}$$

Figure.3.2 (b) plots the spectral and continuum absorption coefficients of pure CO_2, showing that continuum absorption dominates in the spectral from 6 μm to 8 μm.

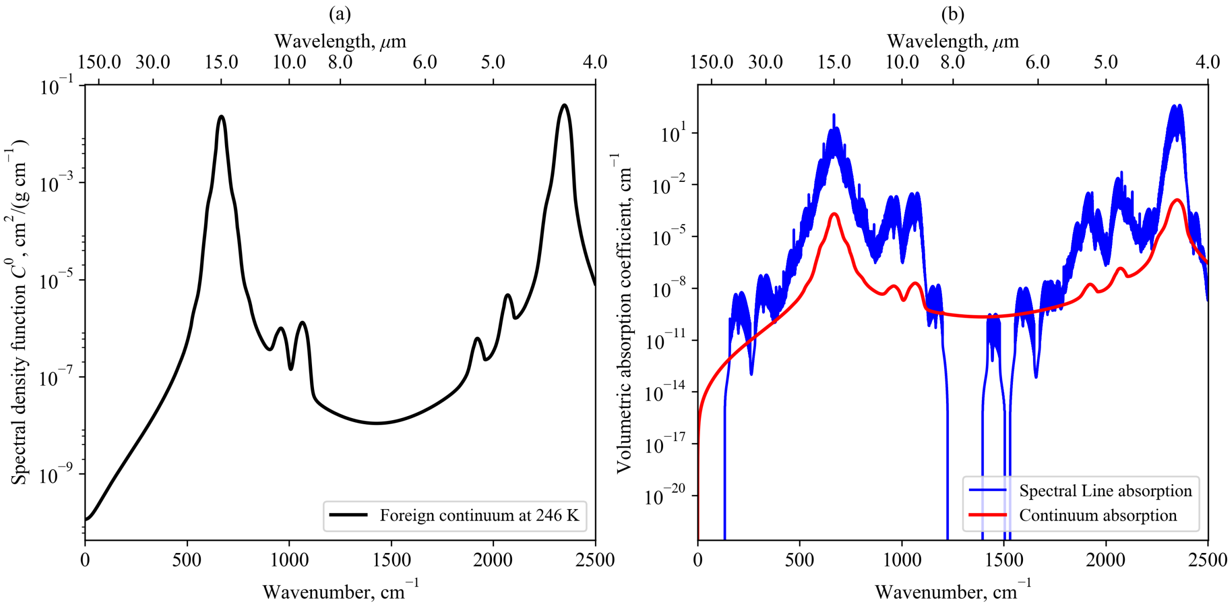

Figure 3.2: (a) The continuum absorption spectral density function C^0 for CO_2 at selected condition. (b) Spectral line and continuum absorption coefficients for CO_2 at 1 atm and 288 K.

3.4 Radiative upwelling and downwelling fluxes

This section presents the complete method used to calculate monochromatic downwelling and upwelling fluxes at each layer boundary in a scattering atmosphere. The broadband longwave fluxes is the integration of monochromatic fluxes over the range of wavenumbers considered (0 – 2500 cm^{-1}).

3.4.1 Monochromatic fluxes

This subsection details the method used to calculate downwelling and upwelling fluxes in a scattering medium from the irradiance G_i and radiosity J_i of each atmospheric layer.

For Earth's atmosphere, the albedo for single scattering is large in some spectral regions under cloud-free skies as shown in Fig. 3.3, thus scattering cannot be completely neglected even though the aerosol scattering effects for longwave radiation are never dominant. For longwave radiation, the asymmetry parameter ranges from 0.02 to 0.75 as shown in Fig. 3.3, therefore the δ-M approximation is used to scale

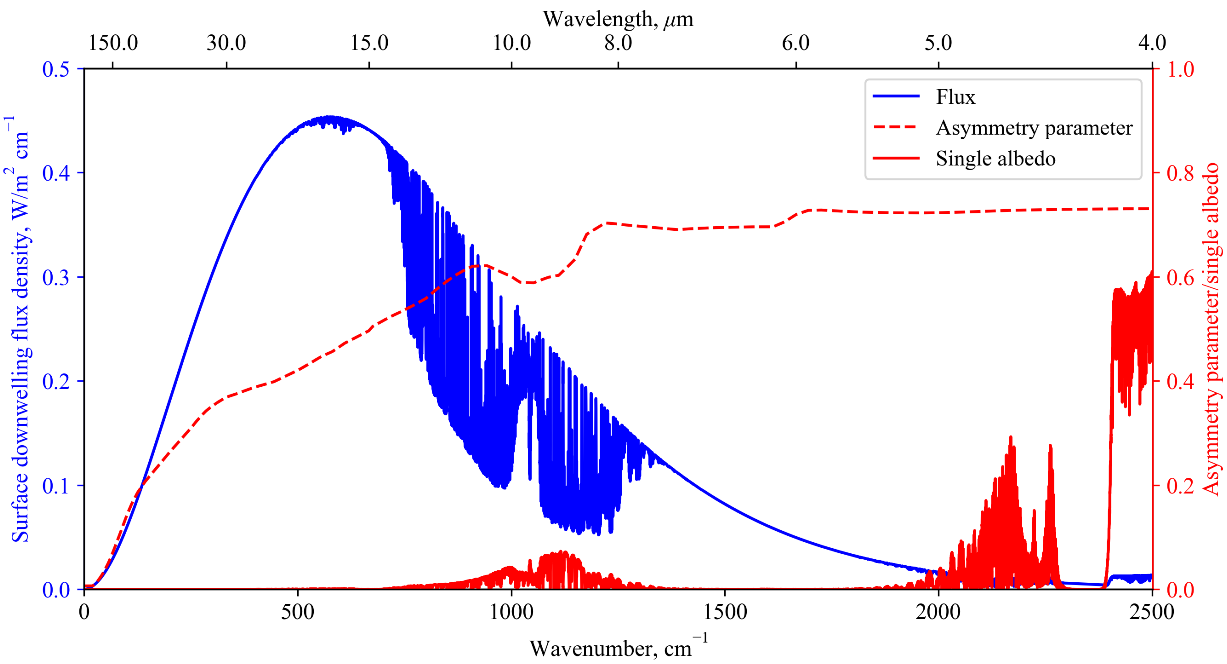

Figure 3.3: The spectral surface downwelling flux density, single scattering albedo and asymmetry parameter of the nearest atmosphere layer, for surface RH = 70% and $AOD_{497.5}$ = 0.1.

anisotropic scattering to isotropic before applying the following algorithm for flux calculation. The δ-M approximation scales the extinction coefficient and the single albedo using [84],

$$\begin{aligned} \hat{\kappa_e} &= (1-\tilde{\rho}g)\kappa_e, \\ \hat{\tilde{\rho}} &= \frac{\tilde{\rho}(1-g)}{1-\tilde{\rho}g}. \end{aligned} \tag{3.22}$$

After the scaling, isotropic scattering is assumed in the proposed model to reduce computational complexity.

For each layer n with a single albedo $\hat{\tilde{\rho}}_n$ and extinction coefficient $\hat{\kappa}_{e,n}$, the irradiance G_n and radiosity J_n are,

$$\begin{aligned} G_n &= \sum_{j=0}^{N+1} \mathcal{F}_{n,j} J_j, \\ J_n &= (1-\hat{\tilde{\rho}}_n)\pi \bar{I}_{b,n} + \hat{\tilde{\rho}}_n G_n, \end{aligned} \tag{3.23}$$

where $\mathcal{F}_{n,j}$ is the transfer factor between layer n and layer j, and $\pi\bar{I}_{b,n}$ is the averaged blackbody emissive flux of the layer, which is taken to be $\pi I_b(\bar{T}_n)$. The symbol I_b (W m m^{-2} sr^{-1}) is used for the monochromatic intensity in wavenumber basis defined by Eq.(1.2). Note that j values range from 0 to $N+1$ where layer 0 represents the ground layer and optical depth t_0 is taken to be negative infinity ($-\infty$). Layer $N+1$ represents the outer space layer and optical depth t_{N+2} is taken to be positive infinity ($+\infty$).

The transfer factors $\mathcal{F}_{n,j}$ are derived as follows. The monochromatic attenuation of intensity along a path s for an isotropic scattering medium is (wavenumber ν is omitted),

$$\frac{dI}{ds} = \hat{\kappa_e}(1-\hat{\hat{\rho}})I_b + \hat{\kappa_e}\hat{\hat{\rho}}\bar{I} - \hat{\kappa_e}I, \tag{3.24}$$

where $\hat{\kappa_e}$ (cm^{-1}) is the extinction coefficient (δ-M scaled), $\hat{\hat{\rho}}$ is the single scattering albedo (δ-M scaled), $\bar{I}$ is the averaged intensity over all solid angles, $\bar{I} = 1/4\pi \iint_0^{4\pi} I d^2\omega$.

The radiosity J and irradiance G of a volume are,

$$J = (1-\hat{\hat{\rho}})\pi I_b + \hat{\hat{\rho}}\pi\bar{I}; \qquad G = \int_0^s e^{-t_{s'}} J(s')ds', \tag{3.25}$$

where the optical depth $t_{s'} = \int_0^{s'} \hat{\kappa_e}(s'')ds''$.

For a plane parallel layer of atmosphere as shown in Fig. 3.4, the irradiance is expressed using *transfer factors*,

$$G_n = \sum_j J_j \mathcal{F}_{n,j} = \sum_j J_j \frac{1}{4\pi} \iint_0^{4\pi} \left[e^{t_s - t_{s,j}} - e^{t_s - t_{s,j+1}}\right] d^2\omega, \tag{3.26}$$

where the transfer factor between layer n and layer j is defined as

$$\mathcal{F}_{n,j} = \frac{1}{\Delta t_{s,n}} \int_{t_s} \int_0^{2\pi} d\phi \int_\theta \left[e^{t_s - t_{s,j}} - e^{t_s - t_{s,j+1}}\right] \frac{\sin\theta d\theta}{4\pi} dt_s. \tag{3.27}$$

Let $u = 1/\cos\theta$, then $du = \sin\theta/\cos^2\theta d\theta$ and $\sin\theta d\theta = du/u^2$. Note that the transfer factors given above can be written in terms of the normal optical depth $t = \int_0^z \hat{\kappa_e}(z')dz'$,

$$\begin{aligned}\mathcal{F}_{n,j} &= \frac{1}{2\Delta t_n} \int_t \int_1^\infty \left[e^{(t-t_j)u} - e^{(t-t_{s,j+1})u}\right] \frac{du}{u^2} = \frac{1}{2\Delta t_n} \int_{t_n}^{t_{n+1}} [E_2(t_j - t) - E_2(t_{j+1} - t)]dt \\ &= \frac{1}{2\Delta t_n} [E_3(|t_j - t_{n+1}|) + E_3(|t_{j+1} - t_n|) - E_3(|t_j - t_n|) - E_3(|t_{j+1} - t_{n+1}|)],\end{aligned} \tag{3.28}$$

where $E_2(\cdot)$ and $E_3(\cdot)$ correspond to the second and third exponential integral functions defined by $E_n(t) = \int_1^{+\infty} \exp(-ut)/u^n du$, which accounts for the integration of intensities over all solid angles of a hemisphere.

The transfer factor $\mathcal{F}_{n,n}$ for a layer to itself (due to emission and scattering) is,

$$\mathcal{F}_{n,n} = 1 - \frac{1}{2\Delta t_n}\int_{t_n}^{t_{n+1}}[E_2(t_n - t) - E_2(t_{n+1} - t)]dt = 1 - \frac{1 - 2E_3(|t_{n+1} - t_n|)}{2(t_{n+1} - t_n)}. \qquad (3.29)$$

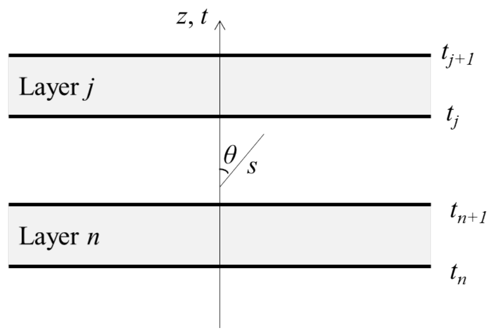

Figure 3.4: Plane parallel geometry and layer indices.

In sum, the transfer factors are,

$$\begin{aligned} A_n^*\mathcal{F}_{n,j} &= 2E_3(|t_j - t_{n+1}|) + 2E_3(|t_{j+1} - t_n|) - 2E_3(|t_j - t_n|) - 2E_3(|t_{j+1} - t_{n+1}|) \quad \text{for } j \neq n, \\ \mathcal{F}_{n,n} &= 1 - \frac{1 - 2E_3(t_{n+1} - t_n)}{2(t_{n+1} - t_n)} \quad \text{for } j = n, \end{aligned} \qquad (3.30)$$

where A_n^* is the equivalent surface area. For gas layers, $A_n^* = 4\hat{\kappa}_{e,n}\Delta z_n$ and for outer space and ground surface, $A_n^* = 1$.

The G_n and J_n are assembled in a matrix and solved by matrix reduction,

$$
\begin{pmatrix} G_0 \\ G_1 \\ \vdots \\ G_N \\ G_{N+1} \\ J_0 \\ J_1 \\ \vdots \\ J_N \\ J_{N+1} \end{pmatrix}
=
\begin{pmatrix}
0 & 0 & \cdots & 0 & 0 & \mathcal{F}_{0,0} & \mathcal{F}_{0,1} & \cdots & \mathcal{F}_{0,N} & \mathcal{F}_{0,N+1} \\
0 & 0 & \cdots & 0 & 0 & \mathcal{F}_{1,0} & \mathcal{F}_{1,1} & \cdots & \mathcal{F}_{1,N} & \mathcal{F}_{1,N+1} \\
\vdots & \vdots & \vdots & \vdots & \vdots & \vdots & \vdots & \vdots & \vdots & \vdots \\
0 & 0 & \cdots & 0 & 0 & \mathcal{F}_{N,0} & \mathcal{F}_{N,1} & \cdots & \mathcal{F}_{N,N} & \mathcal{F}_{N,N+1} \\
0 & 0 & \cdots & 0 & 0 & \mathcal{F}_{N+1,0} & \mathcal{F}_{N+1,1} & \cdots & \mathcal{F}_{N+1,N} & \mathcal{F}_{N+1,N+1} \\
\hat{\rho}_0 & 0 & \cdots & 0 & 0 & 0 & 0 & \cdots & 0 & 0 \\
0 & \hat{\rho}_1 & \cdots & 0 & 0 & 0 & 0 & \cdots & 0 & 0 \\
\vdots & \vdots & \ddots & \vdots & \vdots & \vdots & \vdots & \vdots & \vdots & \vdots \\
0 & 0 & \cdots & \hat{\rho}_N & 0 & 0 & 0 & \cdots & 0 & 0 \\
0 & 0 & \cdots & 0 & \hat{\rho}_{N+1} & 0 & 0 & \cdots & 0 & 0
\end{pmatrix}
\begin{pmatrix} G_0 \\ G_1 \\ \vdots \\ G_N \\ G_{N+1} \\ J_0 \\ J_1 \\ \vdots \\ J_N \\ J_{N+1} \end{pmatrix}
+
\begin{pmatrix} 0 \\ 0 \\ \vdots \\ 0 \\ 0 \\ (1-\hat{\rho}_0)\pi\bar{\boldsymbol{I}}_{b,0} \\ (1-\hat{\rho}_1)\pi\bar{\boldsymbol{I}}_{b,1} \\ \vdots \\ (1-\hat{\rho}_N)\pi\bar{\boldsymbol{I}}_{b,N} \\ (1-\hat{\rho}_{N+1})\pi\bar{\boldsymbol{I}}_{b,N+1} \end{pmatrix}
$$

With the values of J_j determined, the downward and upward fluxes are calculated as,

$$
\begin{aligned}
q_n^- &= \sum_{j=n}^{N+1} \mathcal{F}^*_{n,j} J_j, \\
q_n^+ &= \sum_{j=0}^{n-1} \mathcal{F}^*_{n,j} J_j,
\end{aligned}
\tag{3.31}
$$

where $\mathcal{F}^{*}_{n,j}$ represent corrected transfer factors for downward and upward fluxes calculation. The values of $\mathcal{F}^{*}_{n,j}$ are calculated using Eq. (3.30) with the following rules for optical depth re-determination: (1) when calculating downward fluxes q^{-}_{n}, t_0 to t_{n-1} are taken to be $-\infty$; (2) when calculating upward fluxes q^{+}_{n}, t_{n+1} to t_{N+2} are taken to be $+\infty$.

Note that the above matrix reductions are calculated on every wavenumber, i.e. 0.25 million times with the resolution of 0.01 cm^{-1} for spectral range from 0 cm^{-1} to 2500 cm^{-1}. To make the model more computationally efficient, the irradiance G_n is solved directly by defining a modified transfer factor $\mathcal{F}^{**}_{n,j}$,

$$G_n = \sum_{j=0}^{N+1} \mathcal{F}^{**}_{n,j} \pi \bar{I}_{b,j}, \tag{3.32}$$

where the modified transfer factor $\mathcal{F}^{**}_{n,j}$ is calculated from the blackbody transfer factors $\mathcal{F}_{n,j}$ (Eq.(3.30)) recursively using a modified plating algorithm first proposed by Edwards [66] for radiative transfer within enclosures, but here adapted to radiative exchange between atmospheric layers with scattering.

The plating algorithm for scattering is initiated by assuming all layers to be non-scattering, i.e., having albedo $\hat{\hat{\rho}} = 0$,

$$G_n = \sum_{j=0}^{N+1} \mathcal{F}_{n,j} \pi \bar{I}_{b,j}. \tag{3.33}$$

Then the algorithm applies a single scattering albedo $\hat{\hat{\rho}}$ value to one layer at a time recursively, starting from layer 0. Non-scattering layers are skipped. Upon the plating of layer k, the radiosity is converted from $\pi \bar{I}_{b,k}$ to J_k, the sum of the emitted and scattered radiation,

$$J_k = (1 - \hat{\hat{\rho}}_n) \pi \bar{I}_{b,k} + \hat{\hat{\rho}}_n G^{*}_{k}, \qquad \text{and} \qquad G^{*}_{k} = \sum_{j \neq k} \mathcal{F}_{k,j} \pi \bar{I}_{b,j} + \mathcal{F}_{k,k} J_k, \tag{3.34}$$

where * denotes the corrected irradiance value after plating. Combining the relations in (3.34) gives the radiosity,

$$J_k = \frac{1 - \hat{\hat{\rho}}_k}{D_k} \pi \bar{I}_{b,k} + \frac{\hat{\hat{\rho}}_k}{D_k} \sum_{j \neq k} \mathcal{F}_{k,j} \pi \bar{I}_{b,j}, \tag{3.35}$$

where the denominator is $D_k = 1 - \hat{\hat{\rho}}_k \mathcal{F}_{k,k}$. When i is different from k, the new value of irradiance after plating layer k is given by,

$$G_i^* = \sum_{j\neq k} \mathcal{F}_{i,j}\pi\bar{I}_{b,j} + \mathcal{F}_{i,k}J_k = \sum_{j\neq k}\left[\mathcal{F}_{i,j} + \frac{\hat{\tilde{\rho}}_k}{D_k}\mathcal{F}_{i,k}\mathcal{F}_{k,j}\right]\pi\bar{I}_{b,j} + \frac{1-\hat{\tilde{\rho}}_k}{D_k}\mathcal{F}_{i,k}\pi\bar{I}_{b,k}. \tag{3.36}$$

The irradiance of layer k itself is then affected by the single scattering albedo,

$$G_k^* = (1-\hat{\tilde{\rho}}_k)\sum_{j\neq k}\mathcal{F}_{k,j}\pi\bar{I}_{b,j} + (1-\tilde{\rho}_{s,k})\mathcal{F}_{k,k}J_k = (1-\hat{\tilde{\rho}}_k)\sum_{j\neq k}\left[\mathcal{F}_{k,j} + \frac{\hat{\tilde{\rho}}_k}{D_k}\mathcal{F}_{k,k}\mathcal{F}_{k,j}\right]\pi\bar{I}_{b,j} + \frac{(1-\hat{\tilde{\rho}}_k)^2}{D_k}\mathcal{F}_{k,k}\pi\bar{I}_{b,k}. \tag{3.37}$$

Compare Eqs.(3.36) and (3.37) with Eq. (3.32) shows that four cases exist,

$$\begin{cases} \mathcal{F}_{i,j}^{**} = \mathcal{F}_{i,j} + \frac{\hat{\tilde{\rho}}_k}{D_k}\mathcal{F}_{i,k}\mathcal{F}_{k,j}, & i\neq k, j\neq k, \\ \mathcal{F}_{i,k}^{**} = \frac{1-\hat{\tilde{\rho}}_k}{D}\mathcal{F}_{i,k}, & i\neq k, j=k, \\ \mathcal{F}_{k,j}^{**} = (1-\hat{\tilde{\rho}}_k)\left[\mathcal{F}_{k,j} + \frac{\hat{\tilde{\rho}}_k}{D_k}\mathcal{F}_{k,k}\mathcal{F}_{k,j}\right] = \frac{1-\hat{\tilde{\rho}}_k}{D_k}\mathcal{F}_{k,j}, & i=k, j\neq k, \\ \mathcal{F}_{k,k}^{**} = \frac{(1-\hat{\tilde{\rho}}_k)^2}{D}\mathcal{F}_{k,k}, & i=k, j=k. \end{cases} \tag{3.38}$$

After plating, the modified transfer factors satisfy $\sum_{j=0}^{N+1}\mathcal{F}_{k,j}^{**} = 1-\hat{\tilde{\rho}}_k$.

The wavenumbers are vectorized when calculating the modified transfer factors, so the computational performance is improved in comparison to matrix reductions. More details about the computational performance of the overall algorithm are given in Section 4.1.

3.4.2 Broadband fluxes

The broadband flux is the integration of monochromatic flux over the considered longwave wavenumber range,

$$\begin{aligned} \mathbf{q}_n^- &= \int_{\nu_1}^{\nu_2} q_n^-(\nu)d\nu, \\ \mathbf{q}_n^+ &= \int_{\nu_1}^{\nu_2} q_n^+(\nu)d\nu, \end{aligned} \tag{3.39}$$

where $q_n^-(\nu)$ / $q_n^+(\nu)$ is monochromatic downward / upward flux and ν (cm^{-1}) is wavenumber in the range of $\nu_1 = 0\ \mathrm{cm}^{-1}$ and $\nu_2 = 2500\ \mathrm{cm}^{-1}$. Broadband integration is evaluated using a trapezoidal rule.

3.5 Validation of the model

3.5.1 Grid convergence

The plane parallel model of the atmosphere assumes each layer to be homogeneous, so the accuracy of the model may be compromised if too few layers are considered. Increasing the number of layers increases model accuracy, but there is a number of layers after which further increase causes negligible effects on the overall results. As shown in Fig.3.5 below, the downward flux profile changes by less than 3 W m^{-2} when 18 or more atmospheric layers are used, indicating that grid convergence for DLW is achieved.

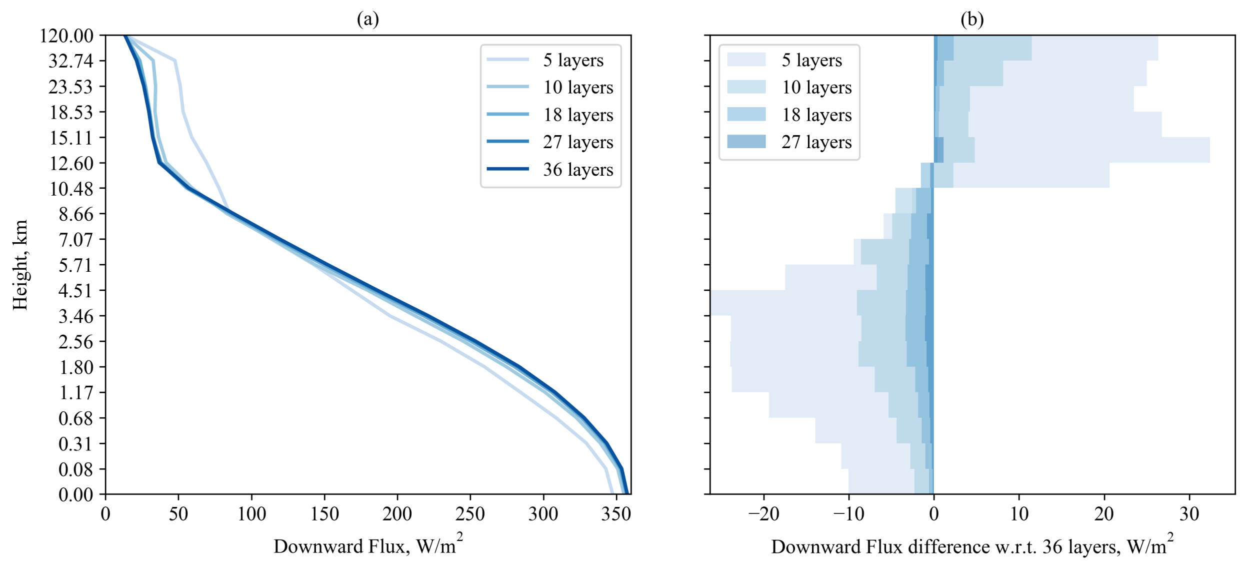

Figure 3.5: (a) Grid dependence on number of layers for broadband DLW; (b) Broadband DLW difference when compared to 36 layers. For this numerical example, surface relative humidity is 70% and $AOD_{497.5}$ is 0.1. The downwelling flux at the top of the atmosphere is from solar radiation.

3.5.2 Comparison with ICRCCM results

In this subsection we validate the proposed model against longwave results from the Intercomparison of Radiation Codes in Climate Models program (ICRCCM) [85]. Aerosols and solar longwave radiation are not included in ICRCCM results. The comparisons for selected cases are listed in Table 3.3, showing that the results of the proposed model are within 2.91% of the mean and within one standard deviation of ICRCCM results. The reference in Table 3.3 is the ICRCCM longwave results produced by Atmospheric Environmental Research, Inc. (AER), with data downloaded from [4]. The DLW flux profiles are plotted in

Fig.3.6 (a) where the difference compared to AER ICRCCM results is smaller than ± 8.5 W/m^2 as shown in Fig.3.6 (b). Spectral comparison with results from AER ICRCCM results is plotted in Fig.3.6 (c). The absolute difference is smaller than 0.035 W cm m^{-2} for all wavenumbers.

Table 3.3: Comparison of surface DLW with ICRCCM results. A midlatitude summer profile is used and the flux values have unit of W m^{-2}.

Case	Case description	ICRCCM Mean [85]	ICRCCM Std [85]	Reference [4]	This work
19	H_2O only, with continuum	326.23	14.06	333.92	335.74
20	H_2O only, without continuum	273.19	17.82	269.02	271.86
27	CO_2, H_2O, O_3 with 300 ppmv CO_2	343.18	8.21	346.91	346.78

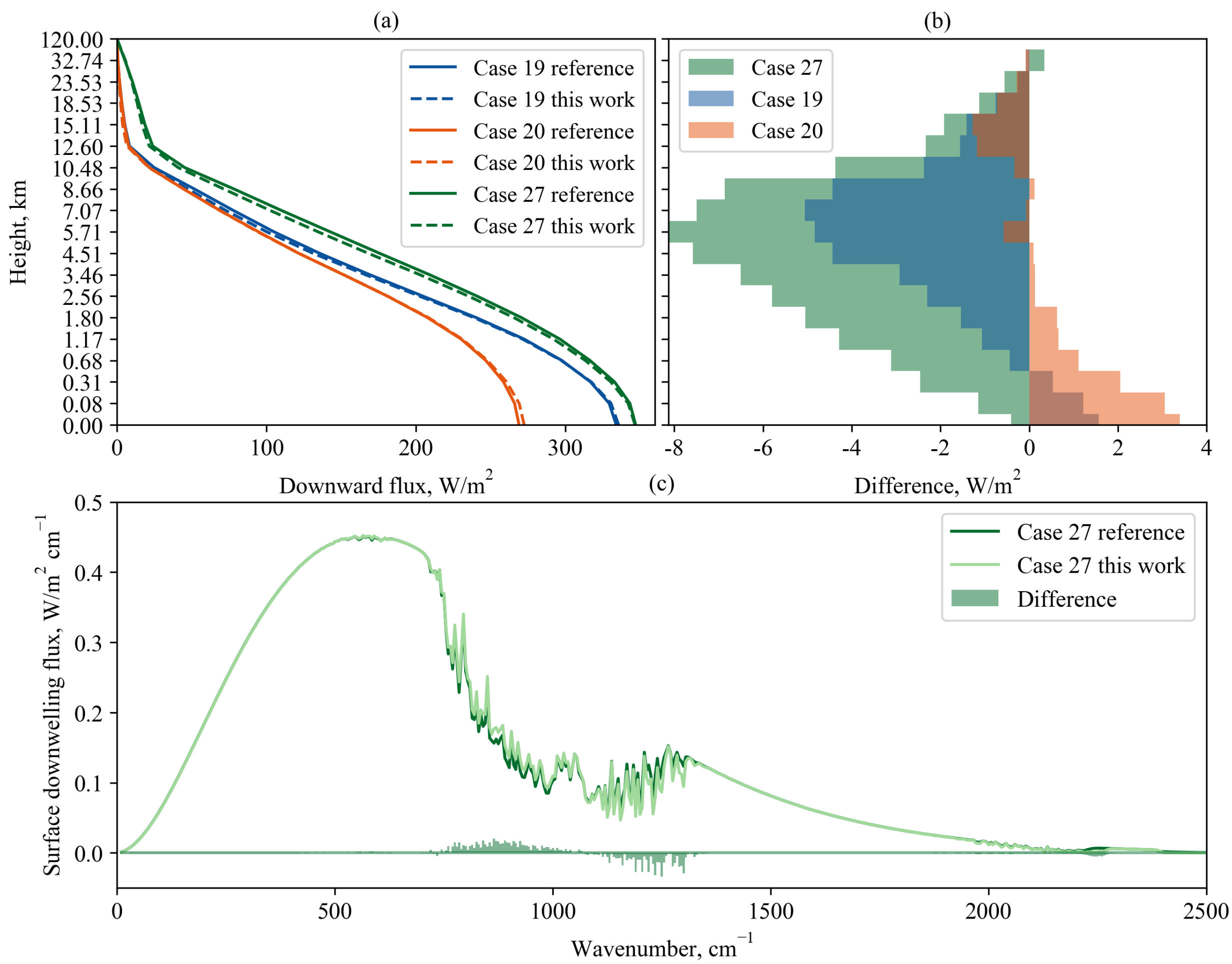

Figure 3.6: (a) Comparison of DLW profiles between the proposed model and Ref. [4]. (b) The difference of DLW fluxes with respect to Ref. [4]. (c) Spectral comparison of surface DLW flux densities.

3.5.3 Comparison with SURFRAD measurements

The comparisons in the previous section indicate the spectral model performs well for non-scattering atmospheres. In this section, we validate the spectral model for scattering atmosphere through a comparison with surface measurements of DLW from 7 SURFRAD stations for the year 2013. Aerosol content is assumed to be $\mathrm{AOD}_{497.5}$ = 0.1243 at the surface (the value 0.1243 is the 2013 annually averaged $\mathrm{AOD}_{497.5}$ for all 7 stations, measured from the surface). Model results are also compared to a calibrated empirical model [16]. During clear sky daytime periods, the surface DLW can be empirically expressed as a function of surface water vapor partial pressure (in hPa),

$$\frac{\mathrm{DLW}}{\sigma T_a^4} = \varepsilon_{\mathrm{sky}} = c_1 + c_2\sqrt{P_w} = 0.598 + 0.057\sqrt{P_w}, \tag{3.40}$$

where $\varepsilon_{\mathrm{sky}}$ is the sky emissivity, $\sigma = 5.67\times10^{-8}\mathrm{W\,m^{-2}\,K^{-4}}$ is the Stefan Boltzmann constant and T_a (K) is surface air temperature. The coefficients c_1 and c_2 are obtained by regression from data from all 7 SURFRAD stations [16].

The proposed spectral model is then used to calculate surface DLW for each of the SURFRAD stations. The SURFRAD stations are located at different altitudes, and the effect of altitude differences is modeled by placing their ground surfaces in different layers according to their altitudes, as shown in Fig. 3.7. The model assumes the AFGL midlatitude summer profile, while the ground level relative humidity ranges from 5% to 100% in the increment of 5%, resulting in 20 different water vapor profiles. Thus, at each altitude z, there are 20 data points of water vapor partial pressure P_w and 20 data points of sky emissivity $\varepsilon_{\mathrm{sky}}$. A one-degree spline is used to interpolate the 20 data points, i.e. $\varepsilon_{\mathrm{sky}} = \mathrm{spl}(P_w)$ as shown in Fig. 3.8. At each station, the sky emissivity is calculated for different values of surface water vapor pressure using the spline interpolation. The surface DLW is then calculated from the sky emissivity using Eq. (3.40).

Model results are compared to measurements using three distinct error metrics proposed in section 1.3.2. Table 3.4 presents the MBE, RMSE and rRMSE of the empirical model and the spectral model when compared to measurements for each individual stations. Compared to the empirical model Eq. (3.40), which is regressed using aggregated data from all 7 stations, the proposed spectral model yields lower RMSE (rRMSE) for 6 out of 7 stations, indicating that the spectral model is able to capture the variability between stations. The model rRMSE ranges from 2.08% to 3.08% for all stations. The performance of the model

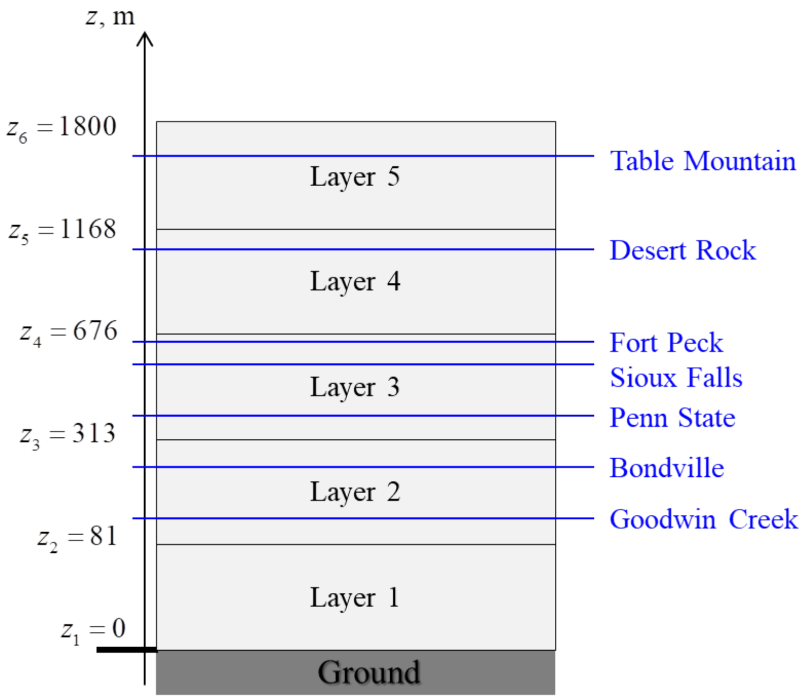

Figure 3.7: Illustration of ground surface locations of the 7 SURFRAD stations used in the model application.

is further illustrated in Fig. 3.8, where biases of the empirical model are more efficiently captured by the spectral model. Note that the proposed model can also be fine-tuned to different pressure-temperature profiles of the atmosphere, but these comparisons show that the model is robust enough to perform well for different microclimates using the standard AFGL midlatitude summer profile.

3.5.4 Comparison with CIRC results for cloudy period

The modeling of clear skies are validated against ICRCCM results as well as SURFRAD measurements, as presented in [5]. In this section, the modeling of cloudy skies are validated against the results from cloudy Case 6 and Case 7 of the Continual Intercomparison of Radiation Codes (CIRC) program [86].

Aerosols, solar longwave radiation and scattering by clouds are not included in the CIRC calculations [87]. The temperature, pressure, gas concentration profiles and cloud properties used in the proposed radiative model are obtained from the input files provided on the CIRC website [86] for validation purposes. The summarized model parameters and results of surface downwelling flux (DLW) for Case 6 and Case 7 are presented in Table 3.5. Scenario 1 recovers the CIRC model parameters except that six out of ten gases are included to be consistent with Ref. [5]. Compared with Scenario 1, Scenario 2 further includes the scattering

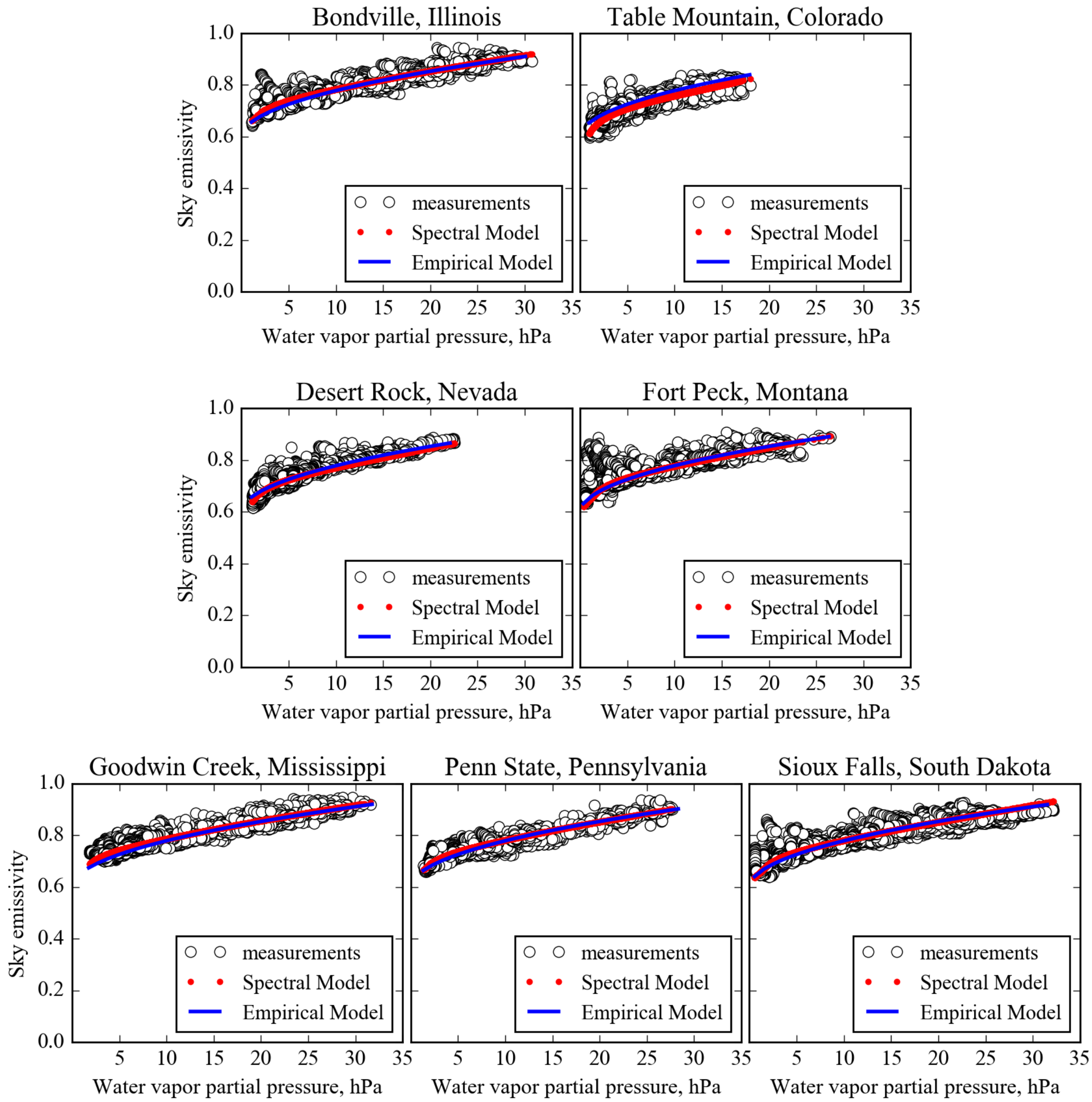

Figure 3.8: Comparison of measured, empirically modeled, and spectrally modeled sky emissivities for the 7 SURFRAD stations.

Table 3.4: Error metrics for empirical and spectral models for estimation of surface DLW during daytime. Bold values indicate best results.

	SURFRAD Stations						
Parameters	Bondville	Table Mountain	Desert Rock	Fort Peck	Goodwin Creek	Penn State	Sioux Falls
Latitude (°)	40.05	40.13	36.62	48.31	34.25	40.72	43.73
Longitude (°)	-88.37	-105.24	-116.02	-105.10	-89.87	-77.93	-96.62
Altitude (m)	213	1689	1007	634	98	376	437
Average T_a (°C)	14.0	14.1	21.9	11.4	18.2	14.6	11.6
25th percentile of T_a (°C)	5.0	7.3	14.6	0.4	11.1	9.4	0.2
75th percentile of T_a (°C)	23.3	21.6	30.1	22.9	26.1	21.1	23.0
Average P_w (hPa)	11.9	7.2	5.1	8.9	14.3	11.1	11.1
25th percentile of P_w (hPa)	5.0	3.4	3.1	4.0	6.4	4.9	4.4
75th percentile of P_w (hPa)	18.0	10.6	5.8	13.7	21.7	16.5	17.0
Empirical MBE (W/m^2)	2.64	-6.82	**3.34**	3.91	4.62	**0.46**	1.30
Empirical RMSE (W/m^2)	7.62	9.70	**6.93**	9.60	8.53	7.34	9.07
Empirical rRMSE (%)	2.47	3.41	**2.18**	3.20	2.54	2.44	2.99
Computed MBE (W/m^2)	**-0.02**	**0.61**	4.52	**3.85**	**1.35**	-1.58	**0.15**
Computed RMSE (W/m^2)	**6.86**	**6.93**	7.65	**9.25**	**6.97**	**6.95**	**8.68**
Computed rRMSE (%)	**2.22**	**2.43**	2.40	**3.08**	**2.08**	**2.31**	**2.86**

by cloud droplets. Scenario 3 adds aerosols where the aerosol profile is adapted from Ref. [5]. Scenario 4 adds the $\sim$ 13 W m^{-2} extraterrestrial longwave irradiance. Scenario 5 uses the Gamma cloud droplet size distribution presented before, while also keeping the liquid water path (LWP) unchanged. The results of the proposed radiative model are within 3% of the CIRC measurements (339.0 W m^{-2} and 373.2 W m^{-2} for Case 6 and Case 7, respectively) for all scenarios. Since the measurements have uncertainties of 3% [87], the proposed model produces reliable results that are within the uncertainties of the measurements.

The comparisons of different scenarios are presented in Fig. 3.9 and Fig. 3.10 for Case 6 and Case 7, respectively. The difference between S2 and S1 indicates the contribution of cloud scattering, which reduces the downwelling flux of the cloud layers and the layers below the clouds because part of the longwave radiation is scattered to outer space. The contribution of aerosols is quantified by the difference between S3 and S2, which increases the downwelling flux above the cloud layers while the surface downwelling flux is nearly unchanged. In the cloud layers and the layers below the clouds, the contribution of aerosols is diminished by the presence of clouds. By comparing Figs. 3.10 and 3.9, the aerosol contribution is more distinct when optically thin clouds are present (Case 7). The contribution of longwave irradiance from the Sun increases the downwelling flux above the cloud layers as shown by the difference between S4 and S3.

Table 3.5: Comparison of the proposed radiative model with ICRC results as well as different scenarios. Different inputs between scenarios are highlighted in bold fonts.

	CIRC modeled [86]	Scenario 1	Scenario 2	Scenario 3	Scenario 4	Scenario 5
Spectral resolution, cm^{-1}	1	1	1	1	1	1
P, T and gas concentration profiles	CIRC	CIRC	CIRC	CIRC	CIRC	CIRC
Number of modeled gases*	10	**6**	6	6	6	6
$AOD_{497.5}$	0	0	0	**0.10**	0.10	0.10
Longwave from solar irradiance, $W\,m^{-2}$	0	0	0	0	**13.29**	13.29
Effective radius of cloud droplets, μm	CIRC	CIRC	CIRC	CIRC	CIRC	**10.00**
Effective variance of cloud droplet radius	0.014	0.014	0.014	0.014	0.014	**0.100**
Spectral dispersion of cloud droplet radius	0.12	0.12	0.12	0.12	0.12	**0.35**
Liquid water path, $g\,cm^{-2}$	CIRC	CIRC	CIRC	CIRC	CIRC	CIRC
Scattering of LW by clouds and aerosols	none	none	**included**	included	included	included
Case 6						
Number of layers	69	69	69	69	69	69
Ground altitude, m	320	320	320	320	320	320
Cloud thickness, m	1600	1600	1600	1600	1600	1600
$COD_{497.5}$	61.66	61.66	61.66	61.66	61.66	**41.17**
Surface downwelling flux, $W\,m^{-2}$	335.20	334.39	329.47	329.51	329.51	331.60
Relative error to measured 339.0 $W\,m^{-2}$, %	-1.12	-1.36	-2.81	-2.80	-2.80	-2.18
Case 7						
Number of layers	59	59	59	59	59	59
Ground altitude, m	2.4	2.4	2.4	2.4	2.4	2.4
Cloud thickness, m	120	120	120	120	120	120
$COD_{497.5}$	6.96	6.96	6.96	6.96	6.96	**6.11**
Surface downwelling flux , $W\,m^{-2}$	372.60	373.87	370.42	370.50	370.63	370.95
Relative error to measured 373.2 $W\,m^{-2}$, %	-0.16	0.18	-0.74	-0.72	-0.69	-0.60

Notes*: CIRC models 10 atmospheric gases: H_2O, CO_2, O_3, N_2O, CH_4, O_2, CO, CCL4, CFC11 and CFC12. The proposed radiative model in this work includes the first six gases.

The downwelling flux remains nearly unchanged in or below the cloud layers since the clouds 'shield' the longwave radiation from the layers above, so that layers below the clouds 'see' only the clouds. The difference between S5 and S4 shows the contribution of cloud droplet size distribution. The proposed size distribution has ~ 30% lower COD when compared with the one used in CIRC (see Table 3.5), which increases the downwelling flux in and below the cloud layers. The difference is more distinct for optically thick clouds (Case 6) when comparing Figs. 3.9 and 3.10. The spectral differences between scenarios show up only in the atmospheric windowing bands (400 ~ 650 cm^{-1} and 750 ~ 1400 cm^{-1}). The surface downwelling flux for the five scenarios are presented in Table 3.5, where the differences between scenarios are smaller than 5 $W\,m^{-2}$, indicating that the surface downwelling flux is insensitive to the cloud scattering, aerosols, extraterrestrial longwave radiation and cloud droplet size distributions under cloudy skies.

3.6 Conclusions

The primary goal of this Chapter is to develop an effective *minimal* model that incorporates the main physical mechanisms needed for calculation of the atmospheric downwelling longwave radiation at the ground level for widely different geographical sites. The operative word *effective* here means a complete model that is capable of discerning the effects of the main contributors to DLW while allowing for fast computations that can be performed by mini computers within time frames compatible with both the time scale of variations in the atmosphere, but also with time scales of engineering systems (power plants, etc.). All main features of the model and its implementation are described within the body of this work.

A secondary goal is to examine the effects of water vapor, carbon dioxide and aerosols content on the surface DLW at high spectral resolutions. A spectrally resolved, multi-layer radiative model is developed to calculate surface downwelling longwave (DLW) irradiance (0 ~ 2500 cm^{-1}) under clear-sky (cloud-free) conditions. The wavenumber spectral resolution of the model is 0.01 cm^{-1} and the atmosphere is represented by 18 non-uniform plane-parallel layers with the pressure of each layer determined by a constant σ coordinate system. Standard AFGL profiles for temperature and atmospheric gas concentrations have been adopted with the correction for current surface atmospheric gas concentrations. The model incorporates the most up-to-date (2016) HITRAN molecular spectral data for 7 atmospheric gases: H_2O, CO_2, O_3, CH_4, N_2O, O_2 and N_2. The MT_CKD model is used to calculate water vapor and CO_2 continuum absorption coefficients.

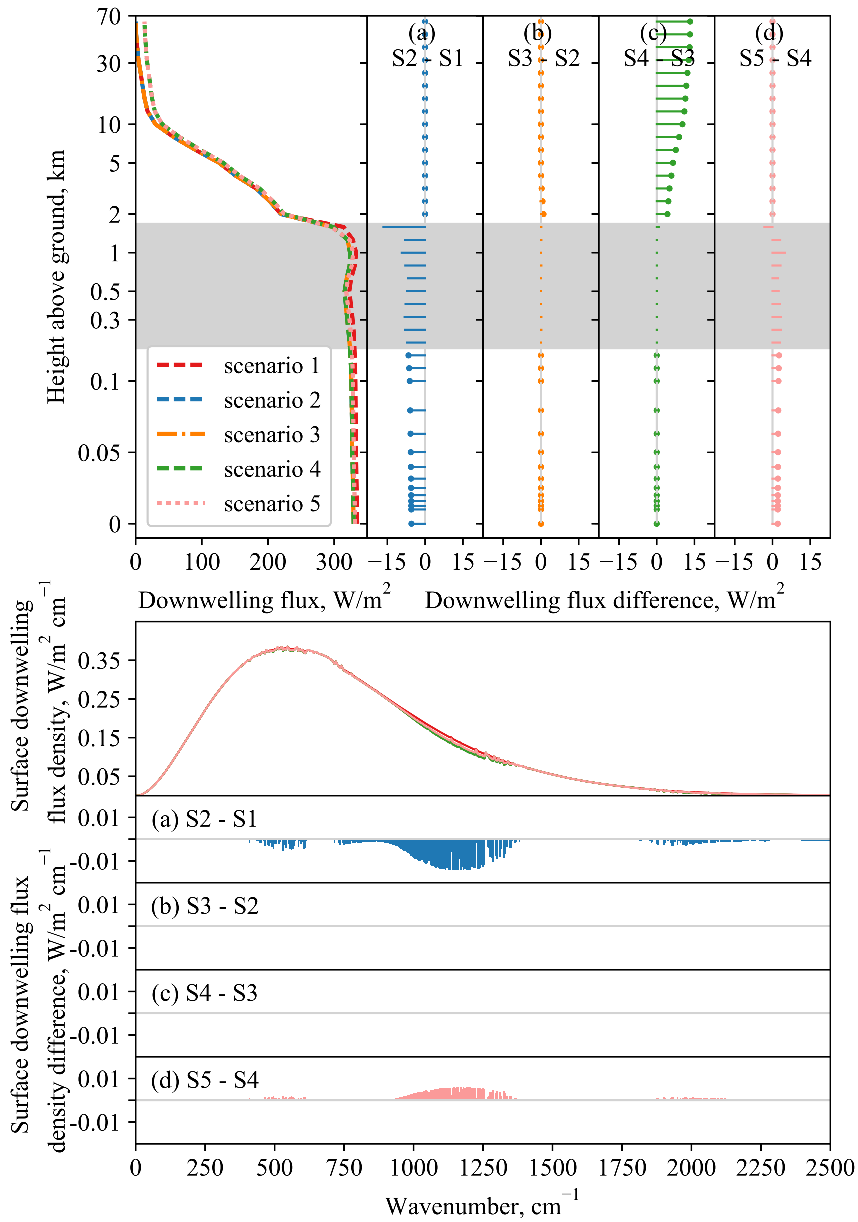

Figure 3.9: Comparison of downwelling flux profiles and surface downwelling flux densities between different scenarios for Case 6. Gray areas indicate cloud layers. Columns (a), (b), (c), (d) show the difference between Scenarios 2 and 1, 3 and 2, 4 and 3, 5 and 4, respectively.

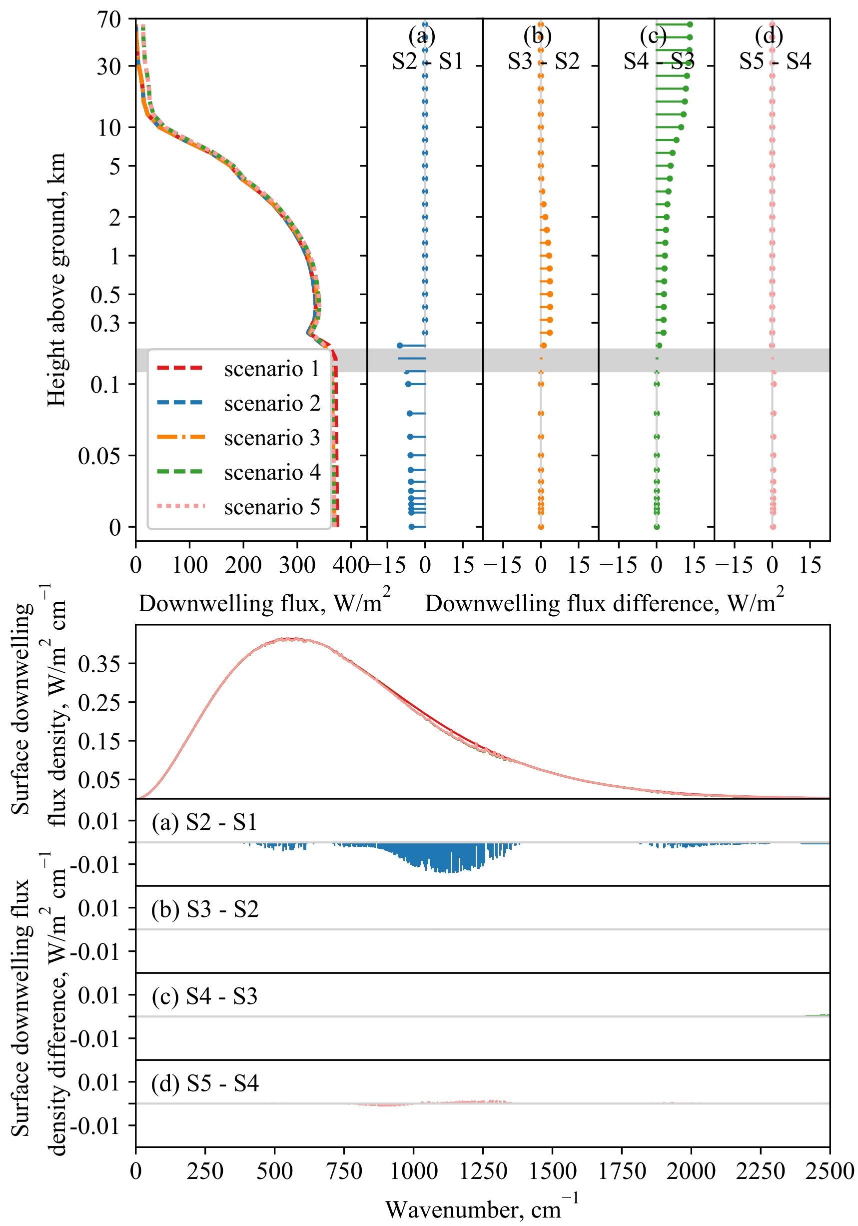

Figure 3.10: The same as Fig.3.9 but for Case 7.

For a scattering atmosphere (with aerosols), the aerosol size distribution is assumed to follow a bimodal distribution. The size and refractive index of aerosols change as they absorb water, therefore the size distribution and refractive index are corrected for different values of local water vapor concentrations (relative humidity values). The absorption coefficients, scattering coefficients and asymmetry factors for aerosols are calculated from the refractive indices for different size distributions by Mie theory. The radiosity and irradiance of each layer are calculated by energy balance equations using transfer factors with the assumption of isotropic aerosol scattering (the δ-M approximation is used to scale anisotropic scattering). The monochromatic downwelling and upwelling fluxes with scattering for each layer are further calculated using a recursive plating algorithm. Broadband fluxes are integrated over the spectrum for both non-scattering and scattering atmospheres.

A model with 18 vertical layers is found to achieve grid independence for DLW. For a non-scattering atmosphere (aerosol free), the calculated surface DLW irradiance agrees within 2.91% with the mean values from InterComparison of Radiation Codes in Climate Models (ICRCCM) program, and the spectral density difference is smaller than 0.035 $\mathrm{W\,cm\,m^{-2}}$. For a scattering atmosphere, the modeled DLW irradiance agrees within 3.08% relative error when compared to measured values from 7 climatologically diverse SURFRAD stations. This relative error is smaller than the error from a calibrated empirical model regressed from aggregate data for those same 7 stations, i.e., the proposed model captures the climatological differences between stations. We also note that these deviation values are within the uncertainty range (+/- 5 $\mathrm{W\ m^{-2}}$) of pyrgeometers ($\sim$ 3% uncertainty).

In summary, the proposed model is capable of capturing climatological and meteorological differences between locations when compared to extensive surface telemetry, which justifies its use for calculating DLW at other locations across the contiguous United States where measurements are not readily available. The proposed model also serves as a powerful and robust tool to study high spectral resolution interactions between atmospheric constituents within the critical longwave region of the electromagnetic spectrum.

3.7 Acknowledgments

This Chapter, in full, is a combination of three publications: M. Li, Z. Liao, and C. F. M. Coimbra (2018) “Spectral model for clear sky atmospheric longwave radiation” *Journal of Quantitative Spectroscopy*

and Radiative Transfer, 209, 196-211; M. Li, Z. Liao and C. F. M. Coimbra (2018) “An Efficient Spectral Model for Evaluating Spectral and Spatial Distributions of Clear Sky Atmospheric Longwave Radiation,” accepted for the *16th International Heat Transfer Conference (IHTC-16)*; M. Li, and C. F. M. Coimbra (2018) “On the Effective Spectral Emissivity of the Sky,” submitted to *Proceedings of the National Academy of Sciences of the United States of America*. The dissertation author is the first author of these manuscripts.

Chapter 4

Analysis of longwave radiative transfer in the atmosphere

4.1 Computational performance

The LBL model proposed in Chapter 3 employs the two-flux approximation (i.e., avoids directional discretization), reusable transfer factors and a recursive plating algorithm for aerosol scattering with the objective of improving overall computational performance for calculation of atmospheric DLW radiation using high-resolution spectral data. The complete model is easily coded in Python within a few hundred lines of code. Wavenumbers are vectorized so that CPU time is only weakly dependent on spectral resolution when adapting the plating algorithm. As a comparison with a radiation model that can also be easily coded in Python, the speed of computation of a standard Monte Carlo simulation is linearly proportional to spectral resolution. A single run of the complete model described in this work requires 100s of Intel Xeon E5-2640 CPU time, where each run corresponds to one data point in Fig. 4.1. The use of the recursive plating algorithm alone reduces the total computational time by 30% when compared to direct matrix reduction. By contrast, an efficient Monte Carlo simulation for the same single case using 50,000 representative photon bundles emitted from each layer requires 90 minutes in the same CPU with 100 times smaller spectral resolution (1 cm^{-1}). In other words, the proposed model is 3000 to 5400 times faster than an equivalent Monte Carlo simulation. Although other radiative models (e.g., those based on discrete-ordinate methods) used in commercial codes also far outperform Monte Carlo simulations in terms of CPU time consumption, there are fewer options for doing so while retaining the level of accuracy and model robustness presented here, and not requiring either thousands of lines of FORTRAN/C coding, and/or expensive yearly fees for the use of optimized commercial products. The model proposed in this work is readily and efficiently implementable in high-level, open-source interpreted computer languages like Python, can easily accommodate different pressure-temperature and aerosol profiles, is only weakly dependent on spectral resolution, and is fast enough to be computed in real-time (within time constants of interest to DLW variability) using low-cost mini-computers.

4.2 Surface downwelling longwave irradiance under clear skies

4.2.1 Broadband contributions of water vapor, carbon dioxide and aerosols

Broadband surface DLW as a function of surface water vapor partial pressure and $AOD_{497.5}$ is plotted in Fig.4.1. The DLW increases with surface water vapor pressure as well as $AOD_{497.5}$, indicating that water vapor and aerosols are warming the surface. The aerosol warming effect is more obvious when there is little water vapor present, which is consistent with previous works [77]. When $AOD_{497.5} = 0.1$, the aerosol direct forcing is 6.57 W m^{-2} for drier conditions (RH = 5%), and 1.86 W m^{-2} for wetter conditions (RH = 95%).

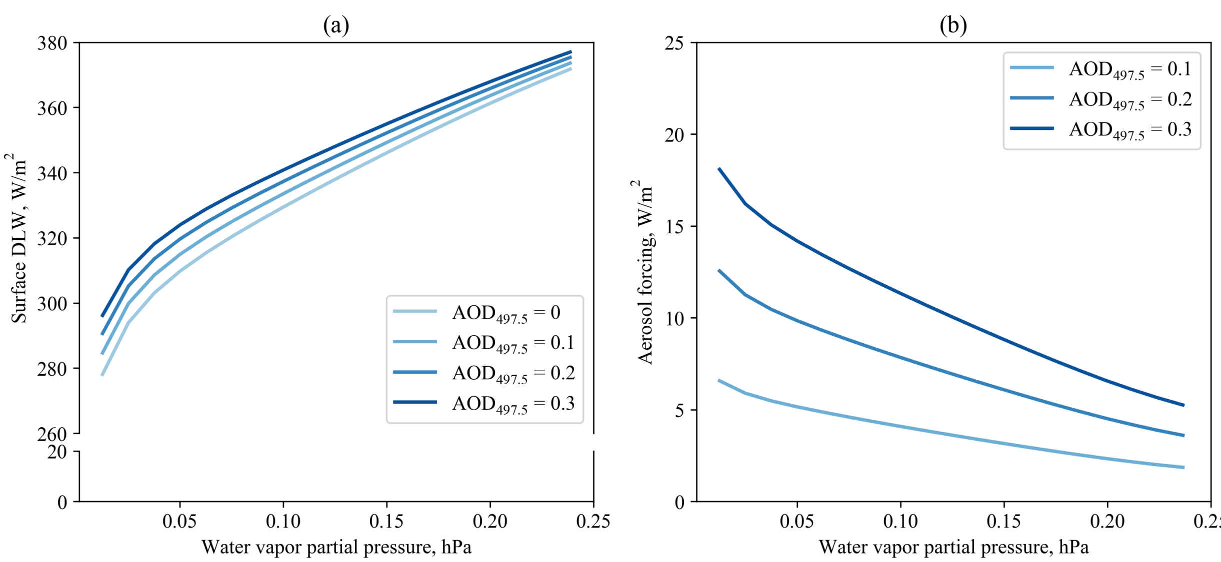

Figure 4.1: Surface DLW with respect to surface water vapor partial pressure and aerosol optical depth.

Broadband surface downwelling and top of atmosphere (TOA) upwelling longwave radiation as a function of surface water vapor partial pressure and surface CO_2 volumetric mixing ratio w_{CO_2} are plotted in

Fig. 4.2. The surface downwelling flux increases with surface water vapor pressure as well as surface w_{CO_2}, indicating that water vapor and CO_2 are warming the surface by increasing the downwelling flux. Clearly, CO_2 warming effects are weaker for increased water vapor content because of band overlapping. The CO_2 contribution to surface downwelling flux is around 0.3 ~ 1.2 W m^{-2} per 100 ppm CO_2 increment, where 1.2 W m^{-2} for drier conditions, and 0.3 W m^{-2} for wetter conditions. The TOA upwelling flux decreases with surface water vapor pressure as well as surface w_{CO_2}, indicating that water vapor and CO_2 are warming the atmosphere by preventing longwave radiation to escape to outer space. Around 0.5 ~ 0.7 W m^{-2} TOA upwelling longwave flux is decreased per 100 ppm CO_2 increment, where 0.7 W m^{-2} for drier conditions, and 0.5 W m^{-2} for wetter conditions. Note that the calculated effects of CO_2 and H_2O discussed here are first-order effects, without consideration of feedback effects. If feedback is positive, these are lower estimates for the fluxes, if the feedback is negative, then these are upper limit estimates.

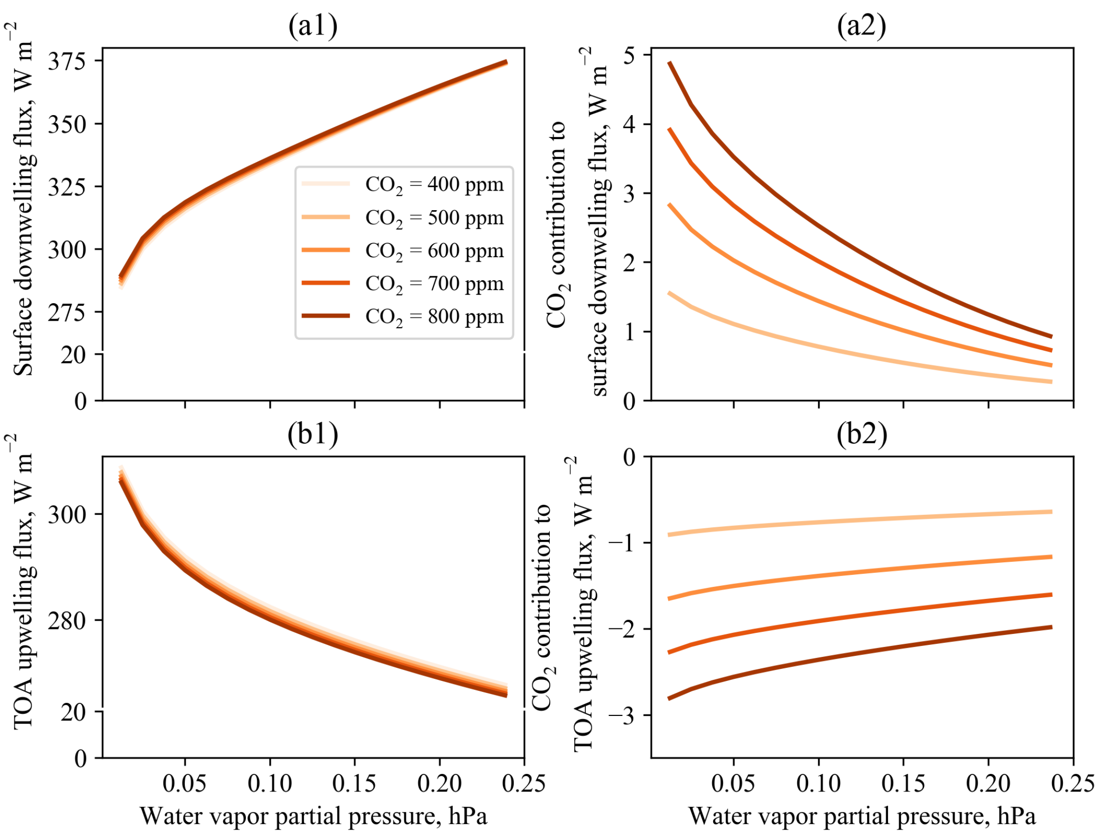

Figure 4.2: Broadband contribution of atmospheric CO_2 to (a) surface downwelling and (b) TOA upwelling fluxes. The right column shows difference relative to 400 ppm CO_2 scenario.

4.2.2 Broadband contributions from each constituent

Brunt (1932) has shown that the broadband sky emissivity is strongly correlated to the concentration of water vapor and temperature at the screening (ground) level [31]. The strong correlation results from two different but related mechanisms: i) the value of broadband sky emissivity is dominated by contributions from the lowest layers of the atmosphere, especially during humid ambient conditions, and ii) the wide absorption bands of water vapor dominate thermal absorption over most of the infrared spectrum, in particular when conditions are wet. For dry conditions, and in specific bands of the spectrum where water vapor is less absorbing, other atmospheric constituents play a significant role.

The radiosity of the sky and the effective sky emissivity are defined as,

$$\begin{aligned} J_{\text{sky}} &= \int_0^{+\infty} q^-(\nu)d\nu \\ \varepsilon_{\text{sky}} &= \frac{J_{\text{sky}}}{\sigma T_a^4} \end{aligned} \tag{4.1}$$

where $q^-(\nu)$ is the monochromatic downwelling flux density at the surface, ν is the wavenumber (cm^{-1}), $\sigma = 5.67 \times 10^{-8}$ W m K^{-4} is the Stefan-Boltzmann constant and T_a (K) is the air temperature at the screening level (10 m above the surface).

We consider the broadband contribution of H_2O to the ε_{sky} when only H_2O is participating (because H_2O is the main constituent responsible for the vertical temperature profile in the troposphere). Contributions of other atmospheric constituents are obtained by calculating the difference of ε_{sky} when the constituent were absent. Therefore, the net contribution (devoid of band overlaps) of constituent i to ε_{sky} is calculated as,

$$\begin{aligned} \varepsilon_{\text{sky},i} &= \frac{J_{\text{sky}}(w_i)}{\sigma T_a^4} \quad \text{for } i = \mathrm{H_2O} \\ \varepsilon_{\text{sky},i} &= \frac{J_{\text{sky}}(\sum_k w_k) - J_{\text{sky}}(\sum_{k\neq i} w_k)}{\sigma T_a^4} \quad \text{for } i \neq \mathrm{H_2O} \end{aligned} \tag{4.2}$$

where w_i represents the volumetric mixing ratio of constituent i. Since the band overlaps have been extracted more than once when calculating $J_{\text{sky}}(\sum_{k\neq i} w_k)$, so an $\varepsilon_{\text{overlap}}$ term is added to account for the total band overlaps. Then ε_{sky} is expressed as,

$$\varepsilon_{\text{sky}} = \sum_i \varepsilon_{\text{sky},i} + \varepsilon_{\text{sky,overlap}} \tag{4.3}$$

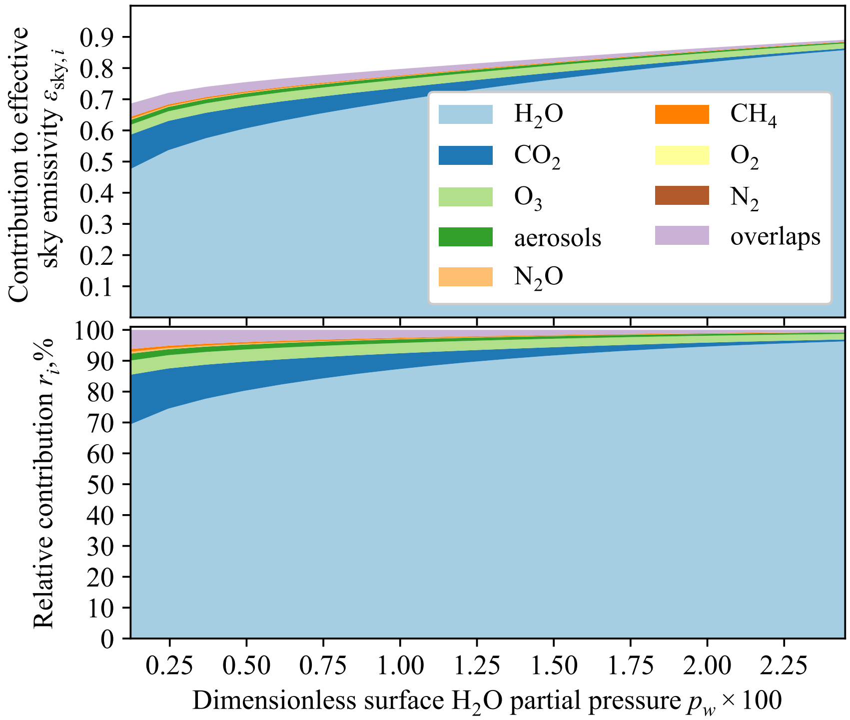

Figure 4.3: Broadband contribution of each atmospheric constituent to effective sky emissivity. Upper and lower subplots show absolute and relative contributions, respectively.

The relative contribution of each constituent and overlap is then,

$$r_i = \frac{\varepsilon_{\text{sky},i}}{\varepsilon_{\text{sky}}} \tag{4.4}$$

The absolute and relative contributions of atmospheric constituents are plotted in Fig. 4.3 with respect to normalized partial pressure of water vapor p_w at the screening level ($p_w = P_w/P_0$ where $P_0 = 1.013 \times 10^5$ Pa). The absolute and relative contributions of H_2O increase with p_w while those of other constituents decrease with p_w. When sufficient H_2O is present in the atmosphere, most of the bands are saturated by water vapor, leaving other constituents' contributions negligible. Water vapor contributes from 69.42% (dry conditions) to 96.27% (humid conditions) of the broadband effective sky emissivity while CO_2 contributes from 16.06% to 0.63%. The contribution of O_3 ranges from 4.59% to 1.79%. The contributions of aerosols range from 2.25% to 0.45% and of N_2O and CH_4 range from approximately 0.87% to 0.12%, while oxygen and nitrogen contribute a negligible amount.

The contribution of each constituent and overlap to broadband effective sky emissivity are fitted using a power law expression,

$$\varepsilon_{\text{sky},i} = c_{1,i} + c_{2,i}\,(p_w)^{c_{3,i}} \tag{4.5}$$

where $c_{1,i}$, $c_{2,i}$ and $c_{3,i}$ are least-square fitted coefficients, which are presented in Table 4.1. Note that since the empirical expression regressed in Ref. [16] uses water vapor partial pressure P_w in hPa as independent variable instead of dimensionless p_w, the coefficient $c_{2,E}$ ('E' stands for empirical) has been modified accordingly. For the contribution of each constituent, the values of $c_{2,i}$ are negative for constituents other than H_2O because their contributions decrease with more water vapor is present. The $c_{2,i}$ is nearly zero for CH_4 indicating that the contribution of CH_4 is weakly dependent on the amount of H_2O. The contribution of water vapor increases with $(p_w)^{0.3784}$. When all constituents are added, the value of $c_{3,T}$ ('T' stands for total) increases to 0.475, which is consistent with the Empirical model proposed in [16].

4.2.3 Spectral band contributions from each atmospheric constituent

To further analyze the spectral contribution of each atmospheric constituent, the longwave spectrum is divided into seven bands: four absorbing bands and three window (non-absorbing) bands. The two absorbing bands of water vapor are (b1) 0 - 400 cm^{-1} and (b5) 1400 - 2250 cm^{-1}. The two absorbing bands of CO_2 are (b3) 580 - 750 cm^{-1} and (b6) 2250 - 2400 cm^{-1}. The three window bands (b2), (b4) and (b7) are in between the absorbing bands. The band boundaries are found so that only the contribution of water vapor is shown in (b1), (b2), (b5) and (b7), and the contribution of CO_2 is only shown in (b3), (b4) and (b6).

The division of bands with the spectral extinction coefficient of each constituent are plotted in Fig. 4.4 , where the absorbing bands of water vapor and CO_2 are readily identified.

The contributions in band j from atmospheric constituent i is defined as,

$$\varepsilon_{\text{sky},ij} = \varepsilon_{\text{sky},i}(\Delta\nu_j) \tag{4.6}$$

where $\Delta\nu_j$ represents the wavenumber range of band j.

Figure 4.5 plots the contributions in each band from each atmospheric constituent with respect to p_w. The contributions from bands (b6) and (b7) are small because little longwave would be emitted in those wavenumbers according to Planck's law. A small amount of water vapor saturates bands (b1) and (b5) so the contribution of water vapor does not increase with p_w and the contributions from other constituents are

Table 4.1: Regression coefficients for the contribution of each constituent to the broadband effective sky emissivity given by Eq. 4.5.

	H_2O	CO_2	O_3	aerosols	N_2O	CH_4	O_2	N_2	overlaps	total	empirical [16]
c_1	0.2996	0.2727	0.0321	0.0178	11.4241	0.0245	-	-	0.0705	0.63042	0.5980
c_2	2.2747	-0.5211	-1.2828	-0.1116	-11.4289	-0.0314	-	-	-0.1870	1.50399	1.8140
c_3	0.3784	0.1766	1.1768	0.5615	0.0001	0.0786	-	-	0.2857	0.47539	0.5000
R^2	0.9998	0.9959	0.9997	0.9992	0.9989	1.0000	-	-	0.9991	0.99777	

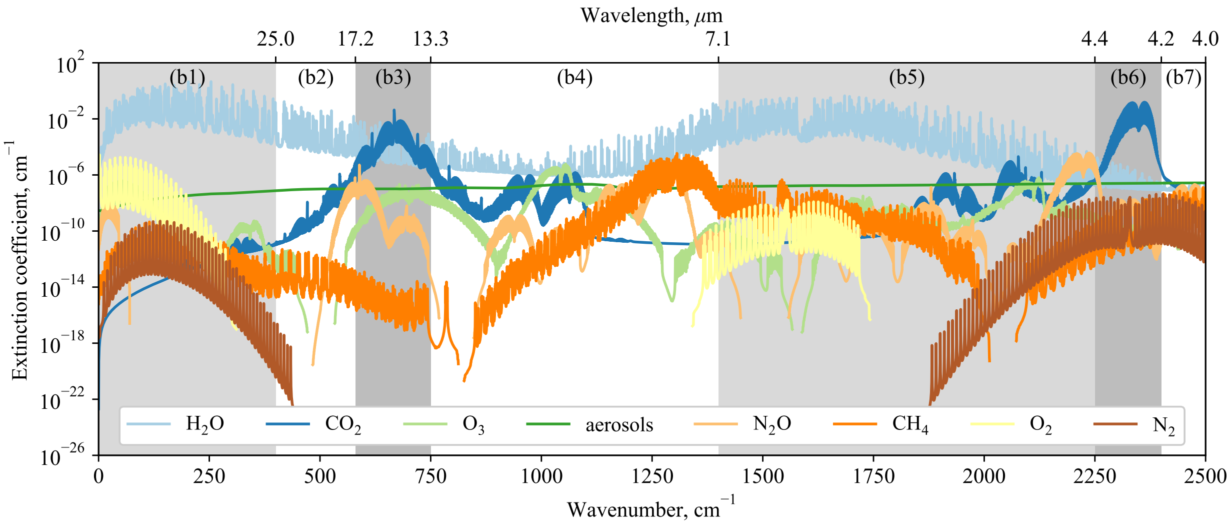

Figure 4.4: Spectral extinction coefficients for main atmospheric constituents at the lowest layer of the troposphere. The absorption coefficients are obtained from HITRAN database and MT_CKD continuum model [5]. The extinction coefficients of aerosols are calculated by Mie thoery [5].

nearly zero in these two bands. For band (b2), the contribution of water vapor increases with increased p_w then becomes saturated when $p_w > 0.01$, and the contributions from other constituents are negligible. Water vapor and CO_2 saturate band (b3), so the total contribution of H_2O and CO_2 plus overlaps is nearly invariant with p_w. The contributions of O_3, N_2O, CH_4 and aerosols are only relevant in band (b4), the so-called 'atmospheric window'. As expected, the contribution of water vapor increases with increased values of p_w while the relative contributions from other constituents decrease. Note that band (b4) is not saturated even when very high water vapor content is present in the atmosphere.

The contributions from each constituent in each band to the broadband effective sky emissivity are fitted using Eq. 4.5 and the coefficients of c_1, c_2 and c_3 are tabulated in Table 4.2. Since band (b2) shows a non-power law asymptotic behavior, a hyperbolic function is used as the fitting function instead. With these tabulated values, each individual contribution to the different atmospheric bands can be easily calculated for any value of ambient p_w.

Figure 4.6 presents the relative contribution in each band from each constituent $r_{i|j}$, which is defined as,

$$r_{i|j} = \frac{\varepsilon_{\text{sky},ij}}{\varepsilon_{\text{sky},j}} \tag{4.7}$$

where $\varepsilon_{\text{sky},ij}$ is the contribution in band j from atmospheric constituent i and $\varepsilon_{\text{sky},j}$ is the contribution in band

Table 4.2: The fitting coefficients of contribution of each constituent in each band to ε_{sky}.

	Constituent	H_2O	CO_2	O_3	aerosols	N_2O	CH_4	O_2	N_2	overlaps	Total
band (b1)	c_1	0.1725	-	-		-	-	-	-	-	0.1725
	c_2	-	-	-		-	-	-	-	-	-
	c_3	-	-	-		-	-	-	-	-	-
	R^2	-	-	-		-	-	-	-	-	-
band (b2)*	c_1	0.1083	0.0002	-	0.0002	0.0001	-	-	-	0.0002	0.1171
	c_2	0.0748	-	-	-	-	-	-	-	-	0.0661
	c_3	270.8944	-	-	-	-	-	-	-	-	269.6852
	R^2	0.9927	-	-	-	-	-	-	-	-	0.9925
band (b3)	c_1	-0.2308	0.2864	0.0001	0.0001	0.0001	-	-	-	0.1119	0.1440
	c_2	0.6484	-0.4879	-	-	-	-	-	-	-0.1422	0.0429
	c_3	0.1280	0.1454	-	-	-	-	-	-	0.0651	0.0906
	R^2	0.9953	0.9951	-	-	-	-	-	-	0.9948	0.9985
band (b4)	c_1	0.0289	0.0131	0.0325	0.0144	0.0018	0.0244	-	-	0.0240	0.1237
	c_2	6.2436	-0.1600	-1.2537	-0.2471	0.0000	-0.0313	-	-	-0.2897	5.3298
	c_3	0.9010	0.7269	1.1678	0.8529	0.0000	0.0791	-	-	0.7461	0.9519
	R^2	0.9998	0.9979	0.9998	0.9988	0.0000	1.0000	-	-	0.9992	0.9998
band (b5)	c_1	0.0775	-	-0.0005	-	-0.0006	-	-	-	-0.0002	0.0764
	c_2	-	-	-	-	-	-	-	-	-	-
	c_3	-	-	-	-	-	-	-	-	-	-
	R^2	-	-	-	-	-	-	-	-	-	-
band (b6)	c_1	0.0044	-0.0022	-	-	-	-	-	-	-	0.0019
	c_2	-	-	-	-	-	-	-	-	-	-
	c_3	-	-	-	-	-	-	-	-	-	-
	R^2	-	-	-	-	-	-	-	-	-	-
band (b7)	c_1	0.0033	-0.0003	-	-0.0001	-0.0001	-	-	-	-0.0002	0.0026
	c_2	-	-	-	-	-	-	-	-	-	-
	c_3	-	-	-	-	-	-	-	-	-	-
	R^2	-	-	-	-	-	-	-	-	-	-

Note*: For band (b2), the fitting function has the form of a hyperbolic tangent function $\varepsilon_{sky,i} = c_{1,i} + c_{2,i}\tanh(c_{3,i}p_w)$.

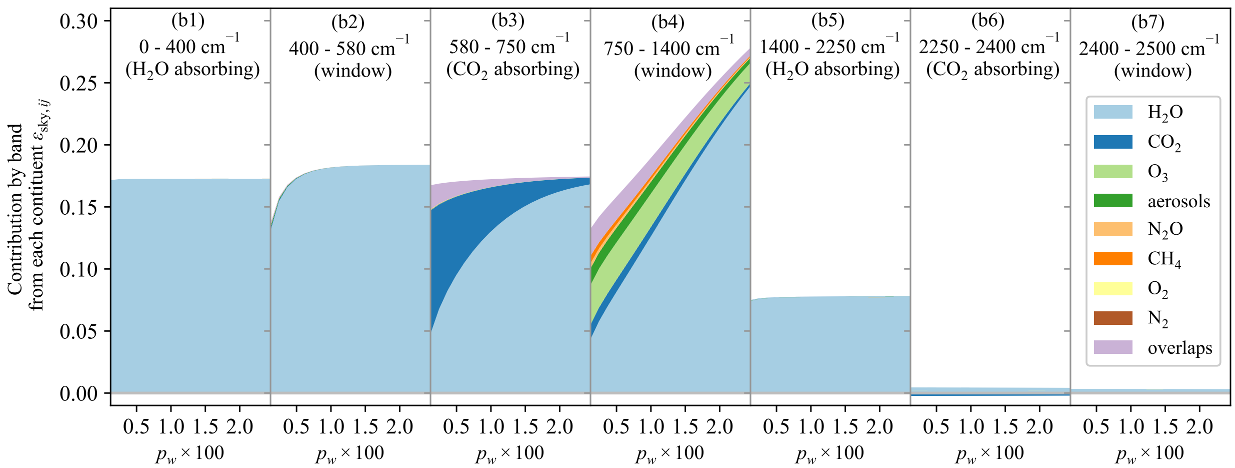

Figure 4.5: Contributions to the effective sky emissivity by atmospheric wavenumber band from each atmospheric constituent.

j from all constituents. In bands (b1), (b2) and (b5), water vapor is the only contributor regardless of ambient p_w. The contribution of CO_2 ranges from 60.0% to 5.0% in band (b3) and ranges from 5.0% to 0% in band (b4). There is a strong absorbing band of O_3 in band (b4) where O_3 contributes to 25% to 8%. For bands (b6) and (b7), CO_2 reduces the effective sky emissivity contributed by water vapor thus resulting in a negative contribution.

Figure 4.7 presents the relative contribution by band from each constituent to the total effective sky emissivity with respect to the ambient p_w, which is defined as,

$$r_{ij} = \frac{\varepsilon_{\text{sky},ij}}{\varepsilon_{\text{sky}}} \tag{4.8}$$

where ε_{sky} is the total effective sky emissivity. Band (b1) contributes to 25% to 19% and the contribution decreases as increased ambient p_w. Band (b2) contributes to 23% to 19% while the contribution first increases then decreases with increased ambient p_w. Band (b3) contributes to 24% to 19% and the contribution of water vapor increases with increased p_w while the contributions of CO_2 and overlap decreases with increased p_w. The contribution of band (b4) increases linearly from 19% to 31% with ambient p_w. Water vapor in band (b5) contributes to approximately 10%. The contributions from bands (b6) and (b7) are smaller than 1%.

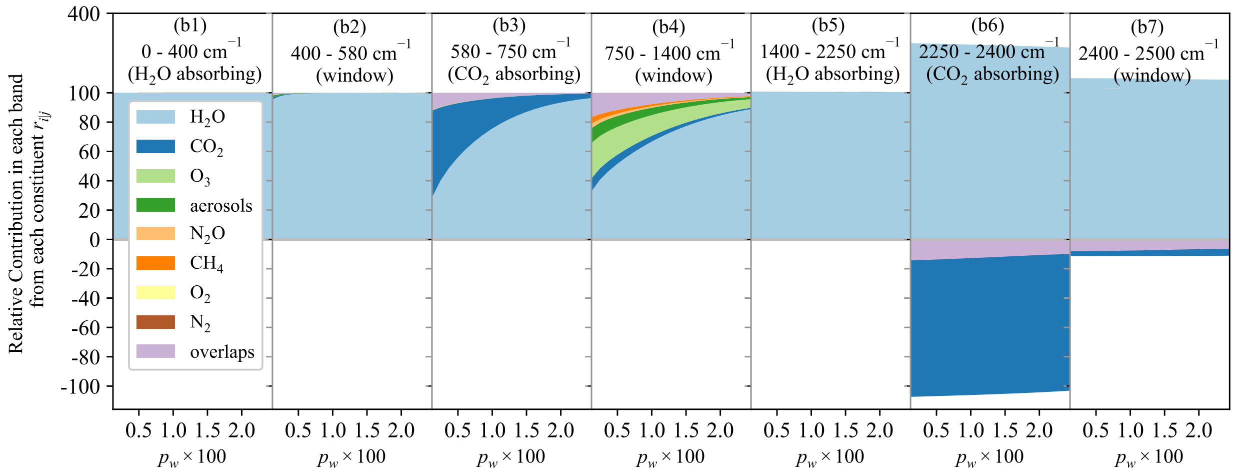

Figure 4.6: Relative contribution from each atmospheric constituent to each band with respect to p_w.

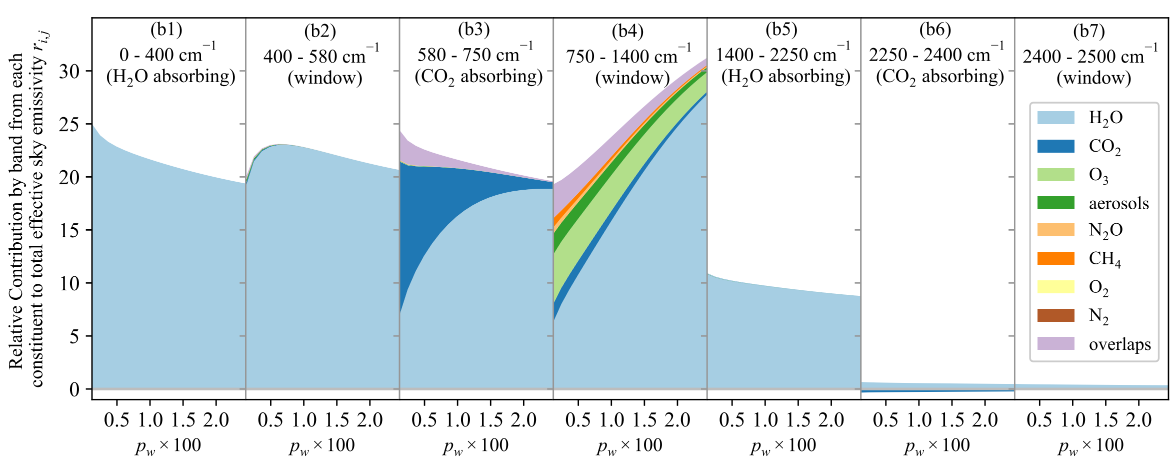

Figure 4.7: Relative contribution by band from each atmospheric constituent to total effective sky emissivity with respect to p_w.

4.2.4 Spectral and spatial contributions of water vapor

The surface value of DLW is a result of contributions of every atmospheric layer above the surface. To examine the spectral and spatial contribution of water vapor, the modified transfer factors $\mathcal{F}_{0,j}^{**}$ are used to express surface monochromatic DLW as,

$$q_1^- = G_0 = \sum_{j=0}^{N+1} \mathcal{F}_{0,j}^{**} \pi \bar{I}_{b,j}. \tag{4.9}$$

Figure 4.8 shows the spatial and spectral contribution of water vapor to surface DLW. The left column and right column show the modified transfer factor $\mathcal{F}_{0,j}^{**}$ and monochromatic flux density $\mathcal{F}_{0,j}^{**} \pi \bar{I}_{b,j}$ of each atmosphere layer, respectively. As shown in Fig. 4.8 (a1), the transfer factors for the absorbing bands of (b1), (b3), (b5) and (b6) are nearly unity in the nearest atmospheric layer, indicating the contribution to surface DLW in these bands are mostly coming from this layer (Fig.4.8 (a2)). Comparing Fig. 4.8 (a1) and (a2), the latter two bands show relatively small contributions in (a2) than in (a1) because $\bar{I}_b$ is relatively small in these two bands. Further increasing the water vapor content has negligible effect on the surface DLW in those bands, as shown in Fig. 4.8 (b), (c) and (d). The contributions of water vapor is mostly from the atmosphere below 1 km in the spectral band (b2). Contributions also come from the band (b4) for heights below 3.46 km. The blue region indicates a decrease in contribution, because water vapor in the layer(s) below absorbs the emitted radiation, preventing the radiation coming from above from reaching the surface.

4.2.5 Spectral and spatial contributions of aerosols

Figure 4.9 shows the spatial and spectral contributions of aerosols from each atmosphere layer, for different surface relative humidity values. The difference of transfer factor (left column) and monochromatic flux density (right column) are with respect to aerosol - free cases. The aerosol contribution to transfer factor is mostly felt within the spectral atmospheric windows: bands (b2), (b4) and (b7) where the single scattering albedo is non-trivial (Fig. 3.3). The latter two windows have negligible effect on the monochromatic flux density because the blackbody intensities in these bands are low. Aerosol forcing mostly comes from the layers below 3.46 km. Above 3.46 km, the blue regions indicate a decrease in transfer factor and monochromatic flux density, because aerosols below prevent the emitted longwave radiation from reaching the surface. In addition, the aerosol forcing effects are accentuated when less water vapor is present, as

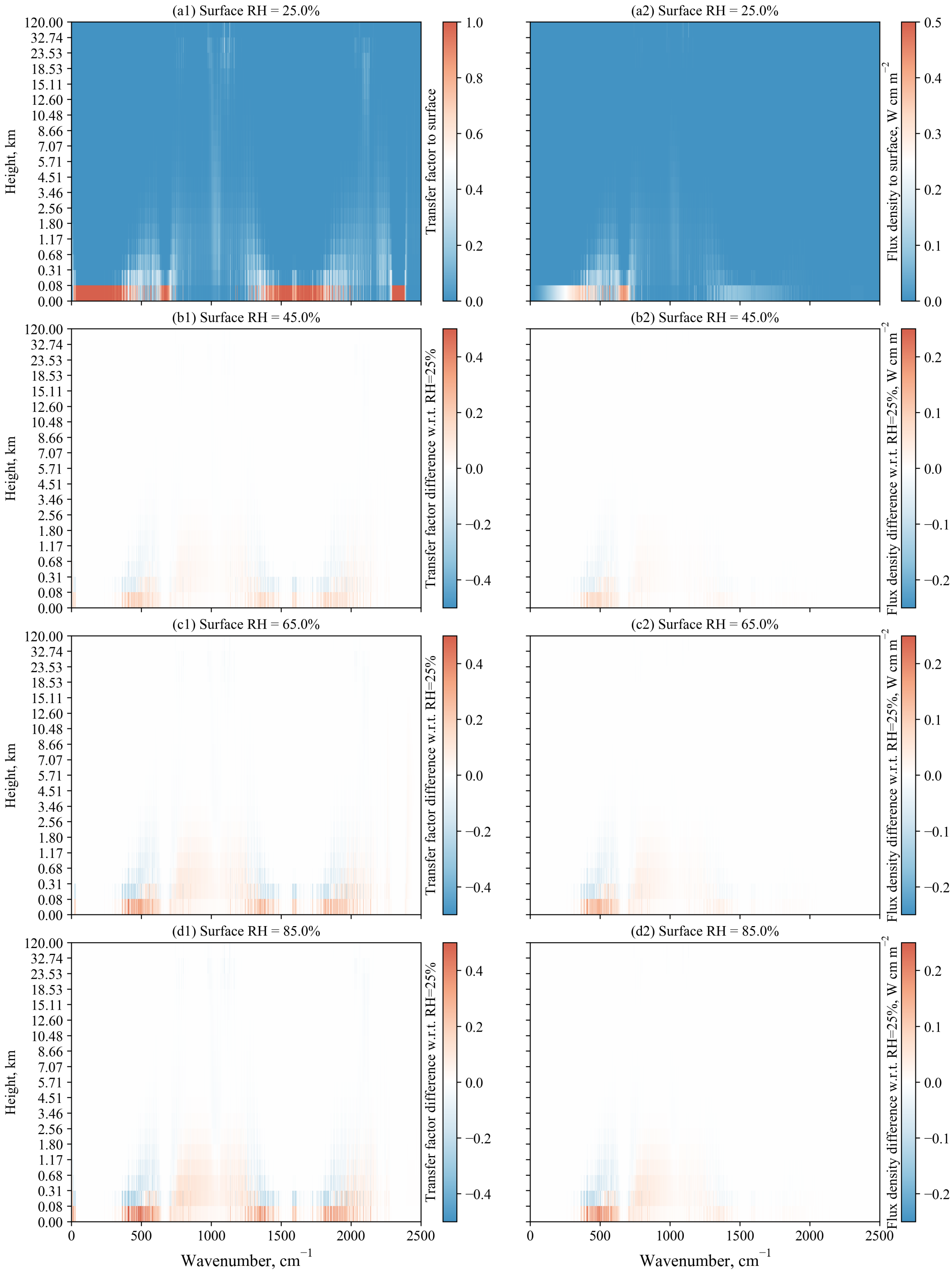

Figure 4.8: Spatial and spectral contributions of water vapor to surface DLW. All differences are compared to ϕ = 25% case.

evidenced by broadband analyses and experiments [12].

4.3 Vertical and spectral distribution of longwave irradiance under clear skies

4.3.1 Vertical and spectral distribution

Figure 4.10 presents the vertical and spectral contribution from all layers to the irradiation on a particular layer. The left column and right column show contributions of the modified transfer factor $\mathcal{F}^*_{n,j}$ and monochromatic flux density $\mathcal{F}^*_{n,j}\pi\bar{I}_{b,j}$, respectively.

As shown in Fig. 4.10 (a1), the transfer factors for the absorbing bands (b1), (b3), (b5) and (b6) are near unity, indicating the surface downwelling flux in these bands are mostly coming from the nearest atmosphere layer (Fig.4.10 (a2)). Comparing Fig. 4.10 (a1) and (a2), the latter two bands show relatively smaller contributions in (a2) than in (a1) because $\bar{I}_b$ is relatively small in these two bands.

Fig. 4.10 (b1) shows that the transfer factors to the nearest atmosphere layer are near unity in the four absorbing bands from the layer itself. The transfer factor from the ground layer is around 0.5 in the atmospheric window bands, i.e. bands (b2), (b4) and (b7). Fig. 4.10 (b2) shows the contributions to flux density from bands larger than 2000 cm^{-1} are negligible because of small $\bar{I}_b$.

Fig. 4.10 (c1) shows that the transfer factor from the tropo-pause layer to itself in the four absorbing bands is the largest compared with from other layers. Notably, the absorbing bands of CO_2 are near unity while the absorbing bands of water vapor are around 0.6 because little water vapor is presented at that altitude (10.48 km ~ 12.60 km) but CO_2 is well mixed below 40 km. The transfer factor from the outer space is around 0.5 except the absorbing bands of CO_2. The contribution to flux density from the outer space is negligible as shown in Fig. 4.10 (c2), because there is only 1% longwave in extraterrestrial solar radiation. The ground layer contributes partially to the transfer factor and the flux density in the window bands.

Fig. 4.10 (d1) shows that the transfer factor from the outer space to the top atmosphere layer dominates. Other contributions come from the ground layer in the window bands, from the middle of atmosphere in the water vapor absorbing bands and from the top of atmosphere in the CO_2 absorbing bands. For flux density in Fig. 4.10 (d2), contributions from the outer space vanishes, leave only contributions from the surface and the middle atmosphere in bands smaller than 1200 cm^{-1}.

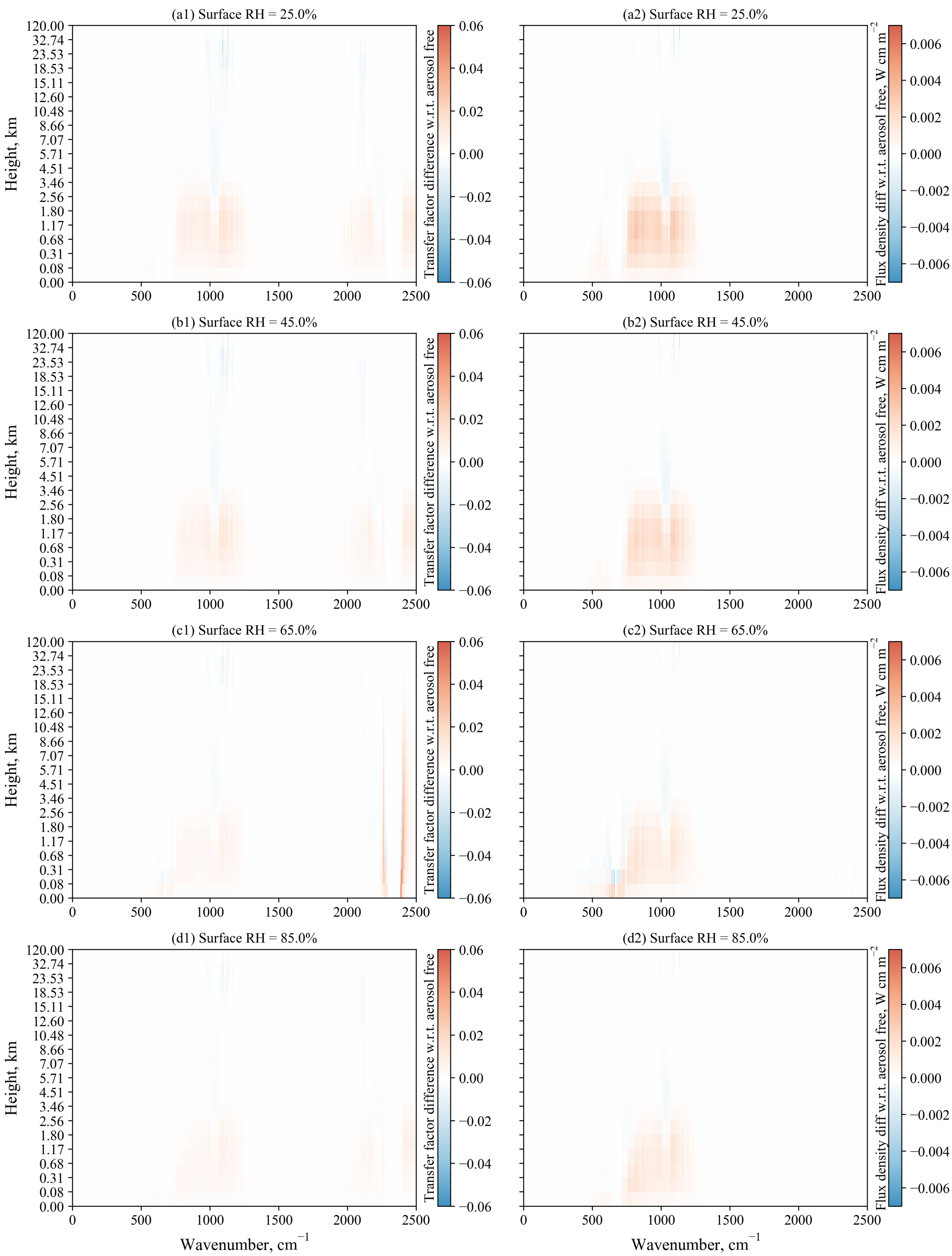

Figure 4.9: Spatial and spectral contributions of aerosols to surface DLW. All differences are compared to aerosol free cases.

Fig. 4.10 (e1) shows that the transfer factor from the surface to the outer space in the window bands is the largest. Other contributions come from the water vapor absorbing bands in the middle of atmosphere and CO_2 absorbing bands in the top of atmosphere. For flux density in Fig. 4.10 (e2), contributions from bands larger than 1200 cm^{-1} vanish.

4.3.2 Broadband contribution to irradiation from each layer

For an atmosphere with surface relative humidity of 65% and aerosol optical depth at 479.5 nm equal to 0.1, the broadband percentage contributions of the transfer factor and irradiation flux of each layer are illustrated in Fig. 4.11 (a) and (b), respectively. The summation of each row in Fig. 4.11 equals to 100%. The outer space layer (layer 19) dominants the transfer factor to upper layers (above tropopause) but the flux contribution is negligible. For the surface layer, 64.4% of its longwave irradiation comes from the nearest atmospheric layer, 15.3% comes from the 2nd nearest layer, 7.5% comes from the 3rd nearest layer and the remainder 12.8% comes from all other layers. For the nearest atmosphere layer, 27.4% of its longwave irradiation comes from the surface, 52.5% comes from itself, 11.2% comes from the layer above it and the rest 8.9% comes from all other layers. Similarly, 18.0% of the 2nd nearest atmospheric layer longwave irradiation comes from the surface, 4.3% comes from the layer below it, 63.2% comes from itself, 8.1% comes from the layer above it, while the remainder 6.4% comes from other layers. From the nearest atmosphere layer to the tropopause layer (layer 13), the largest contribution to the irradiation on the layer is from the layer itself. Above the tropopause, the largest contribution is from the ground layer. The layers above the tropopause contribute less than 4.8% to the irradiance to other layers due to lower temperature levels.

4.4 The effective sky emissivity under cloudy skies

The validation of the radiative model with clouds is presented in the Supporting Information (SI). After the model is validated, it uses the pressure, temperature and constituent profiles proposed in [5]. The clouds are placed in different layers with predefined cloud optical depth at 497.5 nm (COD), cloud base height (CBH) and cloud thickness ΔH_c. Here we deploy a more detailed 36-layer plane-parallel model to better resolve different cloud heights and types.

Represented values of COD, cloud base height (CBH) and cloud thickness ΔH_c are found by comparing the modeling results with the empirical model first proposed in [16],

$$\varepsilon_{\text{sky}} = \varepsilon_{\text{sky},c}(1 - a_1\,\text{CF}^{a_2}) + \text{a}_3\,\text{CF}^{a_4}\phi^{a_5} \tag{4.10}$$

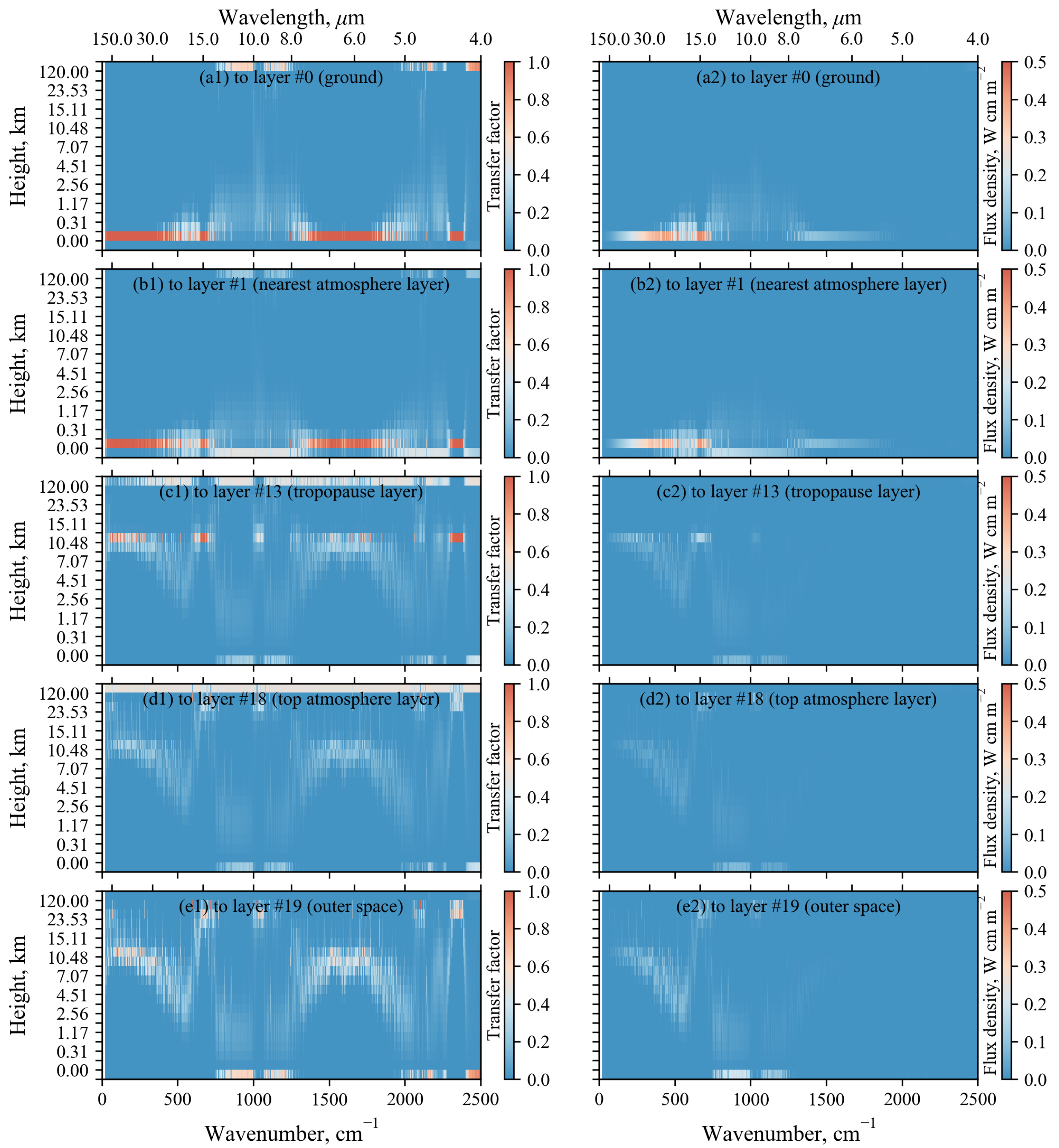

Figure 4.10: Vertical and spectral contribution of irradiation on selected layers: (a) ground layer, (b) nearest atmosphere layer, (c) tropopause layer, (d) top atmosphere layer and (e) outer space layer. Surface RH = 65% and $\text{AOD}_{497.5} = 0.1$.

where $\varepsilon_{\text{sky},c}$ is the empirical clear sky effective emissivity, CF is cloud fraction, ϕ is ambient relative humidity and a_1 to a_5 are coefficients regressed from data collected from seven meteorologically diverse SURFRAD (and other nearby weather) stations over the year 2013 [16]. For daytime periods, $a_1 = 0.96$, $a_2 = 1.2$, $a_3 = 0.49$, $a_4 = 1.09$ and $a_5 = 0.15$.

Figure 4.12 plots the effective sky emissivity with respect to p_w of overcast skies for different COD and cloud types. The empirical model for clear (CF = 0) and overcast (CF = 1) skies are also plotted for references. The three types of clouds shown in Fig. 4.12 are listed in Table 4.3. Comparisons of Fig. 4.12 (a)

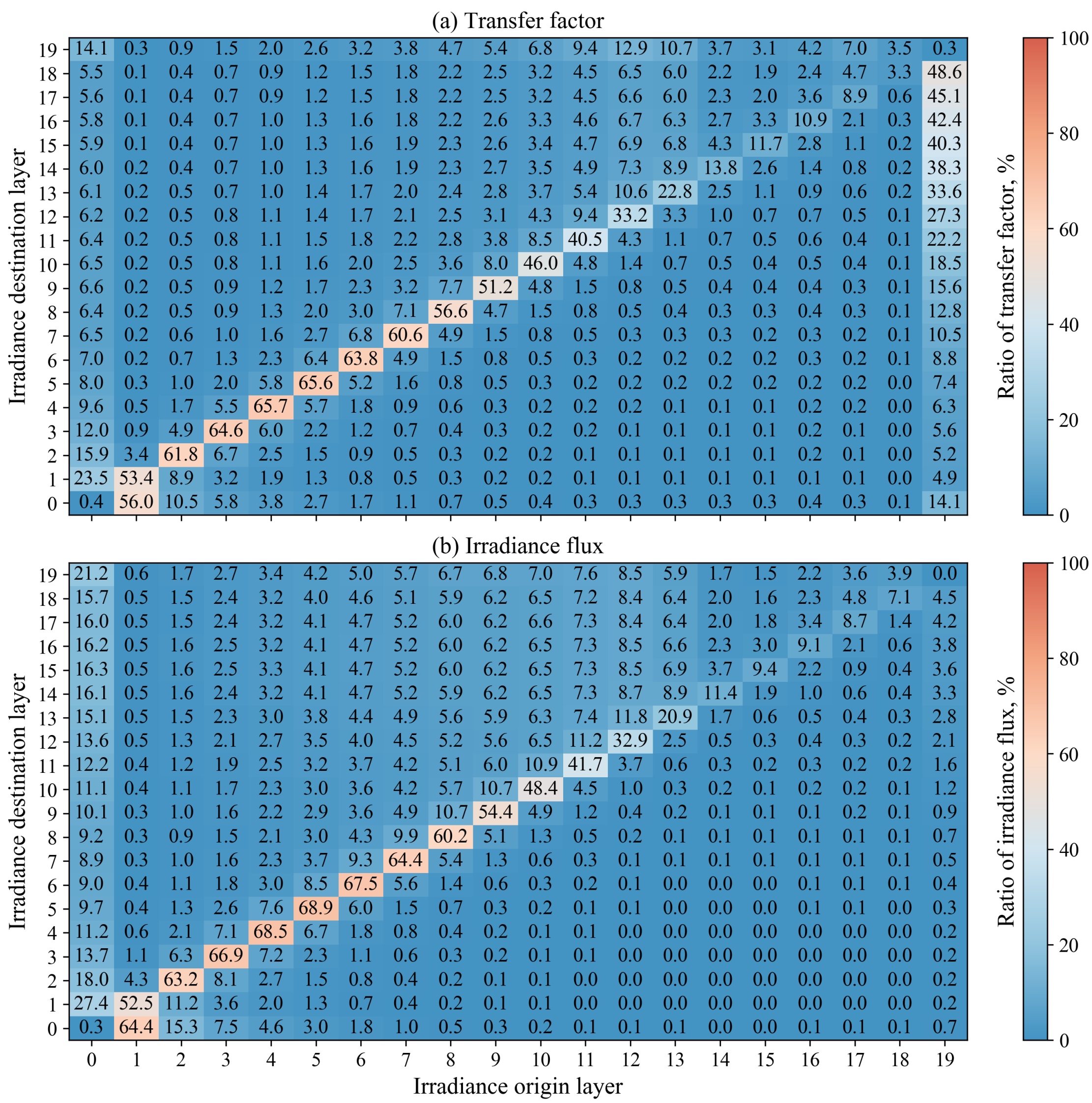

Figure 4.11: The broadband percentage contributions of the transfer factor (a) and irradiance flux (b) of each layer. Surface RH = 65% and $AOD_{497.5} = 0.1$. The total contributions in each row add to 100 (%).

to (c) indicate larger effective sky emissivity for lower clouds and larger COD. When COD is smaller than 0.1, the modeling results align with the clear sky empirical model (CF = 0). When COD is larger than 1.0, the modeling results increase slower with respect to p_w than when compared to the empirical model with CF = 1. Therefore, the real COD can be modeled as an increasing function of p_w.

Table 4.3: Types of clouds considered.

Type	CBH, km	ΔH_c, km	Reside in layers	Notes
I	0.18	1.62	4 to 10	low clouds
II	2.16	1.79	12 to 15	middle clouds
III	7.07	1.59	21 to 22	high clouds

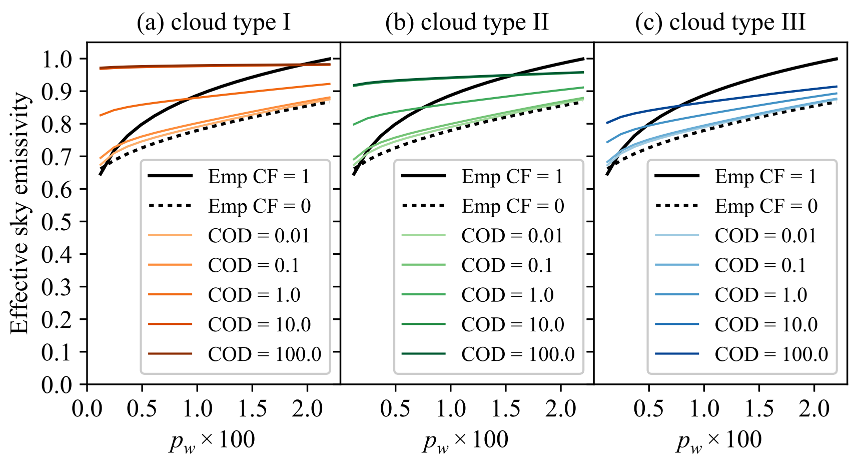

Figure 4.12: Effective sky emissivity of overcast skies for different COD and cloud types. The empirical model for clear and overcast skies is also plotted for comparison.

For partly cloudy skies, the effective sky emissivity calculated from the model is expressed as,

$$\varepsilon_{\text{sky}} = \varepsilon_{\text{sky},c}(1 - \text{CF}) + \varepsilon_{\text{sky,oc}}\text{CF} \tag{4.11}$$

where subscripts 'c' and 'oc' represents clear skies and overcast skies, respectively. Note that $\varepsilon_{\text{sky,oc}}$ is a function of p_w, COD and cloud types (Fig. 4.12).

For given ambient p_w, cloud fraction, and cloud type, a 'fitted COD' could be found that results best agreement between Eq. 4.11 and Eq. 4.10. The fitted COD (COD_f) is plotted in the top row of Fig. 4.13. The COD_f is increasing with increased p_w but only weakly dependent on CF. Therefore, a represented COD for each p_w and cloud type is found by averaging COD_f over all CF. Then the represented COD (COD_r) is regressed as a function of p_w for all cloud types,

$$\log_{10}(\text{COD}_r) = d_1 + d_2 \tanh(d_3\, p_w) \tag{4.12}$$

The regression coefficients d_1 to d_3 are tabulated in Table 4.4. The effective sky emissivity calculated from Eq. 4.11 (with the use of COD_r to calculate $\varepsilon_{\text{sky,oc}}$) minus that calculated from (4.10) are plotted in the middle row of Fig. 4.13. The spectral model tends to overestimate the effective sky emissivity when p_w ranges from 0.01 to 0.015 and cloud fraction is greater than 0.5. When p_w is greater than 0.015, the spectral model tends to underestimate the effective sky emissivity and the degree of underestimation increases with cloud base height (i.e. cloud type). The averaged absolute difference over all CF are plotted in the bottom row of Fig. 4.13, from which we concluded that when $0.01 < p_w < 0.015$, the representative cloud characteristic is the type II cloud with corresponding COD_r, which has the smallest difference. For all other p_w values, the representative cloud characteristic is type I cloud with corresponding COD_r.

Using the representative cloud characteristic in the spectral model, the modeled and empirical effective sky emissivities are compared in Fig. 4.14. The difference is shown on the bottom surface, indicating that the absolute error of all considered CF and p_w are smaller than 0.05, which corresponds to 21.23 W m^{-2} ($0.05\,\sigma T_a^4$ with T_a =294.2 K). The RMSE of the empirical model is 21.18 W m^{-2} when evaluated against the SURFRAD measured downwelling longwave irradiance at the surface.Thus, the proposed representative cloud characteristics fit the measurements accurately.

Table 4.4: Fitting coefficients of represented COD for different cloud types in Table 4.3.

Type	d_1	d_2	d_3	R^2
I	-1.610	4.110	63.440	0.983
II	-1.760	3.980	90.710	0.979
III	-2.170	4.210	188.850	0.964

4.5 Radiative cooling power of passive cooling materials

Passive radiative coolers are designed to have low absorptance in the solar shortwave spectral and high emittance in the infrared longwave spectral [18, 20], so that it can reject heat through the 'atmospheric window' (band (b4)) even under direct sunlight. The broadband net cooling power $q_{\text{cool}}(T)$ of a radiative

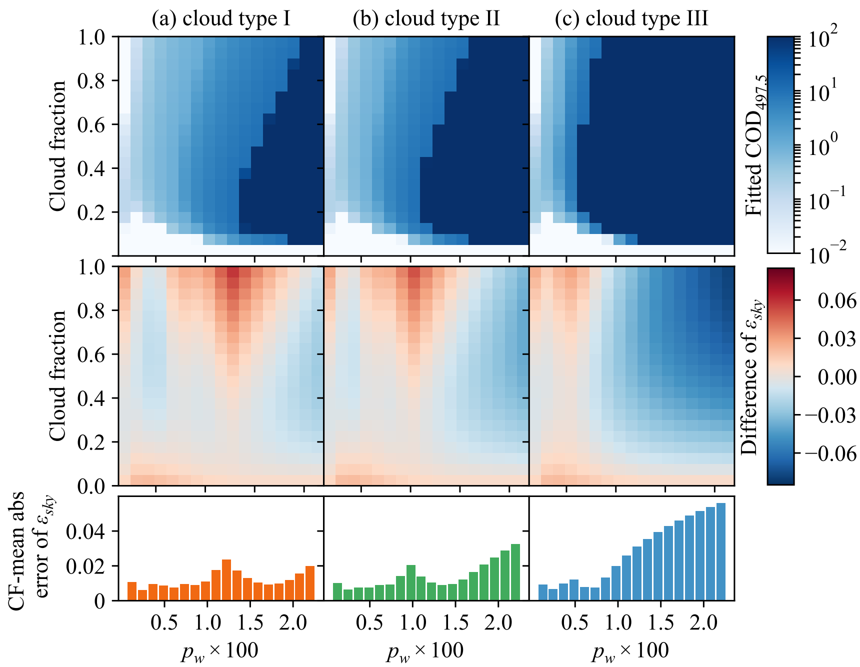

Figure 4.13: Top subplots show fitted COD with respect to CF and p_w for all three cloud types. Middle subplots show the difference between the effective sky emissivity calculated with Eq. 4.11 using the represented COD$_r$ (4.10). Bottom subplots show the difference for all values of CF.

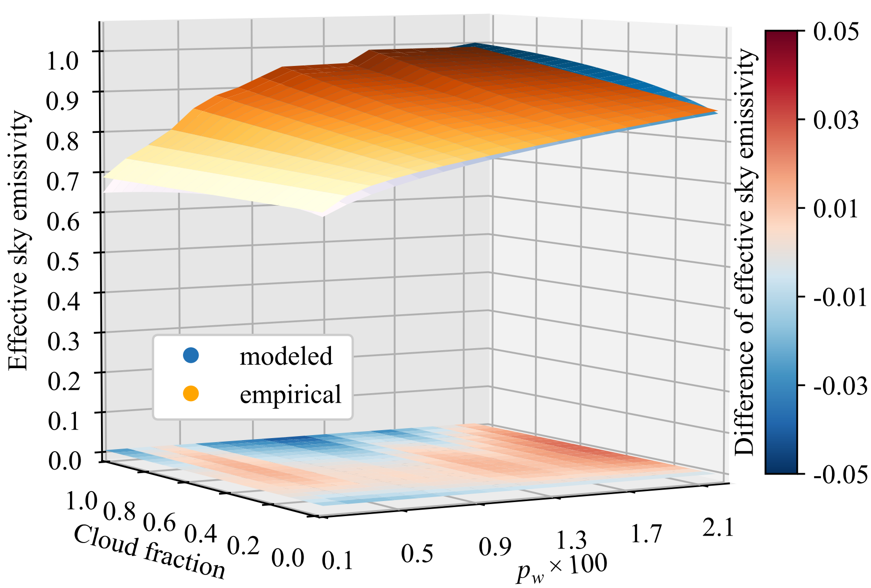

Figure 4.14: Comparison between empirical and spectral model results for different conditions. The total deviation is depicted on the lower surface.

cooler of surface temperature T is [18],

$$q_{\mathrm{cool}}(T) = \bar{\varepsilon}_{lw}\left[\sigma T^4 - J_{\mathrm{sky}}(T_a, \phi, \mathrm{CF})\right] - \bar{\varepsilon}_{sw} q_{sw} - h_c(T_a - T) \tag{4.13}$$

where $\bar{\varepsilon}_{lw}$ (or $\bar{\varepsilon}_{sw}$) are the spectral averaged longwave (or shortwave) emittance/absorptance of the cooler, $J_{\mathrm{sky}}(T_a, \phi, \mathrm{CF})$ (W m^{-2}) is the sky radiation calculated using the methods proposed in the main text, q_{sw} (W m^{-2}) is solar irradiance, h_c (W m^{-2} K^{-1}) is the convective heat transfer coefficient and T_a (K) is the ambient temperature.

When $T = T_a$, $q_{\mathrm{cool}}(T = T_a)$ defines the cooling power at the ambient temperature [18],

$$q_{\mathrm{cool}}(T_a) = \bar{\varepsilon}_{lw} \sigma T_a^4 \left[1 - \varepsilon_{\mathrm{sky}}(T_a, \phi, \mathrm{CF})\right] - \bar{\varepsilon}_{sw} q_{sw} \tag{4.14}$$

where the broadband cooling power decreases with increased effective sky emissivity.

In the absence of net power outflow, a radiative cooler's temperature should reach a steady state temperature T_{ss} [18] and this temperature needs to be below T_a to enable cooling. The steady state temperature is solved from,

$$\bar{\varepsilon}_{lw}\left[\sigma T_{ss}^4 - J_{\mathrm{sky}}(T_a, \phi, \mathrm{CF})\right] = \bar{\varepsilon}_{sw} q_{sw} + h_c(T_a - T_{ss}). \tag{4.15}$$

The spectral longwave cooling power at ambient temperature $q_{\mathrm{cool},lw}(\nu, T_a)$ is,

$$E_{\mathrm{cool,lw}}(\nu, T_a) = \varepsilon_{lw}(\nu) \pi I_b(T_a, \nu)\left[1 - \varepsilon_{\mathrm{sky}}(\nu, T_a, \phi, \mathrm{CF})\right]. \tag{4.16}$$

The passive cooling material proposed in [20] has $\bar{\varepsilon}_{lw} = 0.93$ and $\bar{\varepsilon}_{sw} = 0.04$. For calculation purposes we assume the nominal values of $q_{sw} = 890$ W/m^2 during the day, $q_{sw} = 0$ at night and $h_c = 6.9$ W/m K [18], with the effective sky emissivity calculated using the coefficients presented in Table 4.1. The steady state temperature T_{ss} is then calculated for different ambient temperature T_a and relative humidity ϕ.

4.5.1 Under clear skies

Figure 4.15 plots the temperature difference $(T_a - T_{ss})$ for four scenarios: daytime with or without convection and nighttime with or without convection. The temperature difference $(T_a - T_{ss})$ decreases with increased $p_w(T_a, \phi)$ because of increased effective sky emissivity due to higher water vapor concentration in

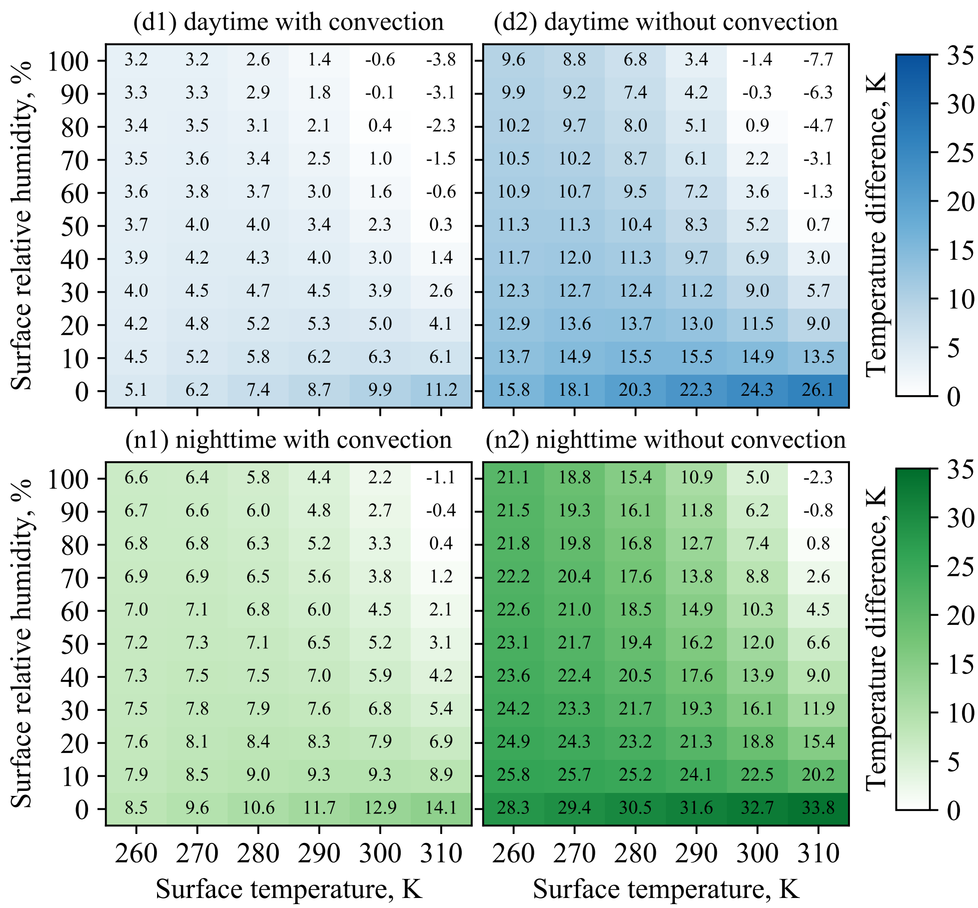

Figure 4.15: The temperature difference ($T_a - T_{ss}$) of the passive cooling material under different ambient meteorological conditions. (d1) is for daytime when q_{sw} = 890 W m^{-2} and h_c = 6.9 W m^{-2} K^{-1}. (d2) is for daytime when $h_c = 0$. (n1) is for nighttime when $q_{sw} = 0$ and h_c=6.9 W m^{-2} K^{-1}. (n2) is for nighttime $h_c = 0$.

the atmosphere. Both the convective heat gain from ambient air and the absorption of solar radiation reduce ($T_a - T_{ss}$), which in turn reduce the cooling efficiency of the passive coolers.

With the correlations for spectral atmospheric emissivity, it is possible to estimate the cooling power of different materials used for passive cooling that take advantage of the atmospheric window. The cooling power $q_{\text{cool}}(T_a)$ of the photonic material described in [20] for different ambient meteorological conditions is shown in Fig.4.16. This material in particular has an averaged solar absorptance of 0.04 and longwave absorptance/emittance of 0.93 [20]. For the purposes of calculation, the daytime solar irradiance is set to 890 W/m^2 [18], and the broadband sky emissivity is calculated using Eq. 4.5 with coefficients tabulated in Table 4.2. Figure 4.16 shows the cooling power during daytime periods. The nighttime cooling power for the same conditions is $0.04 \times 890 = 35.6$W/m^2 more, because of zero absorption of solar irradiance during the night.

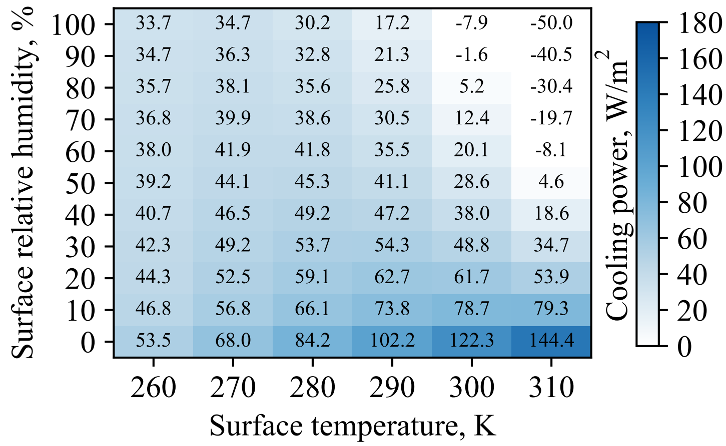

Figure 4.16: The cooling power of the passive cooling material under different ambient meteorological conditions during daytime when $F_{\text{sun}} = 890\ \text{W m}^{-2}$.

The cooling power is high for hot and dry conditions, and substantially lower for mild temperatures and high humidities.

Figure 4.17 plots the emitted longwave radiation and cooling power of the material under clear skies when $T_a = 294.2$ K. The cooling is mostly in bands (b2) and (b4) and decreases with increased ambient relative humidity (equivelent to atmospheric column water vapor concentration).

As indicated by the spectral analysis presented above, only bands (b2) and (b4) contribute to the cooling power. By applying the regressed coefficients for bands (b2) and (b4) tabulated in Table 4.2 the cooling power per band is plotted in Fig. 4.18 (b) for ambient $T_a = 294.2$ K. The longwave cooling power is mostly from band (b4) and it decreases with increased ambient relative humidity (proportional to the column of water vapor content in the atmosphere) because atmospheric H_2O 'blocks' the atmospheric window. Figure 4.18 (a) is a plot of the cooling power by band calculated by line-by-line integration of the cooling power in each band. The difference in values between Fig.4.18 (a) and (b) is less than 6%, indicating that the coefficients proposed in Table 4.1 can be used to estimate sky emissivity in each band with sufficient accuracy for thermal design applications.

4.5.2 Under cloudy skies

Using the spectrally modeled broadband sky emissivity shown in Fig. 4.14, the longwave cooling power of the material proposed in [20] for $T_a = 294.2$ K is plotted in Fig. 4.19. The cooling power decreases

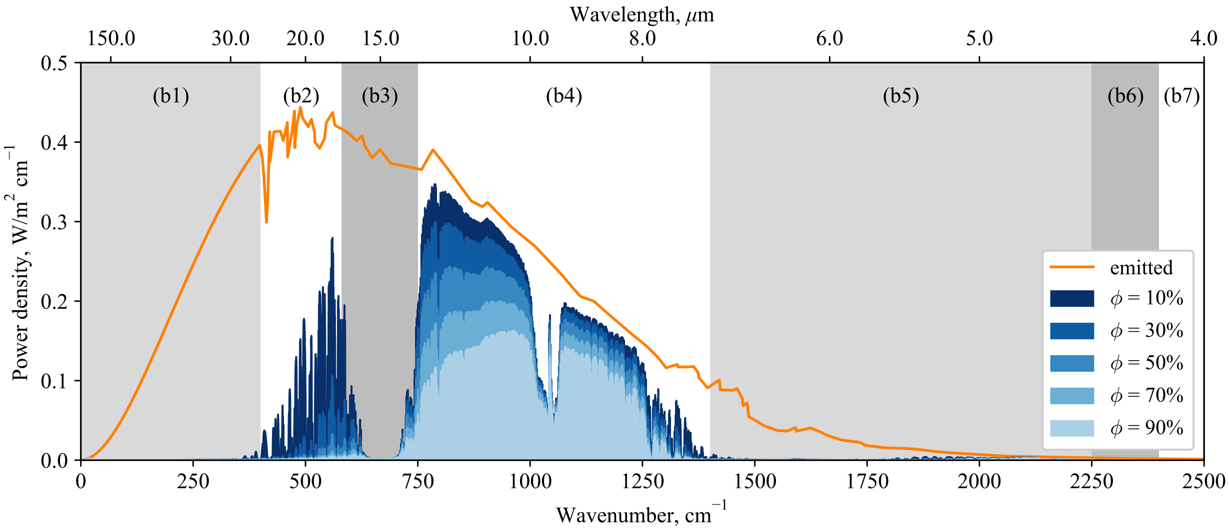

Figure 4.17: Spectral longwave cooling power $q_{\text{cool}}(\nu, T_a)$ for ambient T_a = 294.2 K under clear skies.

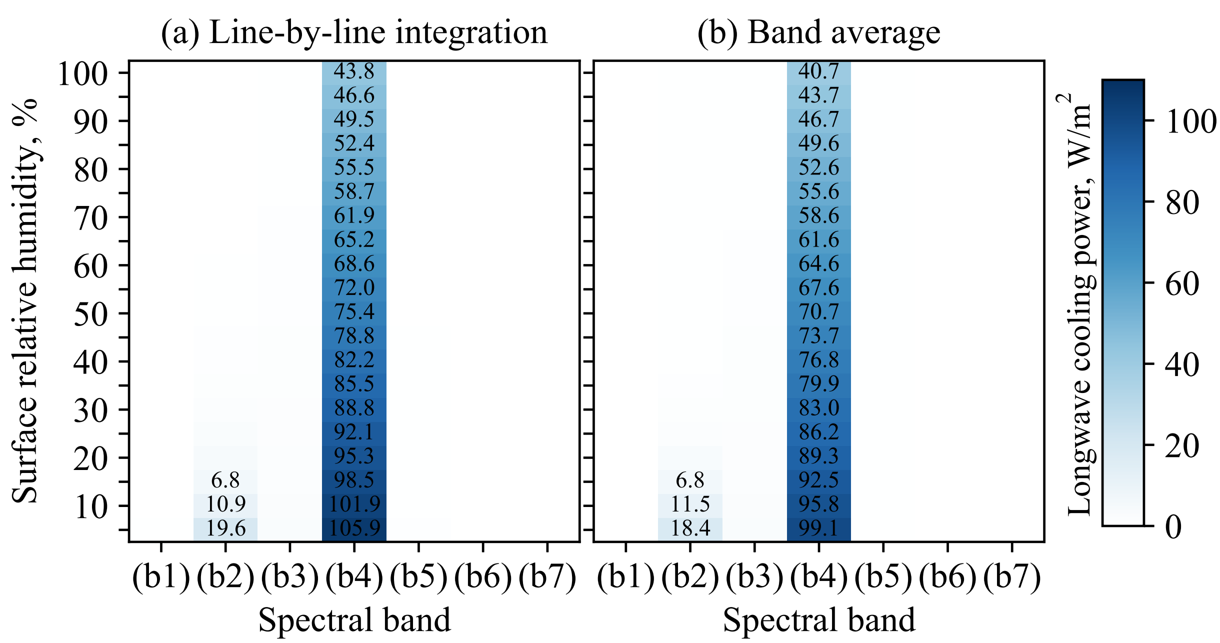

Figure 4.18: Longwave cooling power by bands under clear skies for different ambient relative humidity with $T_a = 294.2$K. (a) line-by-line integration of $\varepsilon_{\text{sky}}(\nu)$ for each band; (b) band-averaged ε_{sky} calculated using the coefficients proposed in Table 4.2 with band-averaged emmissivities for the passive cooler.

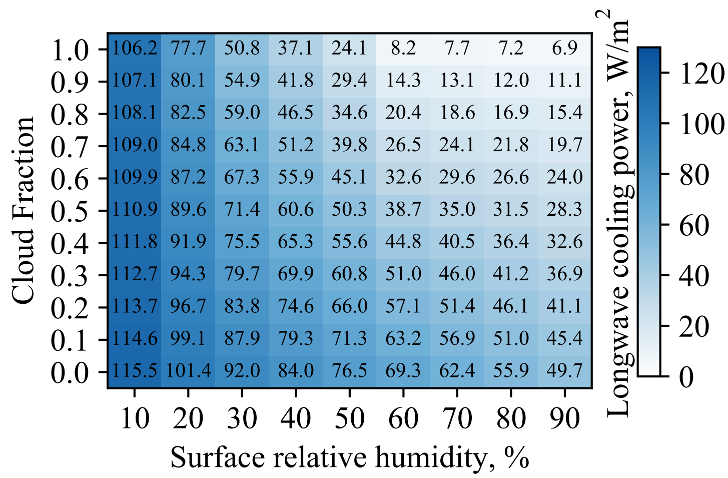

Figure 4.19: The cooling power of the passive cooling material under different surface and cloud conditions when T_a = 294.2 K.

when more water vapor and/or clouds are present in the atmosphere, because clouds also ‘block’ the atmospheric window as can be seen in Fig. 4.20.

4.6 Acknowledgments

This Chapter, in full, is a combination of three publications: M. Li, Z. Liao, and C. F. M. Coimbra (2018) “Spectral model for clear sky atmospheric longwave radiation” *Journal of Quantitative Spectroscopy and Radiative Transfer*, 209, 196-211; M. Li, Z. Liao and C. F. M. Coimbra (2018) “An Efficient Spectral Model for Evaluating Spectral and Spatial Distributions of Clear Sky Atmospheric Longwave Radiation,” accepted for the *16th International Heat Transfer Conference (IHTC-16)*; M. Li, and C. F. M. Coimbra (2018) “On the Effective Spectral Emissivity of the Sky,” submitted to *Proceedings of the National Academy of Sciences of the United States of America*. The dissertation author is the first author of these manuscripts.

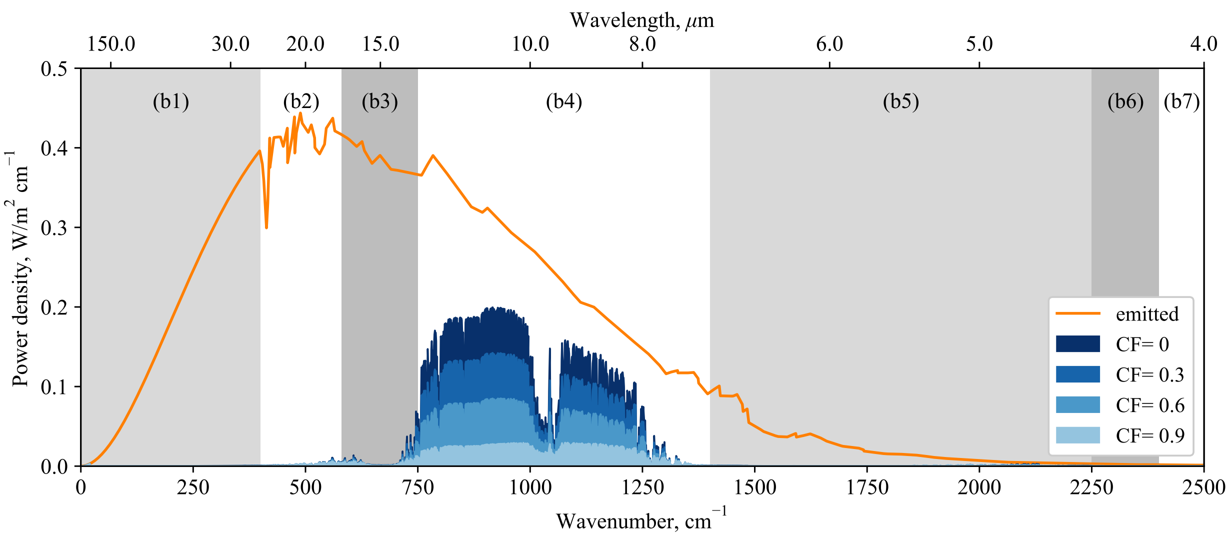

Figure 4.20: Spectral longwave cooling power $q_{\text{cool}}(\nu, T_a)$ for ambient T_a = 294.2 K and ϕ = 70% under cloudy skies.

Chapter 5

Spectral modeling of solar shortwave radiative transfer in the atmosphere

5.1 The radiative models

For longwave radiative transfer in the atmosphere (wavenumber ranges from 0 to 2500 cm^{-1}), a two - flux spectral multilayer model was developed by the authors [5] to calculate the downwelling and upwelling flux densities in the atmosphere at a spectral resolution of 0.01 cm^{-1}. The two - flux model is sufficiently accurate for longwave radiative transfer because the radiation sources (emission) from the system (atmosphere layers and the Earth surface) are diffused. However, for shortwave transfer (wavenumber ranges from 2500 to 40000 cm^{-1}), the radiation source (solar irradiance) is highly directional so a two - flux model would be inappropriate. Therefore, a Monte Carlo radiative model is developed to calculate the shortwave radiative transfer in the atmosphere - Earth system.

The atmosphere here is again modeled as N plane parallel layers extending from the ground to the top of atmosphere (120 km above the ground). The layers are divided using a pressure coordinates as detailed in Ref. [5]. The temperature and atmospheric gas profiles are assumed to follow Air Force Geophysics Lab (AFGL) midlatitude summer profiles [69], with gas profiles corrected for current surface concentrations [5]. The spectral absorption coefficients of gas molecules are retrieved from HITRAN database [82]. The continuum absorption coefficients of water vapor and carbon dioxide are calcualted using MT_CKD continuum model [61]. In the longwave spectrum, the gas molecules are treated as non-scattering because the particle size is much smaller than the wavelength [12]. The absorption, scattering coefficients and asymmetry parameters of aerosols and clouds are calculated via Mie theory by assuming proper size distributions [5, 88].

In the shortwave spectrum, the scattering of gas molecules are modeled as Rayleigh scattering [12]. Ozone and oxygen continuum absorption are added because it is more significant in the shortwave than in the longwave spectrum. The following sections present the methodologies of calculating scattering coefficients of molecules, continuum absorption coefficients of ozone and oxygen and the Monte Carlo method.

5.1.1 Monochromatic extinction coefficients

The Rayleigh scattering coefficient is calculated as [6],

$$\kappa_{s,\text{gas}} = \frac{24\nu^4 N\pi^3 (m_s^2 - 1)^2 F_k}{N_s^2 (m_s^2 + 2)^2} \tag{5.1}$$

where ν (cm^{-1}) is the wavenumber; N (cm^{-3}) and N_s (2.54743×10^{19} cm^{-3}) are the molecular number densities of considered and standard air ($P = 1.013 \times 10^5$Pa, T = 288.15K with 300 ppm CO_2), respectively; m_s is the refractive index for standard air at wavenumber ν; and F_k is King corrector factor defined as $(6+3\rho_n)/(6-7\rho_n)$, where ρ_n is the depolarization factor at ν that accounts for the anisotropy of the air molecules [6]. Figure 5.1 plots the King correction factor with respect to wavenumber, with data retrieved from Ref. [6].

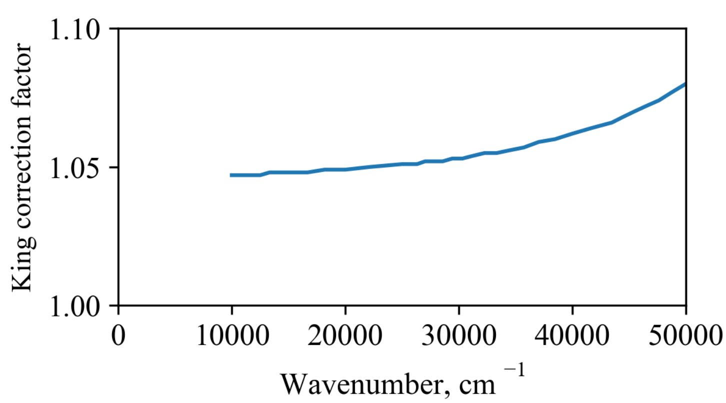

Figure 5.1: The King correction factor with respect to wavenumber [6].

The refractive index of standard air in the shortwave spectrum is calculated as [89],

$$(m_s - 1) \times 10^8 = \frac{5791817}{238.0185 - (\nu/10^4)^2} + \frac{167909}{57.362 - (\nu/10^4)^2} \tag{5.2}$$

The molecular number density of considered atmosphere layer is calculated from Ideal Gas Law,

$$N = \frac{P N_A}{R_u T \times 10^6} \tag{5.3}$$

where P (Pa) is the pressure; N_A (6.022×10^{23} mol^{-1}) is the Avogadro constant; R_u (8.314 J mol^{-1} K^{-1}) is the universal gas constant; and T (K) is the temperature. The factor 10^6 is used to convert the units of number density to cm^{-3}.

The continuum absorption coefficients of ozone and oxygen are calculated using the MT_CKD continuum model [61]. Figure 5.2 plots the absorption and scattering coefficients of atmospheric gases and aerosols. Ozone absorption dominants the UV spectrum while water vapor absorption dominants the near infrared spectrum. In the visible spectrum, scattering by gas molecules and absorption and scattering of aerosols dominant.

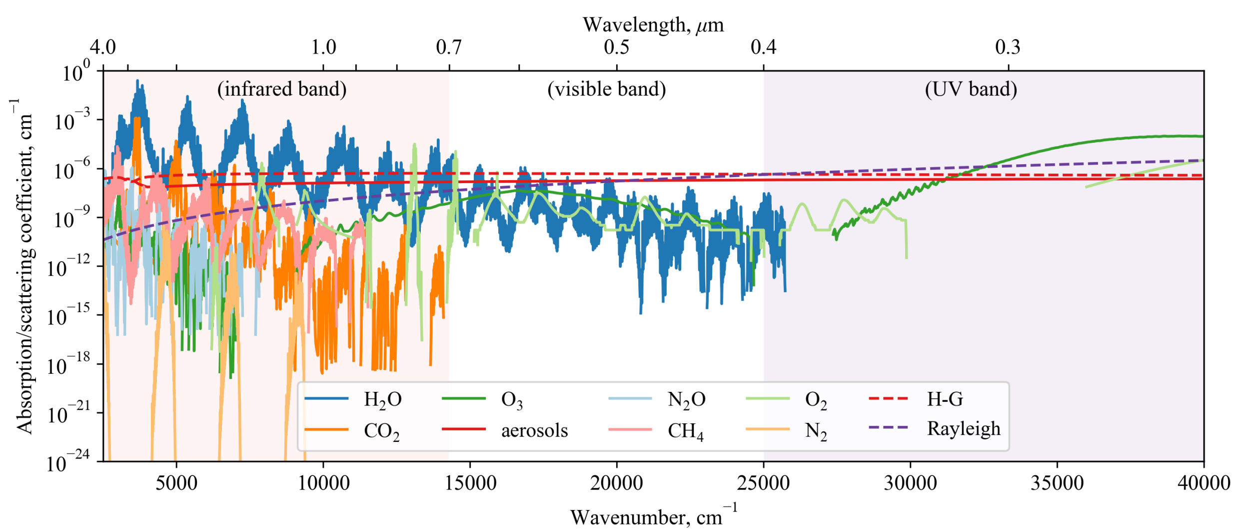

Figure 5.2: Spectral absorption (solid lines) and scattering (dash lines) coefficients for main atmospheric constituents at the lowest layer of the troposphere.

5.1.2 Monte Carlo Method

The statistical Monte Carlo (MC) method is used to simulate the transport of photons (thus energy) in the Earth - atmosphere system. The monochromatic upwelling and downwelling flux densities are calculated by tracing the paths of a large number of photons of that wavenumber. The energy carried by each photon bundle is,

$$e_\nu = \frac{E_{0,\nu}\cos\theta_z}{N_b} \tag{5.4}$$

where $E_{0,\nu}$ is the monochromatic extraterrestrial solar flux density at wavenumber ν; θ_z is the solar zenith angle and N_b is the number of photon bundles used for wavenumber ν. The extraterrestrial solar flux density used is the 2000 ASTM Standard Extraterrestrial Spectrum [22].

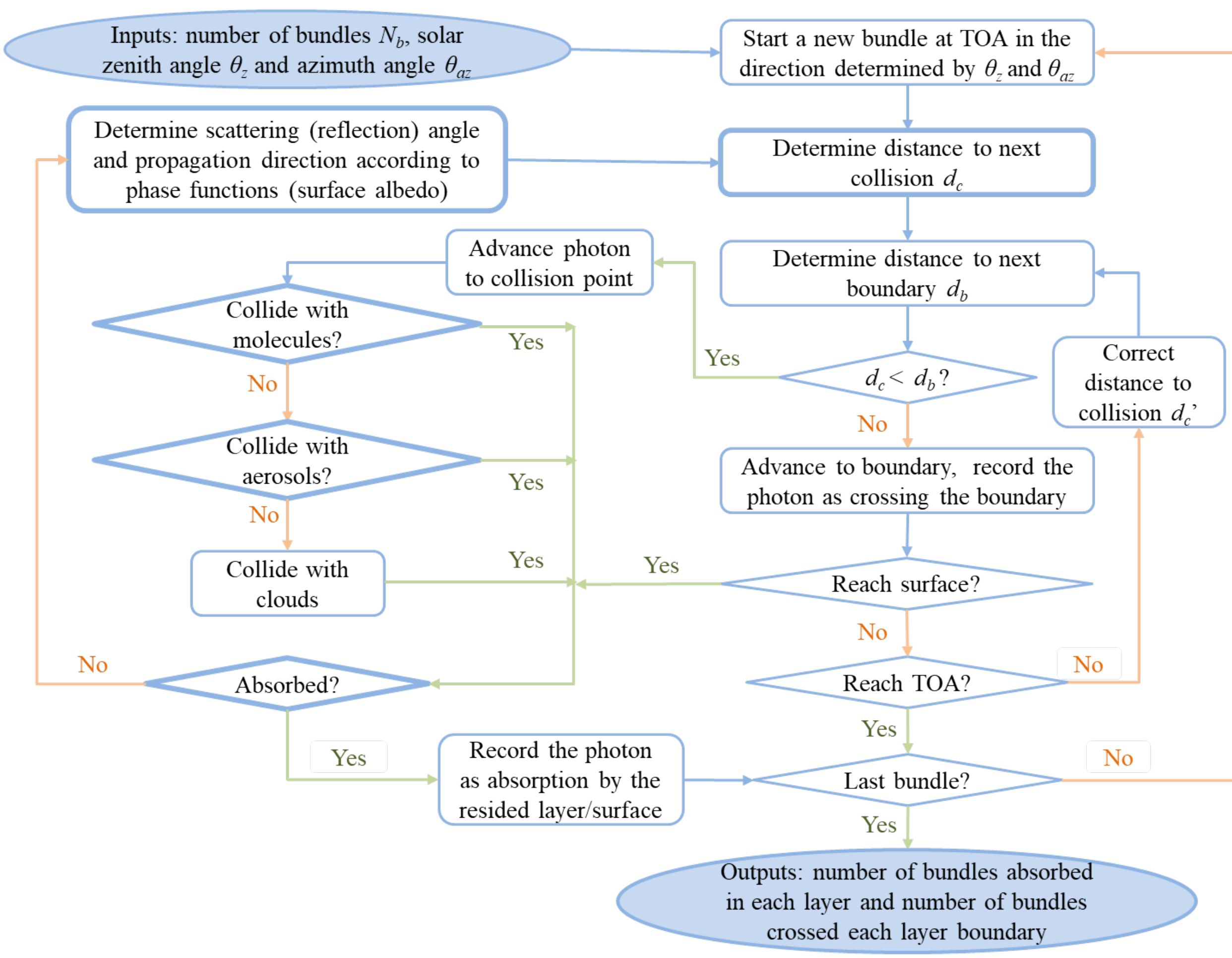

Figure 5.3: Algorithm flowchart for the MC radiative transfer model used in this work. Processes in the rectangles with thick lines use random numbers.

Figure 5.3 shows the flowchart for the MC radiative transfer model, where processes in the rectangles with thick lines use random numbers. Photons enter the Earth - atmosphere system from the top of atmosphere (TOA) in the direction of (r_x, r_y, r_z), where,

$$r_x = \sin\theta_z \cos\theta_{az}, \quad r_y = \sin\theta_z \sin\theta_{az}, \quad r_z = \cos\theta_z. \tag{5.5}$$

Once entering the atmosphere, photons may collide with atmospheric particles (molecules, aerosols and cloud droplets) and then either being absorbed or scattered. A new photon will enter the system after the previous photon ends its lifetime. The total number of photons is predefined to balance accuracy and computational time (see section 5.2.1 for analysis).

Photon traveling

The probability that a photon travels an optical depth t without collision is:

$$p(t)dt = e^{-t}dt. \tag{5.6}$$

Then the optical depth a photon travels before next collision t_0 is sampled by inverting the accumulative probability function,

$$\begin{aligned} \xi_{t0} &= \int_0^{t_0} e^{-t}dt = 1 - e^{-t_0}, \\ t_0 &= -\ln(1-\xi_{t0}) = -\ln\xi_{t0}. \end{aligned} \tag{5.7}$$

where ξ_{t0} is a random number uniformly sampled from 0 to 1, so do all ξ in the following sections. The photon traveling distance to next collision d_c (m) is then,

$$d_c = \frac{t_0}{\kappa_e} = -\frac{\ln\xi_{t0}}{\kappa_e} \tag{5.8}$$

where κ_e (cm^{-1}) is the monochromatic extinction coefficient of the atmospheric layer within which the photon is traveling.

The distance to the nearest boundary d_b (m) in the direction of photon propagation is then calculated. For a plane-parallel geometry,

$$d_b = \left|\frac{z_b - z}{r_z}\right| \tag{5.9}$$

where z_b (m) is the location of nearest boundary in photon traveling direction and z is the current location of the photon. If $d_c < d_b$, the collision happens in the current layer. Otherwise, the photon advances to the boundary with its coordinates updated,

$$x' = x + r_x d_b \qquad y' = y + r_y d_b \qquad z' = z + r_z d_b. \tag{5.10}$$

When a photon reaches a boundary, its energy is recorded as crossing the boundary, thus contributes to the upwelling or downwelling fluxes. If the boundary is ground surface, the photon then interacts with the surface, being either absorbed or reflected back to the atmosphere. If the boundary is TOA, the photon energy is recorded as outgoing energy. If the boundary is internal, the photon continue propagates into the next layer. The distance to next collision d_c' and to next boundary d_b are updated according to the optical properties of the new layer,

$$d_c' = \frac{\kappa_\nu}{\kappa_\nu'}(d_c - d_b), \quad d_b' = \left|\frac{z_b' - z_b}{r_z}\right| \tag{5.11}$$

where κ_ν' (cm^{-1}) is the extinction coefficient in the just-entered layer. The d_c' and d_b' are then compared to determine whether the photon will interact within the layer or continue travel to the next layer. This process continues until the photon collides with particles or exits the external boundary [90].

Photon interacts with particles

When the photon collides with particles, the probability of colliding with molecules, aerosols and clouds are determined by the ratio of extinction coefficients,

$$\begin{aligned} \text{collide with gas molecules:} \quad & \xi_h \le \frac{\kappa_{e,\text{gas}}}{\kappa_e}, \\ \text{collide with aerosols:} \quad & \frac{\kappa_{e,\text{gas}}}{\kappa_e} < \xi_h \le \frac{\kappa_{e,\text{gas}} + \kappa_{e,\text{aer}}}{\kappa_e}, \\ \text{collide with cloud droplets:} \quad & \xi_h > \frac{\kappa_{e,\text{gas}} + \kappa_{e,\text{aer}}}{\kappa_e}, \end{aligned} \tag{5.12}$$

where $\kappa_{e,\text{gas}}$ (cm^{-1}) and $\kappa_{e,\text{aer}}$ (cm^{-1}) are extinction coefficients of gases and aerosols, respectively.

Once collide with a particle, the probability of scattering is determined by the single albedo $\tilde{\rho}$ of the particle,

$$\begin{aligned} &\text{being scattered:} \quad \xi_s \le \tilde{\rho}_i = \frac{\kappa_{s,i}}{\kappa_{e,i}}, \\ &\text{being absorbed:} \quad \xi_s > \tilde{\rho}_i, \end{aligned} \tag{5.13}$$

where $\kappa_{s,i}$ (cm^{-1}) and $\kappa_{e,i}$ (cm^{-1}) are scattering and extinction coefficients of particle type i (molecules, aerosols, droplets), respectively. If absorbed, the photon's life time ends, and its energy is converted to the thermal field of the layer. If scattered, the traveling direction of the photon is changed according to the scattering phase functions,

$$\begin{aligned} \text{Rayleigh scattering:} \quad & P(\cos\Theta) = \frac{3}{4}(1+\cos^2\Theta), \\ \text{Mie scattering:} \quad & P(\cos\Theta) = \frac{1-g^2}{2(1+g^2-2g\cos\Theta)^{3/2}}, \end{aligned} \tag{5.14}$$

where Θ (rad) is the scattering angle and g is the scattering asymmetry parameter of the particles. For Mie scattering, the Henyey-Greenstein (H-G) scattering phase function is used [91]. The scattering angle is sampled by inverting the accumulative phase function,

$$\begin{aligned} &\xi_\mu = \int_{-1}^{\mu} P(\mu')d\mu' \\ &\cos\Theta = \sqrt[3]{4\xi_\mu - 2 + \sqrt{(4\xi_\mu-2)^2+1}} + \sqrt[3]{4\xi_\mu - 2 - \sqrt{(4\xi_\mu-2)^2+1}}, \quad \text{Rayleigh scattering} \\ &\cos\Theta = \frac{1}{2g}\left(1+g^2-\frac{1-g^2}{1-g+2g\xi_\mu}\right), \quad \text{Mie scattering} \end{aligned} \tag{5.15}$$

where $\mu = \cos\Theta$, and the sampling scheme of Rayleigh and H-G phase functions are obtained from [92] and [91], respectively. With the sampled scattering zenith angle Θ and azimuth angle $\Phi = 2\pi\xi_\phi$, the photon traveling direction (r'_x, r'_y, r'_z) after the scattering is [93],

$$\begin{aligned} r'_x &= r_x\cos\Theta - \frac{\sin\Theta}{\sqrt{1-r_z^2}}(r_x r_z\cos\Phi + r_y\sin\Phi), \\ r'_y &= r_y\cos\Theta - \frac{\sin\Theta}{\sqrt{1-r_z^2}}(r_y r_z\cos\Phi - r_x\sin\Phi), \\ r'_z &= r_z\cos\Theta + \sqrt{1-r_z^2}\sin\Theta\cos\Phi, \end{aligned} \tag{5.16}$$

The photon is then traveling in the new direction (r'_x, r'_y, r'_z) to next collision point. The procedure repeats until the photon's lifetime ends (being absorbed or escaping to outer space).

Photon interacts with surface

When a photon reaches the ground surface, it will be either absorbed by the surface or reflected back to the atmosphere. For real surfaces (grass, snow, dessert, barren and etc.) and photovoltaic panels, the reflection is considered to be diffuse. For heliostats in concentrated solar farms, the reflection is considered to be specular. The traveling direction of photon after the surface reflection is sampled as,

$$\begin{aligned} \text{diffuse reflection:} \quad & r_z' = \sqrt{\xi_z} \\ \text{specular reflection:} \quad & r_z' = -r_z \end{aligned} \tag{5.17}$$

The reflected photon continues to travel in the atmosphere until the end of its lifetime.

5.2 Validation of the radiative model

5.2.1 Grid convergence

The accuracy of MC radiative transfer model increases with increased number of plane parallel layers N, number of spectral grid N_ν and number of photon bundles N_b. However, the computational cost increases linearly with N_ν and N_b and near linearly with N. To balance the accuracy and computational cost, a grid convergence is performed to find the minimum $NN_\nu N_b$ that result in errors within ± 1 W m^{-2} for broadband surface global horizontal irradiance (GHI), surface direct normal irradiance (DNI), TOA upwelling flux and surface upwelling flux. Figure 5.4 presents the results of grid convergence test for AFGL mid-latitude summer cloud-free atmosphere, solar zenith angle of 30°, surface relative humidity of 70% and aerosol optical depth at 497.5 nm (AOD) of 0.1. As shown in Fig.5.4, a 54 layer atmosphere, with spectral resolution of 3 cm^{-1}, and 1000 photon bundles for each wavenumber can achieve the desired grid convergence while preserve minimum $NN_\nu N_b$. The model is coded in Cython to improve the computational speed. A single run of the model takes approximately 5 minutes on and Intel Xeon E5-2640 machine with 9 cores parallel.

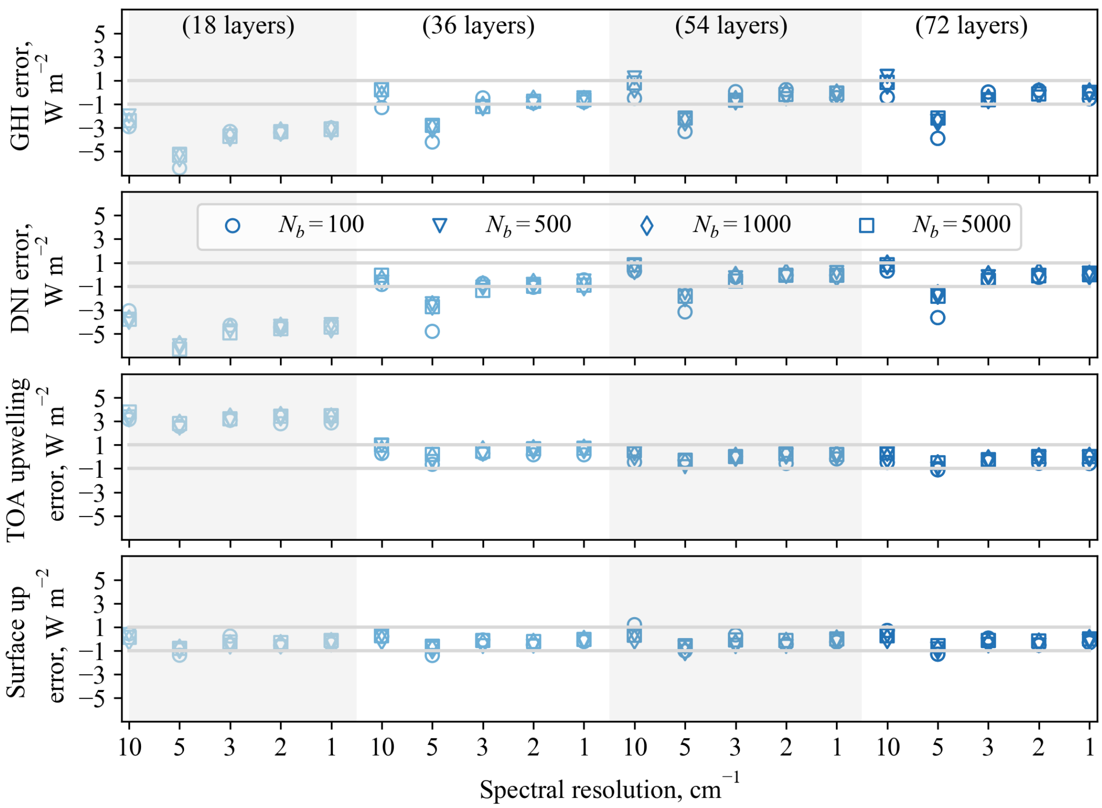

Figure 5.4: Monte Carlo simulation grid convergence test.

5.2.2 Comparison with measurements and other models

The proposed MC radiative model is then validated against shortwave results from CHARTS radiative codes for six CIRC cases [7], with a spectral resolution of 3 cm^{-1}. Cases 1 to 4 are cloud free, Case 6 is cloudy sky with thick overcast liquid cloud and Case 7 is cloudy sky with moderately thin overcast liquid cloud. The MC model adopts the inputs provided by the CIRC program: number of vertical layers, vertical pressure, temperature and gas profiles, aerosol profiles and optical properties, cloud optical properties, solar zenith angle, spectral surface albedo and extraterrestrial solar irradiance. The broadband flux comparisons are presented in Table 5.1, showing that the results from the MC model are within 4% of downwelling flux and 9% of upwelling flux when compared with measurements and are of comparable accuracy of the CHARTS model. Spectral comparison between the MC model and CHARTS model are shown in Fig. 5.5. The spectral variation of the flux densities are comparable with absolute difference lower than 20 $\mathrm{mW\,cm\,m^{-2}}$ for all wavenumbers, for downwelling and upwelling flux densities, and for clear and overcast skies. Therefore, the developed MC model is valid to perform the analysis in the next Chapter.

5.3 Acknowledgments

This Chapter, in full, is in preparation as a manuscript for publication with my co-author and Ph.D. adviser C. F. M Coimbra at UC San Diego. The dissertation author is also the first author of these papers.

Table 5.1: Comparison of proposed Monte Carlo model with measurements and SMARTS model.

	Surface GHI, W m^{-2}	Surface DNI, W m^{-2}	TOA up, W m^{-2}	Surface GHI error, %	Surface DNI error, %	TOA up error, %
Case 1						
Measurements [7]	705.9	636.5	169.8			
CHARTS [7]	701.2	633.5	175.0	-0.67	-0.47	3.06
Monte Carlo model	703.7	636.5	175.4	-0.31	0.00	3.30
Case 2						
Measurements [7]	345.4	252.9	127.8			
CHARTS [7]	348.0	253.8	117.1	0.75	0.36	-8.37
Monte Carlo model	347.6	255.0	116.9	0.65	0.82	-8.52
Case 3						
Measurements [7]	772.5	674.5	159.6			
CHARTS [7]	773.1	675.1	173.6	0.08	0.09	8.77
Monte Carlo model	775.7	678.4	173.8	0.41	0.57	8.92
Case 4						
Measurements [7]	638.9	482.5	425.8			
CHARTS [7]	642.8	487.6	422.9	0.61	1.06	-0.68
Monte Carlo model	645.9	492.2	425.1	1.09	2.01	-0.16
Case 6						
Measurements [7]	97.6	0.8	623.2			
CHARTS [7]	92.1	0.0	628.8	-5.64	-100.00	0.90
Monte Carlo model	94.0	1.7	629.2	-3.67	110.52	0.96
Case 7						
Measurements [7]	479.8	8	356			
CHARTS [7]	473.7	0.1	356.4	-1.27	-98.75	0.11
Monte Carlo model	477.6	9.1	354.6	-0.46	13.17	-0.38

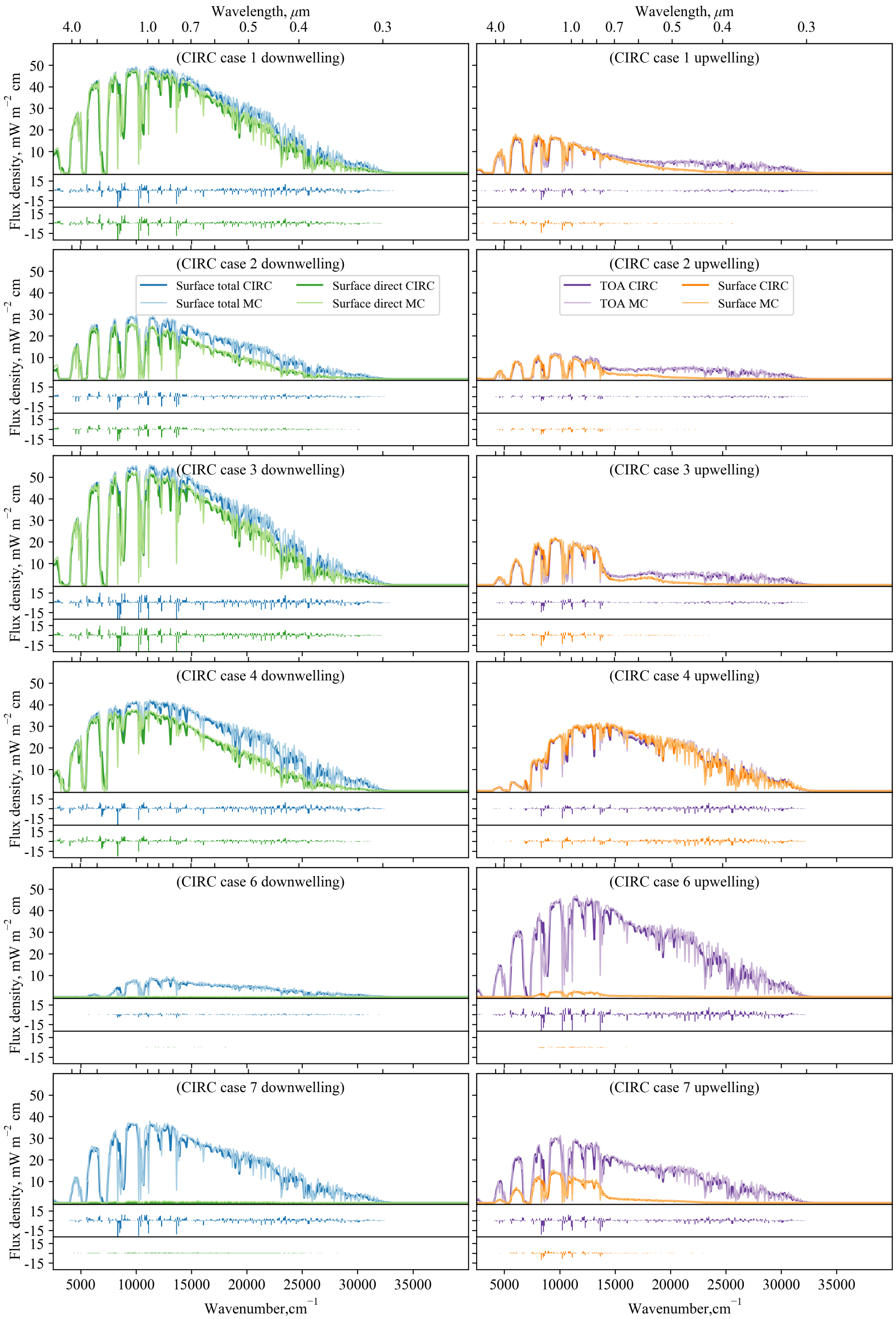

Figure 5.5: Spectral comparison between the proposed MC model and the CHARTS model for six CIRC cases.

Chapter 6

Local thermal effects caused by surface albedo replacement of large scale photovoltaic and concentrated solar farms

6.1 Introduction

Large-scale deployment of renewable energy technologies as replacement for fossil fuel generation aims at mitigating global warming rates by reducing the emission of greenhouse gases (GHG). The scale of this offset is critical to validate societal investments in technologies that may be at the brink of achieving power grid parity. Two major solar technologies arose from market competition in the past decade for utility scale central power plants: photovoltaic (PV) and concentrated solar power (CSP). Of the several CSP technologies, those based on central towers with large heliostat fields appear to be the most efficient. These large scale solar farms also interact with the atmosphere and with the ground though surface albedo replacement in addition to the direct GHG emission offset. Solar PV farms are highly absorbing (lower albedo) while CSP farms are highly reflective (higher albedo) when compared to the ground that they cover.

On one hand, PV generation is economically viable for distributed generation and can be scaled down to kilowatts (household rooftops). On the other hand, CSP plants offer a number of advantages for larger-scale power production, including higher efficiency (smaller solar field footprint), lower cost of thermal storage, higher capacity factors, etc. Photovoltaic systems supply usable solar power by means of direct photoelectric conversion. A typical PV system consists of fixed or sun tracking arrays of semiconductor solar panels that absorb and convert broad wavelength solar irradiance into DC power. Inverters transform electric current from direct (DC) to alternating (AC) current locally, and transformers elevate the voltage for transmission.

Concentrated solar power systems generate solar power by using mirrored surfaces (or sometimes lenses) to concentrate the beam solar irradiance in order to elevate the temperature of pressurized steam. The energized steam then drives one or more turbines that are coupled to AC generators. Direct steam CSP tower plants use tens to hundreds of thousands of mirrors to concentrate radiative power on a boiler that transfer the heat to high-energy steam for operation of vapor turbines. Dry cooling fans that dispense the use of additional cooling water close the low-temperature Rankine cycle and return the vapor to the liquid state for pumping. A modern tower CSP plant operates with very low consumption of water and is thus suitable for arid and semi-arid climates. Widely recognized advantages of CSP technologies for central power plant generation (>100 MW) are: higher thermodynamic conversion efficiency (40% vs 20% for PV panels); reliance on the direct normal component of the solar irradiance, which allows for a flatter generation profile throughout the day; and the lower cost of long-term thermal storage as compared to long-term electrical storage. The main advantages of PV include: simplicity of the direct photoelectric conversion technology (plants are less labor intensive); ability to generate partial power under cloudy conditions; and the modular and scalable nature of plant design. Another potential benefit of widespread CSP deployment is a much greater GHG emission offset due to the very high albedo of heliostat fields. However, this resulting change in the albedo of the surface as well as the temperature and evapotranspiration of water at a CSP deployment may have implications for local cloud cover. The extent to which such changes would reduce or increase surface warming requires a regional simulation of the cloud properties, cloud fraction, and cloud duration. While both PV and CSP technologies affect the local environment, the extent in which they do so has not been studied in detail.

Nemet [94] estimated that the low albedo of PV panels is responsible for lowering the GHG emission offset by 3% when compared with current carbon-intensive energy scenarios. As the penetration of renewable sources increases, that percentage will also increase, and perhaps to a point of being a significant hindrance to continued GHG emission offsets. Even more important, the local thermal balance effects may cause local environmental disruption in desert areas that rely strongly on the very low soil water content. Midday temperature increases of more than 3 K have been observed in desert PV plants [95]. Conversely, heliostat fields in CSP tower plants are characterized by albedos that are 40-50% higher than the original ground albedo, thus the GHG emission offset for CSP is much higher in comparison to PV technologies. Locally, a temperature reduction of 2 K and reduced rates of evapotranspiration have been observed as a direct result of the increased albedo of heliostat fields [95, 96].

This Chapter aims at quantifying the albedo replacement effects of large scale solar farms mainly concerns the temperature anomaly calculated from local radiative balance of the PV and CSP surfaces.

6.2 Spectral albedo of surfaces

Large scale solar farms interact with the atmosphere though land surface albedo replacement. Solar PV farms are highly absorbing (lower albedo) while CSP farms are highly reflective (higher albedo) when compared to the ground. The spectral albedo of regular surfaces, PV panels and CSP heliostats are plotted in Fig. 6.1, where PV panels have spectral albedo smaller than 0.1 while CSP heliostats have albedo greater than 0.9 in infrared and visible bands. Among the six CIRC cases, surfaces of case 1-3, 6 and 7 have nearly the same albedo while the surface of case 4 has much higher albedo in visible and UV bands, indicating the presence of ice or snow. For the analysis of this section, the regular ground is chosen to be the surface of CIRC case 2. PV panels are assumed to be Si pillar solar cells (pillar 3) with spectral reflectance data given by Ref. [8]. The reflection of PV panels is assumed to be diffused. CSP heliostats are assumed to be AgGlass 4 mm Flat glass mirrors, with spectral specular reflectance data given by Ref.[9]. All surfaces are assumed to be oriented horizontally facing the open sky. The vertical profiles of temperature, gases, aerosols and optical properties of gases, aerosols, clouds follow the methodologies presented in Ref. [5].

Note that the effects of PV and CSP farms presented in the following sections are the 'maximum' effects, because in the one dimensional radiative model, the entire ground is covered by PV or CSP, but in reality, only a portion of the ground is covered.

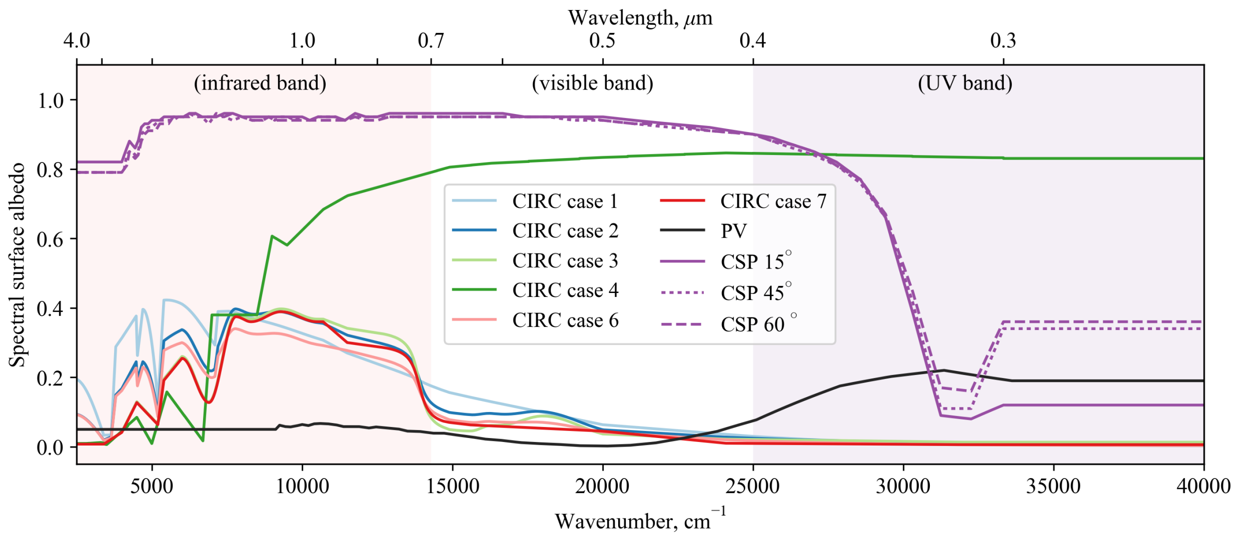

Figure 6.1: Spectral surface albedo of six CIRC cases [7], PV panels [8] and CSP heliostats [9].

6.3 Effects on local solar irradiance field

6.3.1 Under clear skies

Under clear skies, the main atmospheric participators are water vapor and aerosols. Figure 6.2 plots the broadband albedo effects when $\theta_z = 30°$ with respect to ambient AOD and normalized water vapor partial pressure p_w, which is defined as $p_w = \phi P_s(T_a)/P_0$, with ϕ being the relative humidity, P_s being saturated water vapor pressure and $P_0 = 1.013 \times 10^5$ Pa.

The first column of Fig. 6.2 shows the broadband flux for regular surface, the second and third columns show the flux differences caused by the presence of PV farms and CSP farms, respectively. For regular surface, the surface GHI decreases with increased p_w and AOD, so do surface DNI and TOA upwelling fluxes, because the participation of aerosols and water vapor is mainly by absorbing the shortwave radiation.

The second column of Fig. 6.2 shows that the presence of PV farms decreases the local GHI by 0.1 to 6.2 W m^{-2}. The absolute value of GHI modification is weakly dependent on p_w but increases with increased AOD. The DNI modification of PV farms is negligible. The low albedo of PV substantially reduces the TOA upwelling flux, because it 'traps' more radiation to the ground so less would reflected back to the outer space. The TOA upwelling suppression ranges from 59.9 to 125.2 W m^{-2} (up to 62%), decreases with increased AOD and p_w.

The third column of Fig. 6.2 shows that the presence of CSP farms increases the local GHI by 22.5 to

39.6 W m^{-2} (around 4%). The GHI enhancement is caused by heliostats reflected upwelling radiation being scattered back to the surface by gas molecules and aerosols. The GHI enhancement is weakly dependent on p_w but decreases with increased AOD. The DNI modification of CSP farms is again negligible, because the majority of backscatterd irradiance is not in the direction of solar beams. The high albedo of CSP substantially increases the TOA upwelling flux, and the increase could be as high as 187%. The TOA upwelling flux enhancement ranges from 302.7 to 572.7 W m^{-2}, decreases with increased AOD and p_w. The CSP is expected to cool the surface because of the enhancement of TOA upwelling flux.

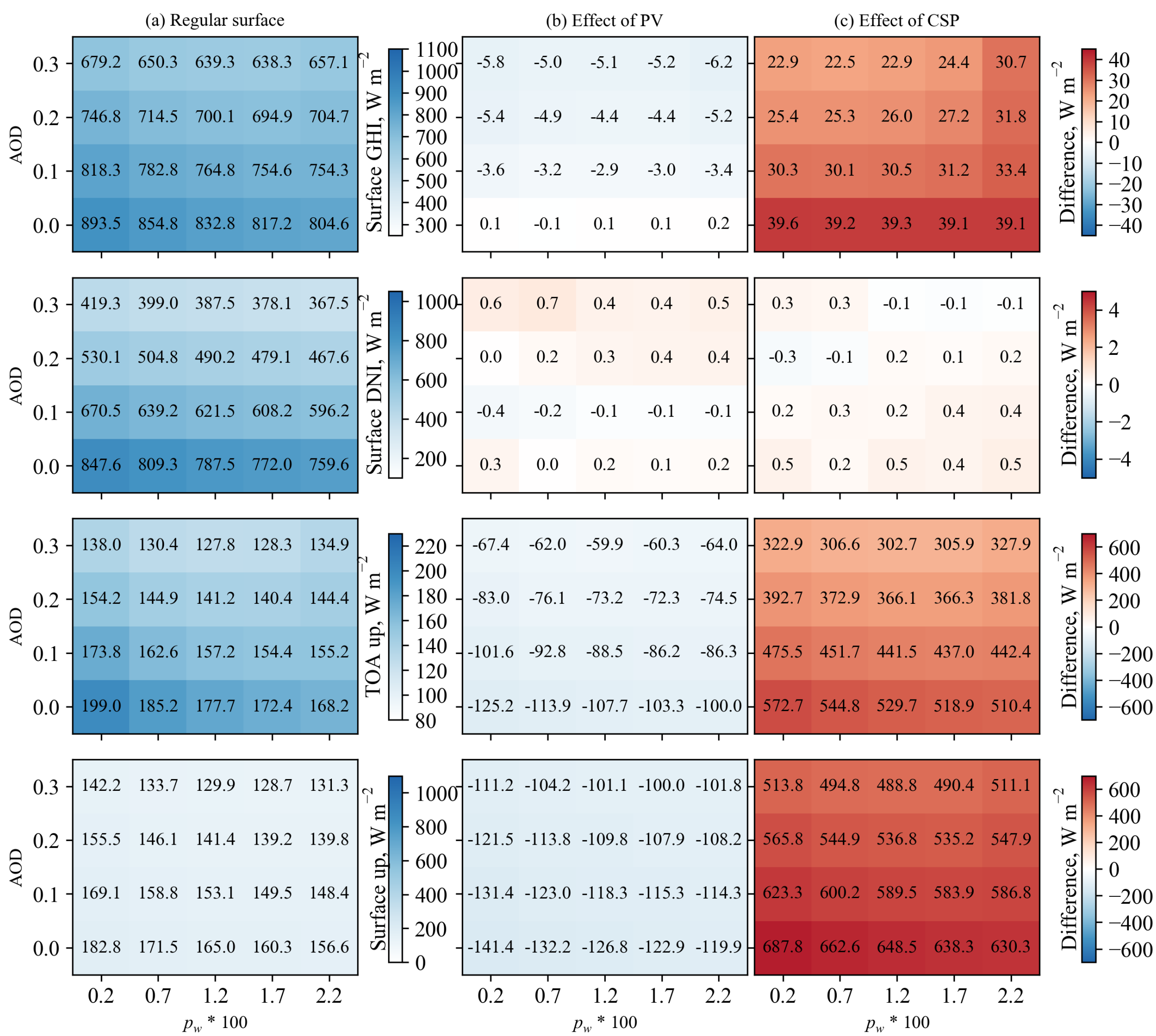

Figure 6.2: Albedo replacement effects of PV and CSP farms under clear skies for $\theta_z = 30°$. The first column shows broadband fluxes of regular ground surface. The second and third columns show the flux modification caused by the presence of PV and CSP farms, respectively.

6.3.2 Under cloudy skies

Under cloudy skies, the main atmospheric participators are water vapor, aerosols and clouds. The cloud base height, thickness and optical depth are a function of surface p_w, as analyzed in section 4.4, where the cloud optical depth is an increasing function of p_w. Figure 6.3 plots the broadband albedo effects when $\theta_z = 30°$ with overcast water clouds.

Compare with Fig. 6.2, the surface GHI and DNI decreases more strongly with p_w when clouds are present because clouds reduce GHI and DNI and the optical depth of clouds increases with p_w. The TOA upwelling flux increases substantially with the presence of clouds because of the high albedo of clouds, especially when the clouds are optically thick. The surface GHI modification of PV and CSP is enhanced by the presence of clouds, especially for CSP because the photons can be reflected several times between the high albedo clouds and the surfaces of heliostats. The presence of PV suppresses while the presence of CSP enhances TOA upwelling flux as under clear skies. The suppression and enhancement are greatly reduced when $p_w > 0.7$ because that the albedo replacement of clouds overrules the albedo replacement of PV and CSP.

Under partly cloudy skies, the irradiance difference caused by albedo replacement is expressed as,

$$\Delta I = (1 - \mathrm{CF})\Delta I_c + \mathrm{CF}\Delta I_{oc} \tag{6.1}$$

where CF is the cloud fraction, subscript ‘c’ represents clear skies and ‘oc’ represents overcast skies. For different values of CF, the albedo replacement effects can be calculated from ΔI_c in Fig. 6.2 and ΔI_{oc} in Fig. 6.3.

6.3.3 Thermal balance at the surface

A thermal balance accounts for both longwave and shortwave irradiance is then performed for regular surface, PV and CSP farms. The scheme of the thermal balance is shown in Fig. 6.4. In the longwave spectral, all the surfaces can be viewed as black surfaces, with emissive power equals to σT_{ss}^4, where the surface steady state temperature T_{ss} is found from the balance,

$$G_{\mathrm{sw}} + G_{\mathrm{lw}} = J_{\mathrm{sw}} + J_{\mathrm{lw}} + q_c + q_d + q_e \tag{6.2}$$

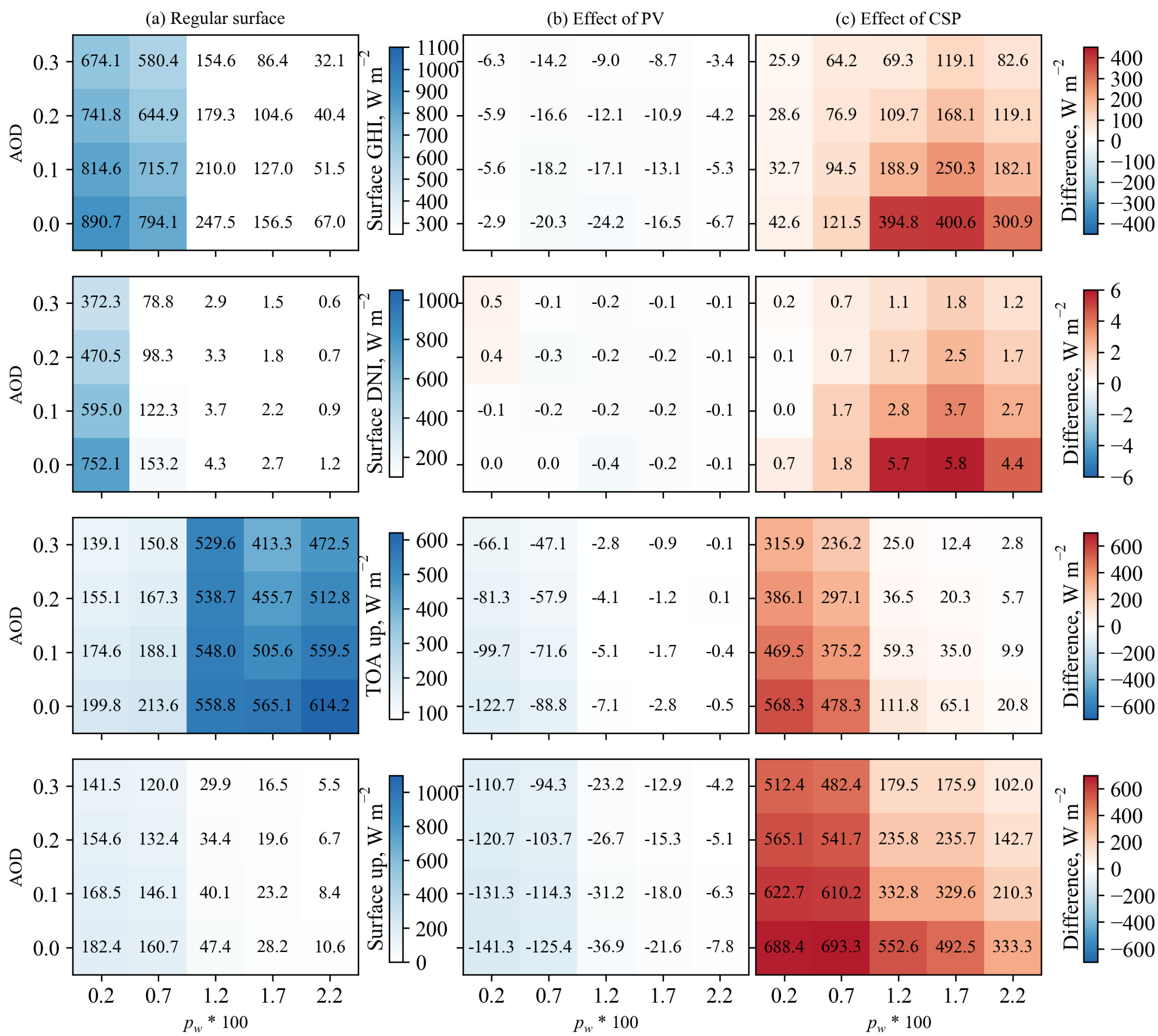

Figure 6.3: Albedo replacement effects of PV and CSP farms when θ_z = 30°. Same as Fig.6.2 but for overcast skies.

where $G_{\rm sw}$ (W m^{-2}) and $J_{\rm sw}$ (W m^{-2}) are the shortwave surface downwelling and upwelling flux as shown in Figs. 6.2 and 6.3; $G_{\rm lw}$ (W m^{-2}) is the longwave surface downwelling flux, which is the radiation from the sky, $G_{\rm lw} = J_{\rm sky} = \epsilon_{\rm sky}\sigma T_a^4$, where the effective sky emissivity $\epsilon_{\rm sky}$ can be calculated using the regression formula given in Chapters 2 and 4; $J_{\rm lw} = \sigma T_{ss}^4$ (W m^{-2}) is the emitted longwave radiation from the surface; $q_c + q_d$ is the convective and conductive heat loss from the surface, which could be estimated as $h_c(T_{ss} - T_a)$ where h_c can be taken as 6.9 W m^{-2} K [18]; q_e (W m^{-2}) is the electric power generated by the PV panels, which equals to $\eta_e(G_{\rm sw} - J_{\rm sw})$, where the panel efficiency is assumed to be 17% [97].

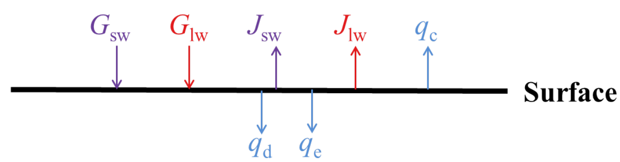

Figure 6.4: The scheme of thermal balance of surfaces placed horizontally to open sky.

6.3.4 Under clear skies

Figure 6.5 plots the equilibrium temperature of the regular ground, effects of PV farms and CSP farms with respect to ambient air temperature and relative humidity, under clear skies when $\theta_z = 30°$ and AOD$= 0.1$. Under direct sunlight, the surface temperature of regular ground is around 40 K above the ambient temperature. CSP farms greatly reduces the surface temperature, and the heliostats temperature can be 3 K below the ambient air temperature, creating a cooling effect. If the PV farm is generating electricity with an efficiency of 17%, the surface temperature is slightly decreased. On the other hand, if the PV farm is not operating, the surface temperature is increased by 6.5 to 9.3 K.

6.3.5 Under cloudy skies

Under cloudy skies, clouds increase surface downwelling longwave irradiance by emission but decrease downwelling shortwave irradiance by reflection and absorption. Figure 6.6 plots the equilibrium temperature of surfaces similar to Fig. 6.5 but under skies with overcast water clouds. For regular surface, the surface temperature is lower when compared to clear skies. When thick clouds are present ($\phi > 50\%$), T_{ss} is comparable with T_a. The T_{ss} modifications by CSP and PV farms is reduced with the presence of clouds, especially when optically thick clouds are present. When $\phi > 50\%$, the surface warming effect of PV farms is

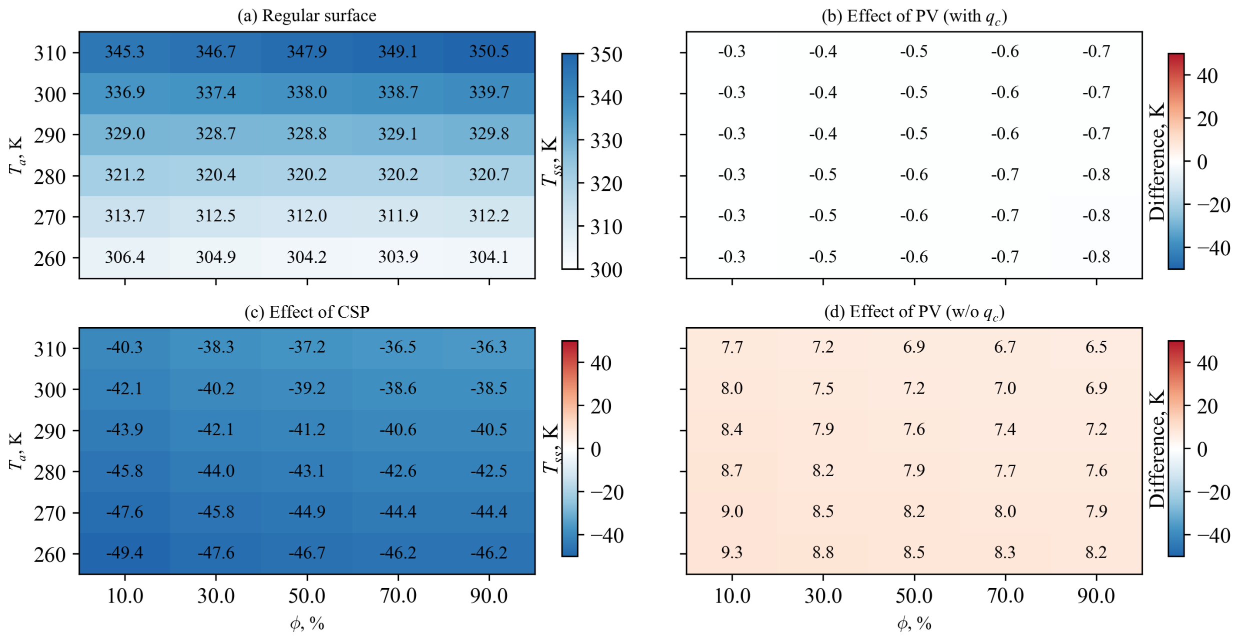

Figure 6.5: The equilibrium surface temperature with respect to ambient air temperature and relative humidity, under clear skies when $\theta_z = 30°$ and AOD= 0.1.

diminished. The surface temperature of CSP farms is again around 3 K below the air temperature, which is not strongly affected by the presences of clouds, because its low absorptance in the shortwave spectrum.

Under partly cloudy skies, the equilibrium temperatures of surfaces are in between those under clear skies and overcast skies.

6.4 Conclusions

A comprehensive spectral Monte Carlo radiative model is developed to quantify the local thermal effects caused by surface albedo replacement of large scale photovoltaic and concentrated solar farms. Under clear skies, local GHI decreases by 0.1 to 6.2 W m^{-2} with the presence of PV farms. On the contrary, local GHI is enhanced by 22.5 to 39.6 W m^{-2} with the presence of CSP farms. Top of atmosphere upwelling is suppressed by 59.9 to 125.2 W m^{-2} with PV farms on the ground while boosted by 302.7 to 572.7 W m^{-2} with CSP farms on the ground. Under cloudy skies, with overcast water clouds, the extent of local GHI reduction and augmentation by PV and CSP is increased. The GHI enhancement can be as high as 250.3 W m^{-2} for normal aerosol loading (AOD= 0.1), which is caused by multiple reflection of radiation between high albedo CSP field and water clouds.

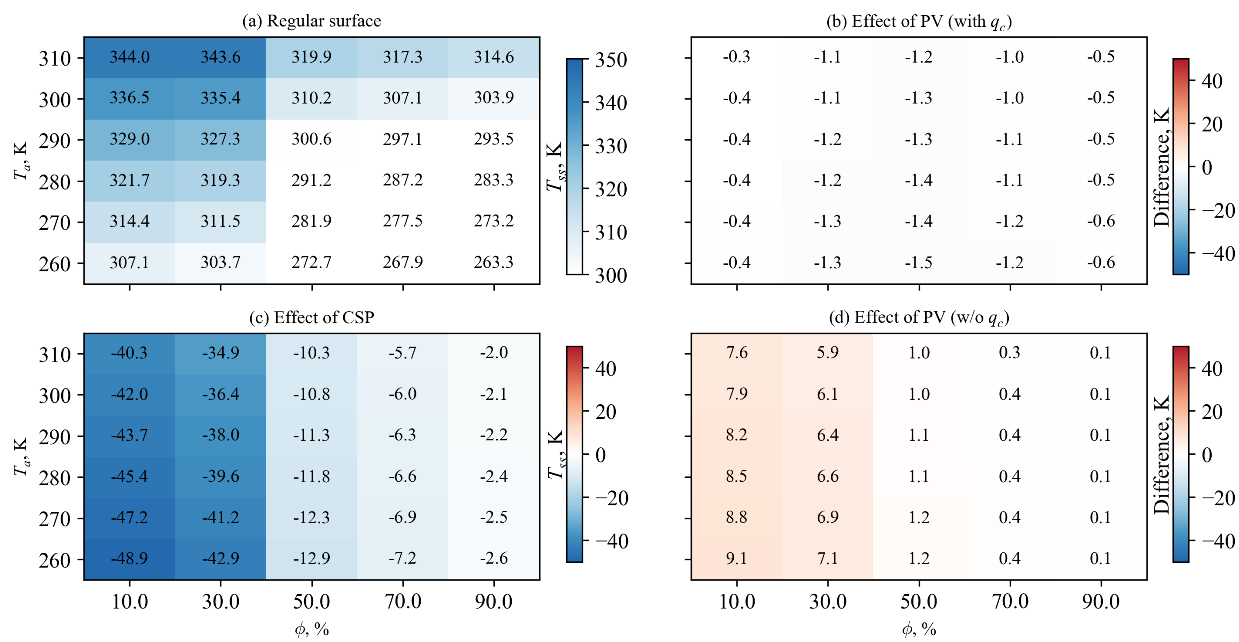

Figure 6.6: The equilibrium surface temperature with respect to ambient air temperature and relative humidity, under overcast skies when $\theta_z = 30°$ and AOD= 0.1.

A thermal balance is then performed to calculate the equilibrium temperature of regular ground, PV and CSP farms. Under direct sunlight, the regular ground can be heated to be 40 K above ambient temperature. With the presence of PV farms, the surface temperature increases 6.5 K to 9.3 K more on top of the 40 K, if the PV farm is not operating. With an electricity conversion efficiency of 17%, the 6.5 K to 9.3 K surface temperature increase could be offset. On the other hand, with the presence of CSP heliostats field, the surface temperature is 3 K lower than ambient temperature, which provides cooling effect. When compared with the 40 K temperature rise for regular surface, CSP reduces the surface temperature by 43 K. Under overcast skies, the surface temperature of regular surface is reduced when compare with under clear skies, because clouds reduce the surface downwelling shortwave flux. With the presence of optically thick clouds, the surface temperature is comparable with ambient temperature. The surface temperature increment caused by PV farms is reduced with the presence of optically thick clouds. The surface temperature of CSP farms remains to be around 3 K below the ambient, which is not strongly influenced by clouds because the low absorptance of the heliostats in the shortwave spectrum prevents them from absorbing downwelling solar irradiance.

6.5 Acknowledgments

This Chapter, in full, is in preparation as a manuscript for publication with my co-author and Ph.D. adviser C. F. M Coimbra at UC San Diego. The dissertation author is also the first author of this paper.

Chapter 7

Conclusions

Atmospheric longwave radiation and solar shortwave radiation are essential components of thermal balances in the atmosphere, playing also a substantial role in the design and operation of engineered systems that exposed to open sky, for examples, cooling towers, radiative cooling devices and solar power plants. To quantify the spectral thermal balances of the atmosphere and engineered systems, especially optically selective devices, comprehensive line-by-line radiative models are developed to simulate atmospheric longwave and solar shortwave radiative transfer in the Earth - atmosphere system, as well as the interactions between engineered systems and the atmosphere.

Firstly, simple parametric models are developed to calculate broadband downwelling longwave irradiance at the surface. Under clear skies, fifteen parametric broadband models for calculating longwave irradiance are compared and recalibrated. All models achieve higher accuracy after grid search recalibration, and we show that many of the previously proposed LW models collapse into only a few different families of models. A recalibrated Brunt-family model is recommended for future use due to its simplicity and high accuracy (rRMSE = 4.37%). To account for the difference in nighttime and daytime clear-sky emissivities, nighttime and daytime Brunt-type models are proposed. Under all sky conditions, the information of clouds is represented by cloud cover fraction (CF) or cloud modification factor (CMF, available only during daytime). Three parametric models proposed in the literature are compared and calibrated, and a new model is proposed to account for the alternation of vertical atmosphere profile by clouds. The proposed all-sky model has 3.8% ~ 31.8% lower RMSEs than the other three recalibrated models. If GHI irradiance measurements are available, using CMF as a parameter yields 7.5% lower RMSEs than using CF. For different applications that require LW information during daytime and/or nighttime, coefficients of the proposed models are corrected for diurnal and nocturnal use.

Then, an efficient spectrally resolved radiative model is developed to capture spectral characteristics of longwave radiation in the atmosphere, under clear and cloudy skies. For the non-scattering clear atmosphere (aerosol free), the surface DLW agrees within 2.91% with mean values from the InterComparison of Radiation Codes in Climate Models (ICRCCM) program, with spectral deviations below 0.035 $\mathrm{W\,cm\,m^{-2}}$. For a scattering clear atmosphere with typical aerosol loading, the DLW calculated by the spectral model agrees within 3.08% relative error when compared to measured values at seven climatologically diverse SURFRAD stations. This relative error is smaller than the aforementioned calibrated parametric model regressed from data for those same seven stations, and within the uncertainty (+/- 5 $\mathrm{W\,m^{-2}}$) of pyrgeometers commonly used for meteorological and climatological applications.

The broadband and spectral forcing of water vapor, carbon dioxide and aerosols are quantified using the model. When aerosol optical depth (AOD) equals 0.1 (497.5 nm/ground level) are considered, longwave aerosol forcing falls between 1.86 $\mathrm{W\,m^{-2}}$ to 6.57 $\mathrm{W\,m^{-2}}$. The forcing increases with decreasing values of surface water vapor content because the aerosol bands contribute mostly when the water vapor bands are not saturated. When examining the spatial and spectral contributions of water vapor to the surface DLW, we find, as expected, that water vapor in the nearest surface layer contributes the most, especially in the spectral ranges 0 ~ 400 $\mathrm{cm^{-1}}$ (water vapor absorbing band) and 580 ~ 750 $\mathrm{cm^{-1}}$ (CO_2 absorbing band). Within the atmospheric spectral windows 400 ~ 580 $\mathrm{cm^{-1}}$, 750 ~ 1400 $\mathrm{cm^{-1}}$ and 2400 ~ 2500 $\mathrm{cm^{-1}}$, water vapor above 3.46 km has negligible effect on the monochromatic surface DLW. In some spectral regions, there is a decrease in water vapor forcing because water vapor content in the layers below prevents the longwave radiation from reaching the surface. The warming caused by aerosols mostly comes from the layers below 3.46 km. In a narrow spectral band between 1050 to 1150 $\mathrm{cm^{-1}}$ above 3.46 km, there is a decrease in monochromatic surface DLW forcing, since the lower layer aerosols prevent the radiation from reaching the surface by absorption.

Spectral and spatial distribution of irradiation is presented for an atmosphere with surface relative humidity of 65% and aerosol optical depth at 479.5 nm equals to 0.1. First order broadband contributions of increased atmospheric CO_2 to surface downwelling flux is found to be 0.3 ~ 1.2 $\mathrm{W\,m^{-2}}$ per 100 ppm CO_2 increment for different water vapor contents. The broadband reduction of TOA upwelling flux is found to be

$0.5 \sim 0.7$ W m^{-2} per 100 ppm CO_2 increment.

Contributions to the irradiation on the top atmosphere layer and outer space layer come from the surface in the atmospheric window bands, from the middle of atmosphere in the water vapor absorbing bands and from the top of atmosphere in the CO_2 absorbing bands. For broadband flux contributions, the outer space layer dominates the transfer factors to upper layers (above the tropopause) but the flux contribution is negligible due to low densities and effective temperatures at that level. For the ground layer, 64.4%, 15.3% and 7.5% of its longwave irradiation comes from the nearest atmospheric layer, the 2nd nearest layer and the 3rd nearest layer, respectively. And the contributions mostly from the four absorbing bands. For all layers below the tropopause, the layer itself contributes the most to its irradiation. For layers above the tropopause layer, the largest contributor to its irradiation is the ground layer. Finally, upper layers above the tropopause contribute to less than 4.8% to the irradiance flux to other layers.

Then accurate correlations for the effective sky emissivity as functions of the normalized ambient partial pressure of water vapor (p_w) for both broadband and seven distinct bands of the infrared spectrum are proposed. The band emissivities are correlated by simple expressions to ambient meteorological conditions at the ground level, and allow for the expedient calculation of cooling power efficiencies of optically selective materials designed for passive cooling or heating. Comparisons between band calculations and line-by-line calculations yield errors that are generally within the measurement uncertainty of atmospheric instrumentation (e.g., pyrgeometers or broadband pyranometers, with uncertainties ranging from $3-6\%$), thus validating the combined approach of high fidelity spectral models with ground experiments taken at diverse micro-climates, altitudes and meteorological conditions.

When clouds are added to the spectral model, the representative cloud characteristics are also proposed as empirical functions for different surface meteorological conditions to guide future modeling efforts. These results enable direct calculation of the equilibrium temperature and cooling efficiency of passive cooling devices in terms of meteorological conditions observed at the surface level. The cooling potential of passive cooling materials is found to be as high as 140 W m^{-2} for dry and hot conditions without the presence of clouds. But the potential diminishes with increased water vapor content and the presence of clouds, because both water vapor and clouds 'block' the atmospheric window for cooling.

A Monte Carlo line-by-line radiative model is developed for solar shortwave radiative transfer in the atmosphere, with different surfaces (e.g. soil, PV and CSP farms). The local thermal effects of albedo replacements of PV and CSP farms are quantified. Under clear skies, the downwelling GHI is being suppressed by the presence of PV farms while being enhanced by the presence of CSP farms (around 4%), because of the back-scattering of reflected irradiance from heliostats. The TOA upwelling flux enhancement of CSP plant could be as high as 187%, so that CSP fields are able to cool the surface. Under cloudy skies, the GHI enhancement by CSP is amplified by the presence of clouds because multiple reflections occur between highly reflective CSP farms and clouds. By performing a surface thermal balance, the surface temperature of CSP is 3 K lower than the ambient while the surface temperature of PV or regular surface is more than 40 K above the ambient while under direct sunlight. Under cloudy skies, the irradiance and temperature modification of PV and CSP farms are reduced because the effects of clouds, especially optically thick clouds, dominant.

The results presented here strongly suggest the possibility of hybrid solar plant designs that employ an outer ring of PV solar field surrounding an inner heliostat field around the central tower. This hybrid design accomplishes two important objectives: (i) minimization of local changes in temperature and humidity by balancing out the heating caused by the PV field with the cooling caused by the CSP heliostats, and (ii) the minimization of DNI variability effects on plant operation through the coupling with the less-variable GHI component absorbed by PV panels.

In addition, the thermal balance discussed in this work also allows for the consideration of dual land use, especially under the heliostat field. A raised heliostat field with partial shading may be used for agricultural purposes in desert areas where very few plants could survice without partial shade and lower temperatures and higher humidities. Note that PV panels not only increase downwelling infrared radiation to the soil, but also prevent radiative exchange with the desert sky at night, which in many regions is the mechanism that allows for the formation of dew at night. By considering these different heat and mass transfer mechanisms carefully, novel solar power plant designs may reduce their environmental impact on desertic areas.

Bibliography

[1] National Oceanic and Atmospheric Administration, SURFRAD Network, http://www.esrl.noaa.gov/gmd/grad/surfrad/ (2015).

[2] D. Lubin, S. Satheesh, G. McFarquar, A. J. Heymsfield, Longwave radiative forcing of Indian Ocean tropospheric aerosol, Journal of Geophysical Research: Atmospheres 107 (D19).

[3] G. M. Hale, M. R. Querry, Optical constants of water in the 200-nm to 200-μm wavelength region, Applied optics 12 (3) (1973) 555–563.

[4] U.S. Department of Energy, ICRCCM infrared (clear-sky) line-by line radiative fluxes (DB-1002), http://cdiac.ornl.gov/ndps/db1002.html (2017).

[5] M. Li, Z. Liao, C. F. M. Coimbra, Spectral model for clear sky atmospheric longwave radiation, Journal of Quantitative Spectroscopy and Radiative Transfer 209 (2018) 196–211.

[6] A. Bucholtz, Rayleigh-scattering calculations for the terrestrial atmosphere, Applied Optics 34 (15) (1995) 2765–2773.

[7] National Oceanic and Atmospheric Administration, CIRC: Continual intercomparison of radiation codes, https://circ.gsfc.nasa.gov/.

[8] M. Patel, J. Kim, Optical properties and impedance spectroscopy analyses for microscale Si pillar solar cells, Data in brief 14 (2017) 1–5.

[9] P. Good, T. Cooper, M. Querci, N. Wiik, G. Ambrosetti, A. Steinfeld, Spectral data of specular reflectance, narrow-angle transmittance and angle-resolved surface scattering of materials for solar concentrators, Data in brief 6 (2016) 184–188.

[10] National Oceanic and Atmospheric Administration, Automated surface observing system user's guide, http://www.nws.noaa.gov/asos/pdfs/aum-toc.pdf (1998).

[11] R. H. Inman, J. G. Edson, C. F. M. Coimbra, Impact of local broadband turbidity estimation on forecasting of clear sky direct normal irradiance, Solar Energy 117 (2015) 125–138.

[12] K. N. Liou, An Introduction to Atmospheric Radiation, Vol. 84, Academic Press, Cambridge, MA, United States, 2002.

[13] S. A. Buehler, A. Von Engeln, E. Brocard, V. O. John, T. Kuhn, P. Eriksson, Recent developments in the line-by-line modeling of outgoing longwave radiation, Journal of Quantitative Spectroscopy and Radiative Transfer 98 (3) (2006) 446–457.

[14] S. Solomon, J. S. Daniel, T. J. Sanford, D. M. Murphy, G.-K. Plattner, R. Knutti, P. Friedlingstein, Persistence of climate changes due to a range of greenhouse gases, Proceedings of the National Academy of Sciencesdoi:10.1073/pnas.1006282107.

[15] M. Shen, S. Piao, S.-J. Jeong, L. Zhou, Z. Zeng, P. Ciais, D. Chen, M. Huang, C.-S. Jin, L. Z. Li, Y. Li, R. Myneni, K. Yang, G. Zhang, Y. Zhang, T. Yao, Evaporative cooling over the Tibetan Plateau induced by vegetation growth, Proceedings of the National Academy of Sciences 112 (30) (2015) 9299–9304.

[16] M. Li, Y. Jiang, C. F. M. Coimbra, On the determination of atmospheric longwave irradiance under all-sky conditions, Solar Energy 144 (2017) 40–48.

[17] L. Zhu, A. P. Raman, S. Fan, Radiative cooling of solar absorbers using a visibly transparent photonic crystal thermal blackbody, Proceedings of the National Academy of Sciences 112 (40) (2015) 12282–12287.

[18] A. P. Raman, M. A. Anoma, L. Zhu, E. Rephaeli, S. Fan, Passive radiative cooling below ambient air temperature under direct sunlight, Nature 515 (7528) (2014) 540.

[19] Z. Chen, L. Zhu, A. Raman, S. Fan, Radiative cooling to deep sub-freezing temperatures through a 24-h day–night cycle, Nature communications 7 (2016) 13729.

[20] Y. Zhai, Y. Ma, S. N. David, D. Zhao, R. Lou, G. Tan, R. Yang, X. Yin, Scalable-manufactured randomized glass-polymer hybrid metamaterial for daytime radiative cooling, Science 355 (6329) (2017) 1062–1066.

[21] A. F. Mills, C. F. M. Coimbra, Basic heat and mass transfer, 3rd Edition, Temporal Publishing, San Diego, CA, 2015.

[22] National Renewable Energy Laboratory, 2000 ASTM standard extraterrestrial spectrum reference E-490-00, https://www.nrel.gov/grid/solar-resource/spectra-astm-e490.html.

[23] F. Kasten, A. T. Young, Revised optical air mass tables and approximation formula, Applied optics 28 (22) (1989) 4735–4738.

[24] P. Ineichen, R. Perez, A new airmass independent formulation for the Linke turbidity coefficient, Solar Energy 73 (3) (2002) 151–157.

[25] P. Ineichen, Comparison of eight clear sky broadband models against 16 independent data banks, Solar Energy 80 (4) (2006) 468–478.

[26] P. Ineichen, Conversion function between the linke turbidity and the atmospheric water vapor and aerosol content, Solar Energy 82 (11) (2008) 1095–1097.

[27] I. Alados, I. Foyo-Moreno, L. Alados-Arboledas, Estimation of downwelling longwave irradiance under all-sky conditions, International Journal of Climatology 32 (5) (2012) 781–793.

[28] F. Carmona, R. Rivas, V. Caselles, Estimation of daytime downward longwave radiation under clear and cloudy skies conditions over a sub-humid region, Theoretical and applied climatology 115 (1-2) (2014) 281–295.

[29] U. Eicker, A. Dalibard, Photovoltaic–thermal collectors for night radiative cooling of buildings, Solar Energy 85 (7) (2011) 1322–1335.

[30] F. Zaversky, J. García-Barberena, M. Sánchez, D. Astrain, Transient molten salt two-tank thermal storage modeling for CSP performance simulations, Solar Energy 93 (2013) 294–311.

[31] D. Brunt, Notes on radiation in the atmosphere. I, Quarterly Journal of the Royal Meteorological Society 58 (247) (1932) 389–420.

[32] W. Brutsaert, On a derivable formula for long-wave radiation from clear skies, Water Resources Research 11 (5) (1975) 742–744.

[33] C. Ruckstuhl, R. Philipona, J. Morland, A. Ohmura, Observed relationship between surface specific humidity, integrated water vapor, and longwave downward radiation at different altitudes, Journal of Geophysical Research: Atmospheres (1984–2012) 112 (D3).

[34] A. Maghrabi, R. Clay, Nocturnal infrared clear sky temperatures correlated with screen temperatures and GPS-derived PWV in Southern Australia, Energy Conversion and Management 52 (8) (2011) 2925–2936.

[35] P. Berdahl, R. Fromberg, The thermal radiance of clear skies, Solar Energy 29 (4) (1982) 299–314.

[36] R. Tang, Y. Etzion, I. A. Meir, Estimates of clear night sky emissivity in the Negev Highlands, Israel, Energy Conversion and Management 45 (11) (2004) 1831–1843.

[37] J. Bilbao, A. H. De Miguel, Estimation of daylight downward longwave atmospheric irradiance under clear-sky and all-sky conditions, Journal of applied meteorology and climatology 46 (6) (2007) 878–889.

[38] O. A. Alduchov, R. E. Eskridge, Improved Magnus form approximation of saturation vapor pressure, Journal of Applied Meteorology 35 (4) (1996) 601–609.

[39] Golden Gate Weather Service, El Niño and La Niña years and intensities, http://ggweather.com/enso/oni.htm (2016).

[40] Iowa State University of Science and Technology, ASOS-AWOS-METAR data download, https://mesonet.agron.iastate.edu/request/ download.phtml (2016).

[41] M. J. Reno, C. W. Hansen, J. S. Stein, Global horizontal irradiance clear sky models: Implementation and analysis, SANDIA report SAND2012-2389.

[42] W. C. Swinbank, Long-wave radiation from clear skies, Quarterly Journal of the Royal Meteorological Society 89 (381) (1963) 339–348.

[43] S. B. Idso, R. D. Jackson, Thermal radiation from the atmosphere, Journal of Geophysical Research 74 (23) (1969) 5397–5403.

[44] D. R. Satterlund, An improved equation for estimating long-wave radiation from the atmosphere, Water Resources Research 15 (6) (1979) 1649–1650.

[45] S. B. Idso, A set of equations for full spectrum and 8-to 14-μm and 10.5-to 12.5-μm thermal radiation from cloudless skies, Water resources research 17 (2) (1981) 295–304.

[46] P. Berdahl, M. Martin, Emissivity of clear skies, Solar Energy 32 (5) (1984) 663–664.

[47] A. J. Prata, A new long-wave formula for estimating downward clear-sky radiation at the surface, Quarterly Journal of the Royal Meteorological Society 122 (533) (1996) 1127–1151.

[48] A. C. Dilley, D. M. O'brien, Estimating downward clear sky long-wave irradiance at the surface from screen temperature and precipitable water, Quarterly Journal of the Royal Meteorological Society 124 (549) (1998) 1391–1401.

[49] S. Niemelä, P. Räisänen, H. Savijärvi, Comparison of surface radiative flux parameterizations: Part I: Longwave radiation, Atmospheric Research 58 (1) (2001) 1–18.

[50] M. G. Iziomon, H. Mayer, A. Matzarakis, Downward atmospheric longwave irradiance under clear and cloudy skies: Measurement and parameterization, Journal of Atmospheric and Solar-Terrestrial Physics 65 (10) (2003) 1107–1116.

[51] Q. Dai, X. Fang, A new model for atmospheric radiation under clear sky condition at various altitudes, Advances in Space Research 54 (6) (2014) 1044–1048.

[52] J.-C. Dupont, M. Haeffelin, P. Drobinski, T. Besnard, Parametric model to estimate clear-sky longwave irradiance at the surface on the basis of vertical distribution of humidity and temperature, Journal of Geophysical Research: Atmospheres (1984–2012) 113 (D7).

[53] T. M. Crawford, C. E. Duchon, An improved parameterization for estimating effective atmospheric emissivity for use in calculating daytime downwelling longwave radiation, Journal of Applied Meteorology 38 (4) (1999) 474–480.

[54] T. Konzelmann, R. S. van de Wal, W. Greuell, R. Bintanja, E. A. Henneken, A. Abe-Ouchi, Parameterization of global and longwave incoming radiation for the Greenland Ice Sheet, Global and Planetary Change 9 (1) (1994) 143–164.

[55] H. F. Duarte, N. L. Dias, S. R. Maggiotto, Assessing daytime downward longwave radiation estimates for clear and cloudy skies in Southern Brazil, Agricultural and forest meteorology 139 (3) (2006) 171–181.

[56] W. L. Ridgway, A. Arking, Computation of atmospheric cooling rates by exact and approximate methods, Journal of Geophysical Research: Atmospheres 96 (D5) (1991) 8969–8984.

[57] S. A. Clough, M. W. Shephard, E. J. Mlawer, J. S. Delamere, M. J. Iacono, K. Cady-Pereira, S. Boukabara, P. D. Brown, Atmospheric radiative transfer modeling: a summary of the AER codes, Journal of Quantitative Spectroscopy and Radiative Transfer 91 (2) (2005) 233–244.

[58] S. A. Buehler, P. Eriksson, T. Kuhn, A. Von Engeln, C. Verdes, ARTS- the atmospheric radiative transfer simulator, Journal of Quantitative Spectroscopy and Radiative Transfer 91 (1) (2005) 65–93.

[59] A. Berk, F. Hawes, Validation of MODTRAN® 6 and its line-by-line algorithm, Journal of Quantitative Spectroscopy and Radiative Transfer 203 (2017) 542 – 556.

[60] I. E. Gordon, L. S. Rothman, C. Hill, R. V. Kochanov, Y. Tan, P. F. Bernath, M. Birk, V. Boudon, A. Campargue, K. Chance, B. Drouin, The HITRAN2016 molecular spectroscopic database, Journal of Quantitative Spectroscopy and Radiative Transfer 203 (2017) 3–69.

[61] E. J. Mlawer, V. H. Payne, J.-L. Moncet, J. S. Delamere, M. J. Alvarado, D. C. Tobin, Development and recent evaluation of the MT_CKD model of continuum absorption, Philosophical Transactions of the Royal Society of London A: Mathematical, Physical and Engineering Sciences 370 (2012) 2520–2556.

[62] A. Eddington, On the radiative equilibrium of the stars, Monthly Notices of the Royal Astronomical Society 77 (1916) 16–35.

[63] C. Sagan, J. B. Pollack, Anisotropic nonconservative scattering and the clouds of Venus, Journal of Geophysical Research 72 (2) (1967) 469–477.

[64] M. Q. Brewster, C. L. Tien, Examination of the two-flux model for radiative transfer in particular systems, International Journal of Heat and Mass Transfer 25 (12) (1982) 1905–1907.

[65] O. B. Toon, C. McKay, T. Ackerman, K. Santhanam, Rapid calculation of radiative heating rates and photodissociation rates in inhomogeneous multiple scattering atmospheres, Journal of Geophysical Research: Atmospheres 94 (D13) (1989) 16287–16301.

[66] D. K. Edwards, The plating algorithm for radiation script-F transfer factor, Journal of heat transfer 108 (1) (1986) 237–238.

[67] S. Manabe, F. Möller, On the radiative equilibrium and heat balance of the atmosphere, Monthly Weather Review, 1961.

[68] S. Manabe, R. F. Strickler, Thermal equilibrium of the atmosphere with a convective adjustment, Journal of the Atmospheric Sciences 21 (4) (1964) 361–385.

[69] G. P. Anderson, S. A. Clough, F. X. Kneizys, J. H. Chetwynd, E. P. Shettle, AFGL atmospheric constituent profiles (0.120 km), Tech. rep., DTIC Document (1986).

[70] Carbon Dioxide Information Analysis Center, Recent greenhouse gas concentrations, http://cdiac.ornl.gov/pns/current-ghg.html (2016).

[71] H. Yu, M. Chin, D. M. Winker, A. H. Omar, Z. Liu, C. Kittaka, T. Diehl, Global view of aerosol vertical distributions from CALIPSO lidar measurements and GOCART simulations: Regional and seasonal variations, Journal of Geophysical Research: Atmospheres 115 (D4).

[72] G. W. Petty, A first course in atmospheric radiation, Sundog Pubulishing, Madison, WI, United States, 2006.

[73] G. Lesins, P. Chylek, U. Lohmann, A study of internal and external mixing scenarios and its effect on aerosol optical properties and direct radiative forcing, Journal of Geophysical Research: Atmospheres 107 (D10).

[74] H. Yu, Y. Kaufman, M. Chin, G. Feingold, L. Remer, T. Anderson, Y. Balkanski, N. Bellouin, O. Boucher, S. Christopher, P. DeCola, K. R, K. D, L. N, R. M. S., S. M., Takemura, Z. M., A review of measurement-based assessments of the aerosol direct radiative effect and forcing, Atmospheric Chemistry and Physics 6 (3) (2006) 613–666.

[75] C. F. Bohren, D. R. Huffman, Absorption and scattering of light by small particles, John Wiley & Sons, 2008.

[76] C. Mätzler, MATLAB functions for Mie scattering and absorption, version 2, IAP Res. Rep 8 (2002) 1–24.

[77] J. Zhang, S. A. Christopher, Longwave radiative forcing of Saharan dust aerosols estimated from MODIS, MISR, and CERES observations on terra, Geophysical Research Letters 30 (23).

[78] J. E. Hansen, L. D. Travis, Light scattering in planetary atmospheres, Space science reviews 16 (4) (1974) 527–610.

[79] N. L. Miles, J. Verlinde, E. E. Clothiaux, Cloud droplet size distributions in low-level stratiform clouds, Journal of the atmospheric sciences 57 (2) (2000) 295–311.

[80] H. Barker, G. Stephens, P. Partain, J. Bergman, B. Bonnel, K. Campana, E. Clothiaux, S. Clough, S. Cusack, J. Delamere, Assessing 1D atmospheric solar radiative transfer models: Interpretation and handling of unresolved clouds, Journal of Climate 16 (16) (2003) 2676–2699.

[81] R. M. Goody, Y. L. Yung, Atmospheric radiation: theoretical basis, 2nd edition.

[82] R. V. Kochanov, I. E. Gordon, L. S. Rothman, P. Wcisło, C. Hill, J. S. Wilzewski, HITRAN application programming interface (HAPI): A comprehensive approach to working with spectroscopic data, Journal of Quantitative Spectroscopy and Radiative Transfer 177 (2016) 15–30.

[83] D. EdwardsGENLN, A general line-by-line atmospheric transmittance and radiance model. version 3.0 description and users guide,, National Center for Atmospheric Research.

[84] M. Lee, Scaling anisotropic scattering in radiation heat transfer for a planar medium, Urbana 2 (1982) 61801.

[85] R. G. Ellingson, J. Ellis, S. Fels, The intercomparison of radiation codes used in climate models: Longwave results, Journal of Geophysical Research: Atmospheres 96 (D5) (1991) 8929–8953.

[86] National Aeronautics and Space Administration - NASA, CIRC: Continual Intercomparison of Radiation Codes, https://circ.gsfc.nasa.gov/index.html (2015).

[87] L. Oreopoulos, E. Mlawer, J. Delamere, T. Shippert, J. Cole, B. Fomin, M. Iacono, Z. Jin, J. Li, J. Manners, The continual intercomparison of radiation codes: Results from phase i, Journal of Geophysical Research: Atmospheres 117 (D6).

[88] M. Li, C. F. M. Coimbra, On the effective spectral emissivity of the sky, Proceedings of the National Academy of Sciences of the United States of America submitted.

[89] E. R. Peck, K. Reeder, Dispersion of air, JOSA 62 (8) (1972) 958–962.

[90] L. House, L. Avery, The Monte Carlo technique applied to radiative transfer, Journal of Quantitative Spectroscopy and Radiative Transfer 9 (12) (1969) 1579–1591.

[91] D. Toublanc, Henyey–Greenstein and Mie phase functions in Monte Carlo radiative transfer computations, Applied optics 35 (18) (1996) 3270–3274.

[92] J. R. Frisvad, Importance sampling the rayleigh phase function, JOSA A 28 (12) (2011) 2436–2441.

[93] O. N. Vassiliev, Monte Carlo methods for radiation transport, Fundamentals and Advanced Topics (Cham: Springer).

[94] G. F. Nemet, Net radiative forcing from widespread deployment of photovoltaics, Environmental science & technology 43 (6) (2009) 2173–2178.

[95] D. Millstein, S. Menon, Regional climate consequences of large-scale cool roof and photovoltaic array deployment, Environmental Research Letters 6 (3) (2011) 034001.

[96] A. Hu, S. Levis, G. A. Meehl, W. Han, W. M. Washington, K. W. Oleson, B. J. van Ruijven, M. He, W. G. Strand, Impact of solar panels on global climate, Nature Climate Change 6 (3) (2016) 290.

[97] R. Fu, D. J. Feldman, R. M. Margolis, M. A. Woodhouse, K. B. Ardani, Us solar photovoltaic system cost benchmark: Q1 2017, Tech. rep., National Renewable Energy Lab.(NREL), Golden, CO (United States) (2017).